Finding Structure Property Relations for Designing High Mobility Semiconducting Polymers

Thesis submitted in accordance with the requirements of the University of Liverpool for the degree of Doctor in Philosophy

by

Rex Manurung

School of Physical Sciences

Department of Chemistry

December 2023

Contents

List of Figures and Tables

List of Abbreviations

1D	1 Dimensional
AO	Atomic Orbital
B3LYP	Becke 3-Parameter Lee-Yang-Parr Exchange-Correlation Functional
BHJ	Bulk Heterojunction
DA	Donor-Acceptor
DOS	Density of States
GDM	Gaussian Disorder Model
HOMO	Highest Occupied Molecular Orbital
IPR	Inverse Participation Ratio
LL	Localisation Length
LMO	Localised Molecular Orbital
LMOM	Localised Molecular Orbital Method
LUMO	Lowest Unoccupied Molecular Orbital
MO	Molecular Orbital
OLED	Organic Light Emitting Diode
PHJ	Planar Heterojunction
RMSE	Root Mean Squared Error
SRU	Structural Repeating Unit

TFT	Thin Film Transistor

Acknowledgements

I would like to thank Prof. Alessandro Troisi, for giving me the opportunity to do this PhD degree, and for his supervision, advice and support throughout my time at the University of Liverpool. Thank you for giving me the opportunity to do interesting work in projects and other various collaborations, as well as helping me develop further in my skills and experience.

I would also like to thank members of the Troisi Group for our interactions during my time at the University of Liverpool, for technical help, general friendliness and cultivating a good working environment. I would like to thank colleagues Tahereh Nematiaram and Ömer Omar for being always willing to answer my questions and help with issues arising during my work. I would like to thank Maryam Reisjalali for the opportunity to collaborate with her on some of her published work.

I would like to thank the University of Liverpool and Leverhulme Trust (via the Leverhulme Research Centre for Functional Materials Design) for their financial support.

Declaration

This thesis is submitted to the University of Liverpool in support of my application for the degree of Doctor of Philosophy. I, Rex Manurung, have composed this thesis and declare that this work contains original work done by myself unless specified otherwise.

Below is a list outlining which portions of this thesis have been derived from published works:

- Chapter 4 is derived from a published peer-review journal article, “Rapid Method for Calculating the Conformationally Averaged Electronic Structure of Conjugated Polymers”:

  R. Manurung, P. Li and A. Troisi, *The Journal of Physical Chemistry B*, 2021, **125**, 6338-6348

- Chapter 5 is derived from a published peer-reviewed journal article, “Screening Semiconducting Polymers to Discover Design Principles for Tuning Charge Carrier Mobility”:

  R. Manurung and A. Troisi, *Journal of Materials Chemistry C*, 2022, **10**, 14319-14333

Abstract

Conjugated polymer materials are attractive materials for electronics, being solution processable, light weight and tuneable through synthesis. Their more disordered microstructure, however, make it difficult to identify a clear universal structure property relation for charge carrier mobility, an important figure of merit in all device applications. Additionally, it is computationally expensive to study polymer materials using theoretical approaches while including atomistic level detail. In this thesis, the development of a rapid method for computing the electronic structure of large ensembles of polymer chains is presented. A tight-binding based approach is used to simplify the generation of the input Hamiltonian matrices for the polymer chains which approximates the matrix elements for the full chain with those obtained from monomer and dimer fragments of adjacent monomer pairs occurring along the chains. An implementation of the method is described which allows for improvement of accuracy in the energies obtained from calculations with a calibration procedure and reuse of input matrices for calculations. The method is initially demonstrated for 5 polymers, where it is shown that the electronic structure can be characterised using the density of states and orbital localisation characteristics calculated for the polymers. The method is then demonstrated in a screening study sampling 36 unique polymers taken from recent examples reported in literature. It is demonstrated that the localisation length can be used as a proxy for charge carrier mobility and that two properties of the polymers have the most notable effect on increasing the localisation length; reduced fluctuation of the coupling between localised HOMO orbitals on each monomer and the presence of only two monomers in the polymer repeat unit. Other features, such as the difference in HOMO orbital energies along the polymer repeat unit and an overall smaller coupling between HOMO orbitals localised on adjacent monomers are identified to have some effect. These findings form the basis of suggested design principles to find polymers with higher mobility.

Chapter 1
An Overview of Polymeric Semiconductors

1.1 Semiconducting polymers

Semiconducting conjugated polymers are carbon-based materials made of individual chains constructed from smaller monomeric units. The bulk solid-state properties of these materials arise from the soft van der Waals interactions between individual chains which hold them together in the material, and their electronic properties from the π-conjugated electronic states on each monomer that delocalise across individual and several chains. The electronic structure results from the sp^2 hybridised carbon atoms on the monomers, which lead to σ-bonds arising from the sp^2 orbitals forming the polymer backbone bonding, and a π-bond network arising from the contiguous overlap of the singly occupied monomer p orbitals orthogonal to the σ-bonds, illustrated in Figure 1.1. The conductivity of conjugated polymers results from the molecular orbitals formed by p-orbitals on sp^2 hybridised carbon atoms which couple and form bands with states closely spaced in energy, resulting in an occupied and unoccupied band of states separated by a band gap.

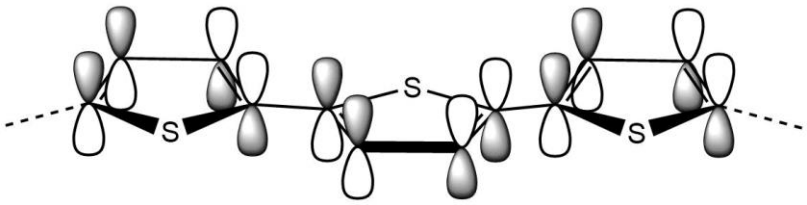

Figure 1.1: Illustration of conjugated p orbitals orthogonal to the plane of the monomers along a segment of an example polymer chain.

The semiconducting nature of conjugated polymers arises when charges are injected into the bands, for example by introduction from electrodes, adding dopants[1] or promotion of charges across the band gap between the valence and conduction bands by energetic excitation of the polymer[2]. There are two possible types of charge carriers which are negatively charged electrons and positively charged holes, and conjugated polymers can be categorised based on which of these charge carriers are the majority carriers in the material. Majority hole charge carrier materials are p-type while majority electron charge carrier materials are n-type, and ambipolar polymers display both hole and electron charge carrier transport. The p-type or n-type nature of the polymer is determined by the electron affinity of the monomeric units contained in the chains, where higher electron affinity monomers enable n-type conductivity.[3]

For device applications, desirable features of conjugated polymers are their flexibility[4], solution processability[5, 6] and light weight compared to inorganic materials used for electronics. However, the morphology of conjugated polymers typically ranges from semicrystalline to amorphous, with a mixture of ordered and disordered domains, and the morphologies are defined by how much of the material these domains occupy. This morphological difference thus precludes band transport throughout conjugated polymer materials like in their inorganic counterparts and makes it challenging to define a structure property relation for charge mobility. Examples of currently known high mobility polymers display charge carrier mobilities in the range 0.5–20 $cm^2 V^{-1} s^{-1}$,[7, 8] which is comparable to amorphous silicon[9] but still significantly behind conventional inorganic materials such as gallium arsenide (GaAs)[10] and silicon wafers[11] that exceed 100 $cm^2 V^{-1} s^{-1}$.

Early examples of conjugated polymers are polythiophenes such as P3HT[12] and poly[2,5-bis(3-tetradecylthiophen-2-yl)thieno[3,2-b]thiophene] (PBTTT)[13, 14], shown in Figure 1.2, which are p-type polymers due to the electron rich thiophene units and have exhibited mobilities in the range 0.1-1.1 $cm^2 V^{-1} s^{-1}$. These polymers are typically semicrystalline, with large ordered domains displaying lamellar-like structures.[15, 16]

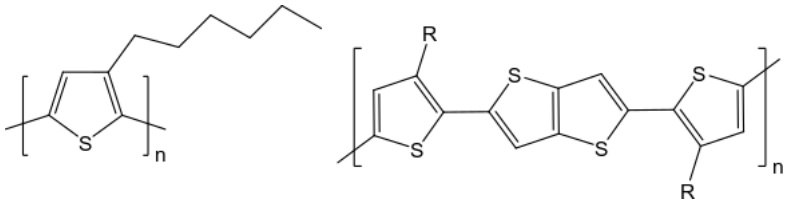

Figure 1.2: P3HT (left) and PBTTT (right) polymer structural repeat units (R=alkyl side chain group)

More recently, higher mobilities have been observed in donor-acceptor (DA) copolymers, in which the structural repeating unit of the polymer has an alternating sequence of lower and higher electron affinity monomers, which create a polarized pair that should help promote injection of charges into the polymer and charge carrier separation. These polymers typically display no long range order in their morphology and are poorly ordered or near amorphous.[17, 18] Reported mobilities for DA copolymers range from 0.1–20 $cm^2 V^{-1} s^{-1}$, where there are both n-type, p-type and ambipolar polymers.[7, 8] The observations from DA copolymers do not indicate a need for long range, crystalline-like order to achieve high mobility and instead strategies employed to improve mobilities include enforcing rigid and torsion free backbones[19, 20], optimising intermolecular stacking interactions[21] and aggregation of chains[22], and increasing molecular weight of the polymer chains[23]. Examples of DA copolymers are shown in Figure 1.3.

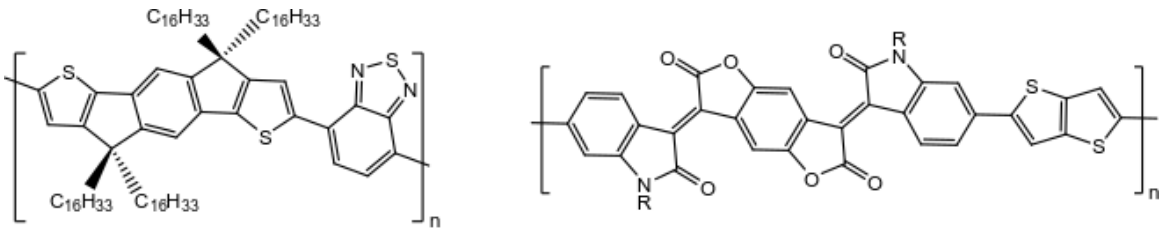

Figure 1.3: Donor-acceptor copolymers IDTBT (left), a p-type polymer, and BDOPV-BTT (right), an n-type polymer.

1.2 Applications of semiconducting polymers

The most important figure of merit in device applications of semiconducting conjugated polymers is charge carrier mobility, which measures the speed at which charge carriers in a material move in a given direction under an applied electric field. A general expression for the charge mobility $\mu_{\alpha\beta}$, where $\mu_{\alpha\beta}$ is a 3x3 tensor in the spatial coordinates α, β (x,y, and z coordinates), can be defined in terms of the time-averaged charge carrier velocity $\langle v_\alpha \rangle$ along a direction α and the applied (externally or built-in) electric field $\mathbf{F}$ inducing the current of carriers with component F_β acting in direction β, given in (1.2.1).

$$\mu_{\alpha\beta} = \frac{\langle v_\alpha \rangle}{F_\beta} \tag{1.2.1}$$

The main branches of semiconducting polymer device applications are field effect transistors[7], photovoltaics[24], and light emitting diodes[25]. In the area of transistors, the main focus has been thin film transistors (TFT), which are used in organic-based thin film and flexible electronic devices such as sensors[26] and flexible displays.[27] TFTs consist of a source, drain and gate contact, dielectric, conducting channel, and substrate, and these parts can be arranged in various device architectures, shown in Figure 1.4.[28] The conducting channel is a thin layer, only a few molecules thick, of conjugated polymer material deposited via solution-based methods such as spin- and dip-coating[29] or thermal evaporation.[28] The source and drain contacts are metal electrodes, while the gate contact can be a polymer or metal, and the dielectric layer is an insulator which separates the conducting polymer and gate contact.[30] The source and drain electrodes inject charge into the conduction channel under an applied voltage which generates a layer of charge between them causing a current. The charge flow through the polymer channel is modulated using the voltage applied through the gate contact and the conductivity of the polymer channel depends on the relative voltages between the source, gate and drain contacts. High mobility in the polymer is desirable to increase the sensitivity of the channel layer. For the polymer layer, p-type materials are predominantly used due to the lower ambient stability of electron rich n-type polymers[31], and a

diverse range of structural repeat units have been explored in transistor applications[8], examples of which are illustrated in Figure 1.4.

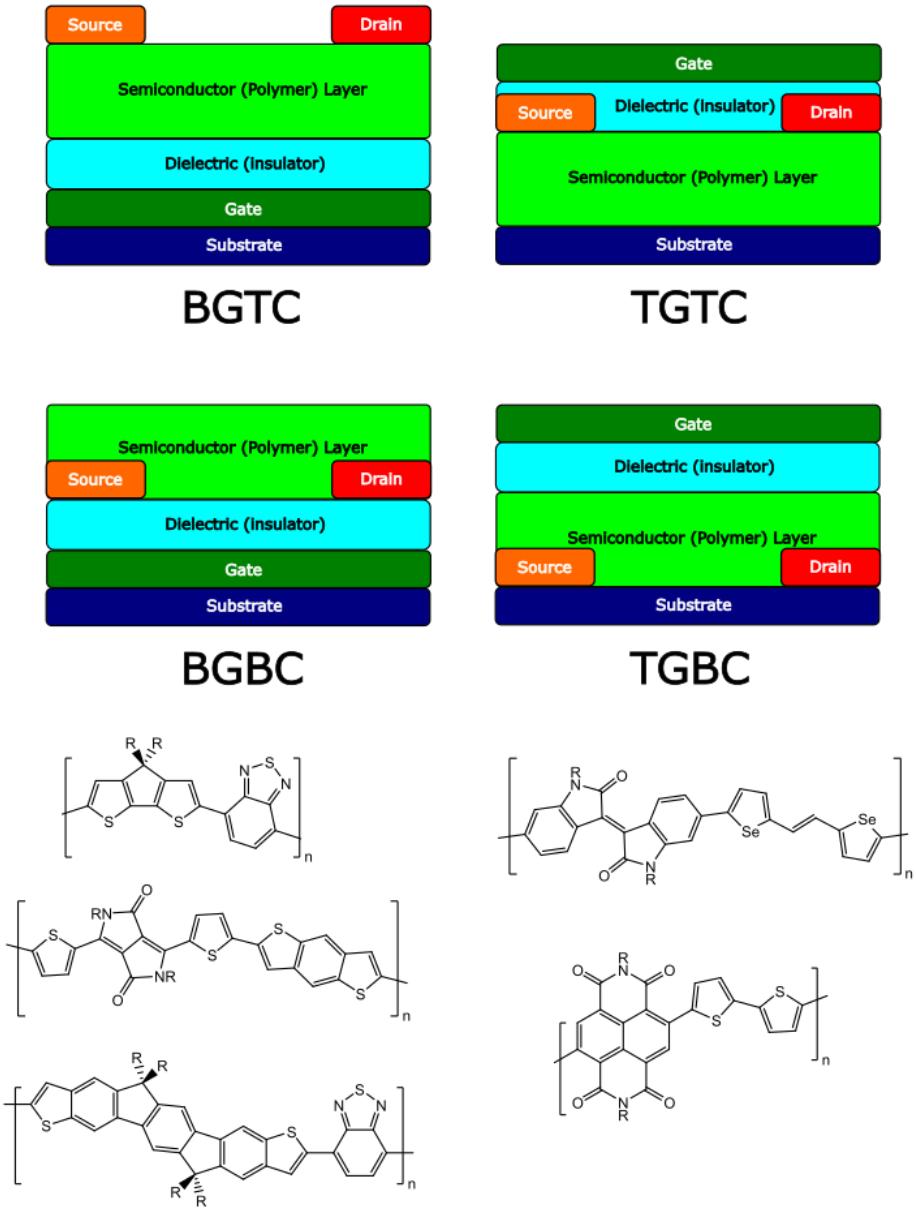

Figure 1.4: TOP: Device architectures for thin film transistors (TFT); Bottom Gate Top Contact (BGTC), Top Gate Top Contact (TGTC), Bottom Gate Bottom Contact (BGBC), Top Gate Bottom Contact (TGBC). BOTTOM: Examples of p-type (left column) and n-type (right column) polymers reported for transistor applications (R=variable side chain group). The selection of structural repeat units shown are adapted from references[7] and [8].

The basic construction of an organic solar cell device involves two electrodes sandwiching a semiconducting polymer layer, which consists of an n-type and p-type polymer, with one

transparent electrode (usually the anode side) to allow illumination and thus photogeneration of charge carriers in the polymer layer. Illumination of the polymer layer yields excitons, which ideally separate into distinct electrons and holes that are collected at the anode and cathode, respectively. The n-type polymer is the electron donating material, usually a conjugated polymer, while the p-type polymer is an electron acceptor, such as a fullerene derivative[32] or small molecule acceptor[33]. Initially, organic solar cells were constructed with a planar heterojunction (PHJ) architecture, with the n and p-type polymer deposited as separate discrete layers in a simple n-p bilayer arrangement or multiple cascaded layers[34] but more recent research focuses on the bulk-heterojunction architecture (BHJ)[35], in which the polymer layer is a solution processable blend of the n and p-type materials. The blend forms domains on the scale of the exciton diffusion length and the interpenetrating network of n and p-type regions resulting from the BHJ architecture increases the interfacial area between the n and p materials which allows for faster charge separation. The polymer layer in BHJs is also thinner, enabling faster exciton diffusion while preserving optimal optical absorption. These device architectures are illustrated in Figure 1.5. A key feature to optimise in organic solar cells is the open circuit voltage V_{oc}, the largest voltage possible provided by the solar cell to an external circuit, which is determined by the HOMO-LUMO bandgap of the polymer material.[36-38] Early polymers used for organic solar cells include polythiophenes, polyfluorenes[39] and polyphenylvinylenes (PPV)[40], with polythiophenes regarded as the benchmark materials. The most recent developments in organic solar cells, however, make use of donor-acceptor (DA) copolymer materials, in which the donor and acceptor monomer fragments can be varied separately thus allowing for better tuning of the band gap and HOMO-LUMO energy levels.[41] Example polymers are shown in Figure 1.5. Similar to TFT applications, a design challenge for improving solar cell performance is improving the charge carrier transport within the donor-acceptor blends, in order to decrease exciton recombination events that hamper efficiency.[42]

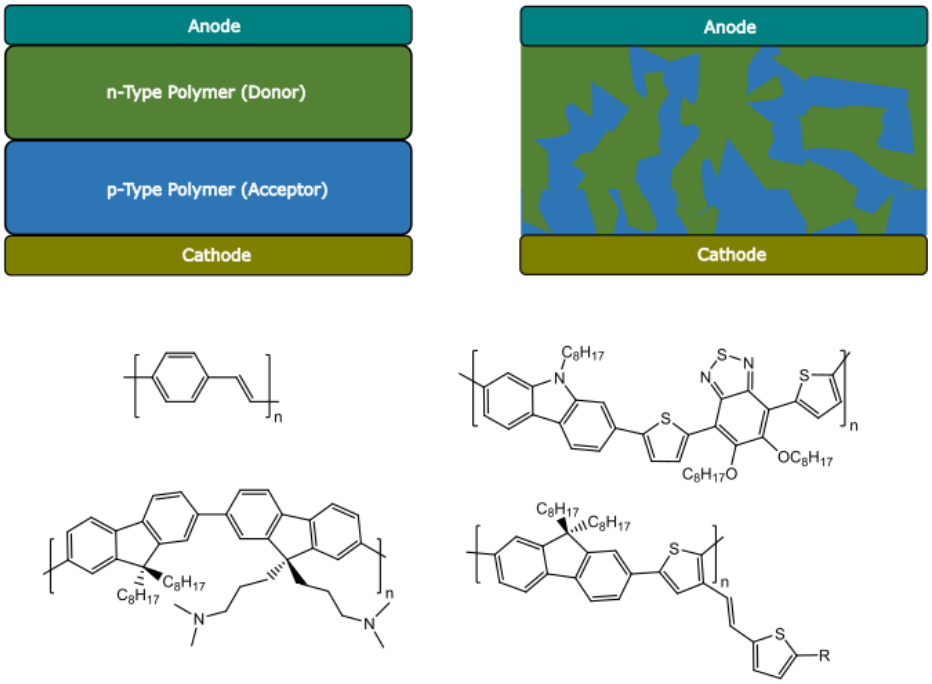

Figure 1.5: TOP: Device architectures for a planar (left) and bulk (right) heterojunction. BOTTOM: Structural repeat units for polyphenylvinylene (top left) and a polyfluorene (bottom left) polymer, and examples of DA copolymers (right column) reported for solar cell applications (R=variable side chain group). Structural repeat units shown are adapted from reference[35].

An emerging application is the use of conjugated polymers as photocatalysts for water splitting.[43] Currently, inorganic materials dominate this application but operate in the UV range[43, 44], which is not abundant in the solar spectrum. Organic polymers have been shown to enable photocatalytic water splitting in the visible light range and without the use of any precious metal doping and work with abundant electrolytes such as NaCl[43-45]. Example polymer materials that have been tested include porous conjugated polymers[45], and some of the already well known polymers in other applications, such as rr-P3HT, fluorene-benzothiadiazole copolymers, and polyphenylvinylenes.[43, 44] Example polymers used in photocatalysis are shown in Figure 1.6. In addition to being intrinsically more attuned to visible light absorption than inorganic materials, using polymers allows for cheaper and easier fabrication from solution processed methods, more precise tuning of properties through varying the monomer and co-polymer constituents with a large range of existing options for the

monomers[43], and having the active photocatalytic material (the polymer) in a homogeneous (solid) phase. Charge carrier mobility is significant is application as an important process of interest in photocatalysis is H^+ reduction, where transport of electrons across the polymer to reacting surfaces is a critical aspect of the process.

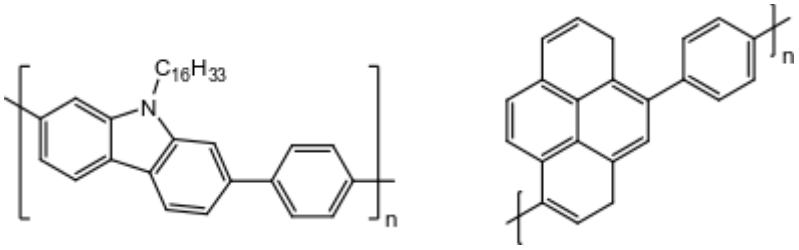

Figure 1.6: Structural repeat units of example conjugated polymers used in photocatalysis applications. Left structural repeat unit is from reference[44] and right is from reference[45].

Organic light emitting diodes (OLEDs) operate on a complementary principle to that of solar cells, in which charge carriers are injected into the polymer layer to recombine and induce photoluminescence. The basic construction of an organic light emitting diode, illustrated in Figure 1.7, has the polymer layer sandwiched between two electrodes which inject the charge carriers. The polymer layer can be single or multi-layered, where in the latter the layer is divided into an electron transporting (hole blocking) material, hole transporting (electron blocking) material, and an electroluminescent material.[25] Under an applied electrical potential the charge carriers are injected from electrodes to the electron and hole transporting layers. The hole and electron charge carriers travel through their respective transporting layers towards the electroluminescent material layer where they capture each other to form excitons. The electron and hole in the excitons can recombine to release photons, causing light emission from the device. Similar to the previous applications outlined, optimisation of the charge carrier mobility is an important consideration in designing new polymer light emitting diode materials to minimise trapping of electrons outside of the electroluminescent material layer and recombination with holes in non-emissive layers of the polymer which cause non radiative recombination losses in the device[46]. Other design challenges in the area of polymer light emitting diodes focus on improving the tunnelling injection of charges from

the electrodes into the polymer layer, increasing the intensity and efficiency of light emission from the electroluminescent layer and improving material stability towards degradation.[25]

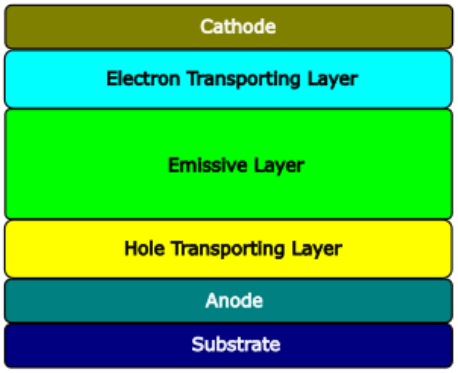

Figure 1.7: Device architecture for an organic light emitting diode.

1.3 Morphology, microstructure and charge carrier transport

Morphology defines the nature of the charge carrier transport in conjugated polymers at multiple scales. Charge transport characteristics are sensitive to features at the mesoscopic scale (chain alignments, chain coiling, domains) and those at the molecular level (onsite energies, electronic coupling), thus the features of the morphology are significant in determining the mode of charge carrier transport through different parts of the material.[47] In materials with clearly defined boundaries between crystalline and disordered regions, such as semicrystalline polymers, charge transport can be hindered due to the absence of states that overlap across both regions[48] which trap charges.[49] In amorphous materials, where there is no long range order with only small ordered domains, tie chains connecting between ordered aggregates are important in improving transport by providing states that access both ordered and disordered regions,[50, 51] and the different types of aggregates that can form[52] can lead to increased mobility due to improved interchain overlap between MOs on monomers.[53]

The nature of the individual polymer chains influences the overall morphology. Earlier examples of conjugated polymers studied, such as PBTTT, feature semicrystalline morphologies, in which there are discernible domains of ordered, lamellar and interdigitated chains separated by amorphous region boundaries.[13, 54] The picture from these materials favours the idea of polymer backbones which maintain longer range order throughout the material, and charge carrier transport that is delocalised along chains while in the domains, with hopping transport through amorphous regions between the ordered domains.[48, 55] However, the best performing polymers currently are donor–acceptor copolymers, such as IDT-BT, which show a higher proportion of bulk material as amorphous regions with scattered aggregated domains of ordered chains and have no apparent long-range order.[18] The charge carrier transport in this mostly amorphous morphology is facilitated by tie chains traversing between the ordered aggregates which can maintain a relatively ordered backbone, thus precluding the need for long range order throughout the material.[56] Overall, the effect of disorder in polymer morphology is to complicate the mechanism of charge transport due to the different types of aggregates and disordered regions that can form in the bulk, and the structure-property relation for morphology and carrier mobility remains unclear with the most recent examples of high mobility polymer showing disordered morphologies.

1.4 Finding strategies to optimise charge carrier mobility

Approaches to finding features of polymers which optimise charge carrier mobility include screening candidate materials by known material properties and identifying distinguishing features of those materials, predicting material properties of proposed novel materials and designing new polymer backbones by adding different moieties to constituent monomers to engineer specific interactions along the chain. Methods for screening polymers by known properties or generating predictions of properties can focus on optoelectronic properties such as HOMO−LUMO energies[57-60] and optical excitation energies,[61] or screen for physical properties such as solubility and molecular weight and

find the most optimal materials and features for these properties.[62] Using existing oligomer structures as starting points, promising materials can be discovered and identified by progressive alterations to a starting structure from existing databases of oligomers, such as with functional group and monomer substitutions, then predicting the optoelectronic properties for the novel generated structures.[63] These screening methods are fast at exploring the possible chemical space for candidate materials and have been used successfully to guide the synthesis of novel materials[64] but ignore the effect of chain disorder, which is the principal parameter affecting the charge mobility in conjugated polymers.

The design of polymer backbones can be approached through tuning the torsional disorder and electronic disorder. Torsional disorder can be tuned by engineering side chain interactions to lock dihedral angles and planarizing the π-conjugated core of the monomers, with the view that this concomitantly reduces electronic disorder. For side chains, an extensively researched approach is side chain functionalisation with heteroatoms to introduce non-covalent interactions that soft lock the dihedral angle between the plane of monomers.[65] These non-covalent interactions include known hydrogen bonding interactions O–H and N–H, but also N–S, O–S and the corresponding halogen based X–H and X–S interactions (X=halogen), with the participating heteroatoms either as side groups or embedded in the conjugated backbone.[66, 67] Some examples of polymer repeat units containing this design feature are illustrated in Figure 1.8. As a result of altering the backbone planarity *via* this approach, such interactions allow for tuning of the aggregate domain sizes, their crystallinity and thus morphology to achieve better mobility.[68, 69] An additional benefit to heteroatom non-covalent interactions is the ability to tune the electronic properties, where such interactions have been shown to narrow HOMO–LUMO bandgaps which facilitates charge transfer between affected monomeric units.[70]

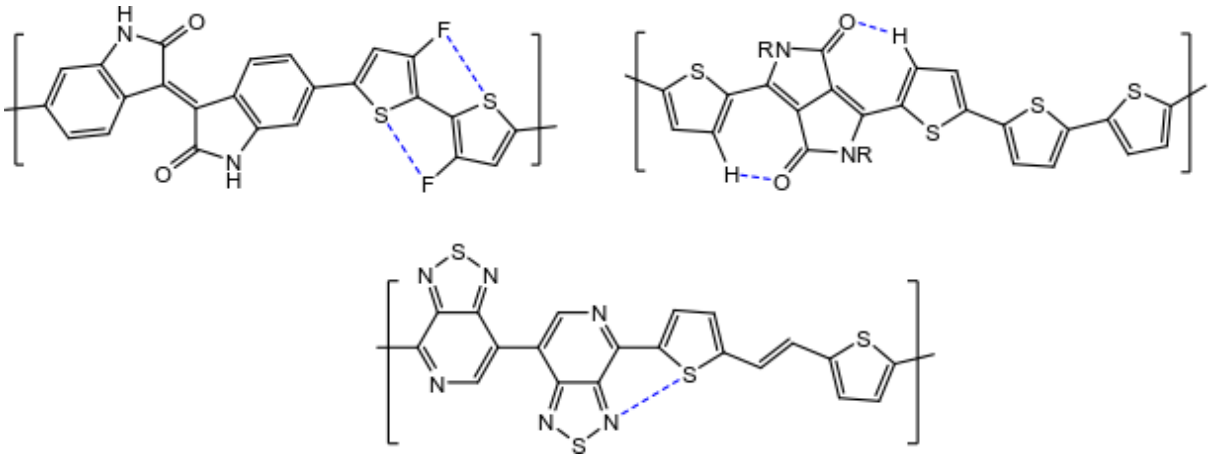

Figure 1.8: Structural repeat units of example polymers featuring engineered noncovalent contacts along the polymer backbone, where the anticipated interactions are highlighted with blue dashed lines (R=variable side chain group).

Another feature to tune in the polymer backbone is the monomer size, where the perspective is mixed. Examples representing the various different monomer sizes explored are illustrated in Figure 1.9. Increasing the monomer length can increase the number of interchain contacts and thus the connectivity for charge carrier hopping,[71] but at the cost of increasing the distance between atoms on the backbone periphery which can participate in non-covalent interactions, resulting in less torsional rigidity.[72] A contrary view to designing torsional rigidity is instead to make the coupling between monomers along backbones tolerant to non-planarity,[73] where a possible route is to exploit overlap between π-MOs and n-lone pairs from peripheral groups on the monomer backbone.[74] Higher mobility has also been attributed to polymer backbones which can stabilise the charge carrier polaron, where localisation of the polaron to a smaller segment on polymer chains gives an energetically narrow distribution of states that the charge carrier can occupy and allows the chain to host more charge carriers on the chain.[75, 76]

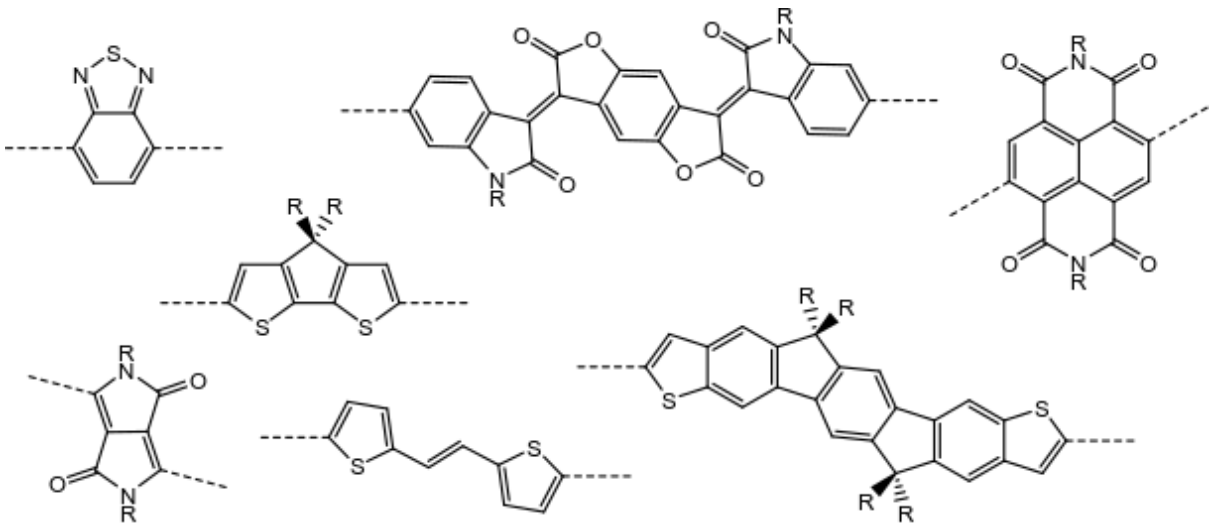

Figure 1.9: Examples of monomer units explored for conjugated polymers used in organic electronics showcasing the variety in molecular sizes. Dashed lines indicate sites on the monomer to which other monomers can bond. Structural repeat units adapted from reference[8].

The sequence of monomers is significant for the electronic coupling features of the polymer. An important result from phenomenological modelling reveals the importance of the sequence architecture for donor acceptor (DA) copolymers, showing that overall perfectly alternating (AB type sequences) DA sequences and block copolymers with closer to uniform block lengths exhibit better predicted mobilities than more randomised DA sequences, and that the effect of altering the gap between the donor and acceptor MOs is dependent on the type of monomer sequence.[77] There are contrasting views on whether the energy gap between MOs on adjacent monomers should be large or small, with large gaps suggested to be unfavourable as they result in localisation and thus trapping of the charge carrier,[78] while other work suggests a preference for large gaps due to narrowing of bands which makes charge carrier states more accessible.[77, 79] It has also been proposed that the influence of tuning MO energy differences is diminished or enhanced depending on whether the hopping occurs across energetically localised or delocalised bands.[77] The current work for polymer backbone design reveals some consistent principles across several examples but this has still yielded a variety of monomer structures, sequence architectures and moieties thus indicating an overall consensus on structure property relation is still lacking.[8]

1.5 Objectives of the work in this thesis

The introduction and background sections in this chapter show that a general structure property relation for charge carrier mobility in conjugated polymers is still lacking. There are several design principles prescribing molecular, structural and sequence features to obtain better carrier mobilities; however, many are reported and discovered using specific polymer examples. With this in mind, the work in this thesis has two goals:

- The first goal is to develop a method able to perform calculations which allow characterisation of many polymers, encompassing as much of the state-of-the-art conjugated polymers reported as possible, and infer their relative mobility. The method developed will include atomistic detail for the polymer chains to best incorporate the effects of electronic and conformational disorder in the polymers. Work related to this aim is outlined in Chapter 3.
- The second goal is to employ the method developed for characterisation of polymers to screen the large space of state-of-the-art conjugated polymers and discover general structure property relationships for the charge carrier mobility using the inferred relative mobility of the polymer sequences examined in the screening. Work related to this aim is outlined in Chapter 4.

Chapter 2

Modelling of Charge Transport in Semiconducting Polymers

2.1 Charge carrier transport in disordered polymers

The nature of the charge carrier transport can be determined by first considering the general one-electron Hamiltonian for the system H given in 2.1.1 with the components in 2.1.2-2.1.6.[80] This Hamiltonian assumes low-carrier density, thus electron-electron correlation and coulomb effects are not included.[81] $\in_n$ is the energy of the orbital at site n hosting the excited electron charge carrier with fluctuation $\delta \in_n$ due to disorder in the lattice containing the polymer molecules, $a_n^\dagger/a_n$ are the creation/annihilation operators that add/remove a charge carrier on a site with energy $\in_n$, $b_\lambda^\dagger/b_{-\lambda}$ are the creation/annihilation operators for vibrational mode λ with energy $\hbar\omega_\lambda$, $g_{n\lambda}^2$ and $f_{nm\lambda}^2$ are dimensionless electron-phonon coupling constants, J_{nm} is the coupling between sites n and m in a perfectly ordered lattice and δJ_{nm} is the fluctuation in the coupling due to disorder.

$$H = H_0 + H_1 + H_2 + H_3 + H_4 \tag{2.1.1}$$

$$H_0 = \sum_n \in_n a_n^\dagger a_n + \sum_\lambda \hbar\omega_\lambda (b_\lambda^\dagger b_\lambda + \frac{1}{2}) \tag{2.1.2}$$

$$H_1 = \sum\nolimits_{n\neq m}^{n,m} J_{nm} a_n^\dagger a_m \tag{2.1.3}$$

$$H_2 = \sum_\lambda \sum_n g_{n\lambda}^2 \hbar\omega_\lambda a_n^\dagger a_n (b_\lambda^\dagger + b_{-\lambda}) \tag{2.1.4}$$

$$H_3 = \sum\nolimits_{n\neq m}^{n,m} \sum_\lambda f_{nm\lambda}^2 \hbar\omega_\lambda a_n^\dagger a_m (b_\lambda^\dagger + b_{-\lambda}) \tag{2.1.5}$$

$$H_4 = \sum_n \delta \in_n a_n^\dagger a_n + \sum\nolimits_{n\neq m}^{n,m} \delta J_{nm} a_n^\dagger a_m \tag{2.1.6}$$

H_0 gives the total energy of the polymer molecules and the lattice excited with the charge carrier without polaronic effects arising from interaction between the lattice and the electronic excitation.

H_1 gives the transfer energy associated with the electron charge carrier moving from site n to m. H_2 gives the energy relaxation of site n hosting the charge carrier due to intermolecular and intramolecular vibrations (lattice vibrations) on accommodating the carrier (electron-phonon coupling). H_3 gives the energy due to electron-phonon coupling in the transfer of the charge carrier from site n to m, in which lattice vibrations alters the probability amplitude for the transition. H_4 gives the energy due to the transfer of the charge carrier from site n to m in which the probability amplitude for this transition and site energies are altered by morphological and conformational disorder in the polymer. The coupling between sites J_{nm}, disorder due to fluctuation in the coupling and site energies δJ_{nm} and $\delta \in_n$, and the strength of electron-phonon coupling indicated by $g^2_{n\lambda}$ and $f^2_{nm\lambda}$ determine the charge transfer characteristics and thus nature of charge transport. When expressed in matrix form the Hamiltonian H has the onsite energies $\in_n$ (from $\sum_n \in_n a_n^\dagger a_n$ term in H_0) along the diagonal and elements arising from coupling between sites are off-diagonal. H_0 and H_4 describe the on-diagonal onsite energies and their fluctuation due to disorder through terms $\sum_n \in_n a_n^\dagger a_n$ and $\sum_n \delta \in_n a_n^\dagger a_n$, respectively, while terms in H_1, H_2, H_3 and the $\sum_{\substack{n,m \\ n\neq m}} \delta J_{nm} a_n^\dagger a_m$ term in H_4 describe the off-diagonal elements. The disorder in the Hamiltonian can be described in terms of static and dynamic disorder, which relate to the fluctuation in site energies relative to dynamics of the charge carrier transfer. Static disorder is when the distribution of site energies varies much more slowly than the charge transfer dynamics, which corresponds to disorder in the on-diagonal elements of the Hamiltonian from fluctuations in the site energies described by terms in H_0 and H_4. Dynamic disorder is present if the energy of site levels fluctuates on a time scale comparable to the transfer dynamics, corresponding to the fluctuation in the off-diagonal coupling elements from electron-phonon coupling interactions described by terms in components H_2 and H_3 of the Hamiltonian.[80]

In conjugated polymers, the MOs of the charge carrier states can be described by the linear combination of orbitals localised on the monomeric units. A polymer chain MO ψ_j can be expressed

as the linear combination of the monomer orbitals φ_i each with contribution denoted by coefficient c_{ji} as given in 2.1.7, where indexes i and j run over the polymer MOs and monomer orbitals, respectively.

$$\psi_j = \sum_i c_{ji}\varphi_i \tag{2.1.7}$$

In an idealised rigid polymer chain, with perfectly planar dihedral angles between the planes of the monomeric units that make up the chain backbone, there is band transport with the charge carriers occupying delocalised band states and the coupling between neighbouring sites J_{nm} dominates the transport characteristics. The bulk material in disordered conjugated polymers, however, consists of individual chains bound by weak Van der Waals forces and there is conformational and electronic disorder in the polymer chains. The molecular orbitals of the charge carrier states are localised as a result of the disorder in the chains[80, 82] and there is a spreading of their energies, known as Anderson localisation.[83-85] The polymer MOs are strongly coupled with the conformation of the chains and morphology of the polymer material, and perturbed by intermolecular interactions, disorder along chains and in the bulk material.[80] In the microstructure of disordered conjugated polymers, static disorder in the Hamiltonian, corresponding to $\delta \in_n$ in H_4 and the spreading of site energies, arises from the positional and conformational disorder in the polymer chains, the latter being a fluctuation in the dihedral angles between monomeric units. Conformational disorder also contributes to off-diagonal disorder in the Hamiltonian through the $\sum_{n,m \atop n \neq m} \delta J_{nm} a_n^\dagger a_m$ term of H_4, affecting the coupling between MOs on monomeric units. Dynamic disorder in the Hamiltonian, affecting terms H_2 and H_3, arises from coupling of the charge carrier with the nuclear motion in the polymer chain through the polaronic effect, where the charge carrier deforms the surrounding molecular environment it occupies. The charge carrier and the nuclear reorganisation of the surrounding molecular structure are treated together as a polaron trapped by the conformational and site energy disorder in the polymer,[83] and displacements of these polarons across the polymer material are thermally activated and can be mediated by tunnelling.[86, 87] Features of the polymer morphology,

such as chain aggregation, stacking and tie chains between aggregated domains in the bulk material affect the mode of transport,[52, 56] where the charge carrier can move along (intrachain transport) and between chains (interchain transport), and movement between aggregate and amorphous domains also presents an energetic barrier to transport through weak overlap of the orbitals between these regions.[22, 49] In summary, the charge transport in conjugated polymers compared to inorganic materials is complicated by static and dynamic disorder arising from the conformational freedom in the chains, the polaronic effect, and charge carrier sites being localised on a mixture of amorphous and aggregate domains.

Conceptually, transport in disordered organic materials is modelled based on the picture that charge carriers move between individual sites hosting charge carrier states, localised by the disorder, by thermally activated tunnelling ("hopping").[80] In terms of molecular structure, charge carrier states exist on molecular fragments of the polymer chains, where each fragment position in the material represents an electronic site with wavefunctions that describe an energy state the charge carrier can occupy. The elementary process of transport is the hopping of a charge carrier from one site to the next empty site, and the dynamics of this is described by the master equation in 2.1.8.[88] The probability that site i is excited with a charge carrier at some point in time t is $f_i(t)$, with the probability that the site is unoccupied being $[1 - f_i(t)]$. $\frac{\partial f_i(t)}{\partial t}$ is the rate of change in $f_i(t)$, which is the rate of transfer from site i to j. W_{ij} is the transition rate from occupied site i to a specific empty site j. λ_i is the decay rate of the excited state at site i with the charge carrier, corresponding to recombination of an electron with a hole.

$$\frac{\partial f_i(t)}{\partial t} = \sum_{j \neq i} W_{ij} f_i(t)\big[1 - f_j(t)\big] - \sum_{j \neq i} W_{ji} f_j(t)[1 - f_i(t)] - \lambda_i f_i(t) \qquad (2.1.8)$$

Typically, the decay rate term $\lambda_i f_i(t)$ is treated as negligible.[88] The most commonly used transition rate W_{ij} for disordered polymers is the Miller-Abrahams equation in 2.1.9.[89] The equation gives the hopping rate W_{ij} from localised state i to j with energies E_i and E_j, respectively, for the transition upwards in energy ($E_j - E_i > 0$) and the downwards transition ($E_j - E_i < 0$), mediated by

absorption of energy from a phonon and tunnelling. v_0 is the "attempt-to-escape" frequency (maximum possible transition rate), $|R_{ij}|$ is the distance between sites i and j, γ is the inverse localisation radius (a measure of how well charge carriers can tunnel across distance $|R_{ij}|$), T is the temperature and k_bT is the thermal energy. The $\exp(-(E_j - E_i)/k_bT)$ component is the penalty for the upwards transition and indicates that this is thermally activated, and the $\exp(-2\gamma|R_{ij}|)$ component indicates the rapid exponential decline in tunnelling between the sites with increasing distance $|R_{ij}|$.

$$W_{ij} = \begin{cases} v_0 \exp(-2\gamma|R_{ij}|)\exp\left(-\frac{E_j - E_i}{k_bT}\right) : E_j - E_i \geq 0 \\ v_0 \exp(-2\gamma|R_{ij}|) : E_j - E_i < 0 \end{cases} \quad (2.1.9)$$

The probability of occupation for site i, f_i, is given by the Fermi-Dirac distribution in 2.1.10, where E_F is the Fermi energy, the energy of the highest occupied state electrons can occupy at absolute zero.

$$f_i(E_i) = \frac{1}{1+\exp\left((E_i - E_F)/k_bT\right)} \quad (2.1.10)$$

The energetic distribution of the charge carrier sites determines where the Fermi energy E_F is located, with the distribution of states near the edge (tail) of the valence band being most significant for charge carrier transport. The distribution of states is obtained by calculating the density of states (DOS) $f(E)$ function, which describes the distribution and localisation of the charge carrier states in energy. The gaussian disorder model (GDM), which is widely used for disordered polymers, computes the DOS as a distribution broadened by a gaussian function, given in equation 3.2.1; the Gaussian function is $g(E - E_m)$ with standard deviation σ, E_m is the energy of the molecular orbital representing a charge carrier state and N is the concentration of sites in inverse energy units.[80, 90]

$$f(E) = \sum_m g(E - E_m) = \sum_m \frac{N}{\sigma\sqrt{2\pi}} \exp\left(-\frac{(E - E_m)^2}{2\sigma^2}\right) \quad (2.1.11)$$

The propagation of charge carriers in the Gaussian DOS is illustrated in Figure 2.1. Charge transport occurs across a distribution of sites uncorrelated in space and energy, and hops occur from one occupied site to the next unoccupied site. The charge carriers that contribute to the overall transport through the material are located within the vicinity of the transport energy ε_t given in 2.1.12.[91] ε_0 is the energy scale of the DOS (σ for the gaussian DOS) and x_0 is the energetic difference between the starting and final state in a hop with the fastest rate in the DOS, dependent on the charge carrier concentration N_0, decay length of the wavefunction of the starting charge carrier state α, temperature of system T and ε_0.

$$\varepsilon_t = \varepsilon_0 x_0(T, N_0, \alpha, \varepsilon_0) \tag{2.1.12}$$

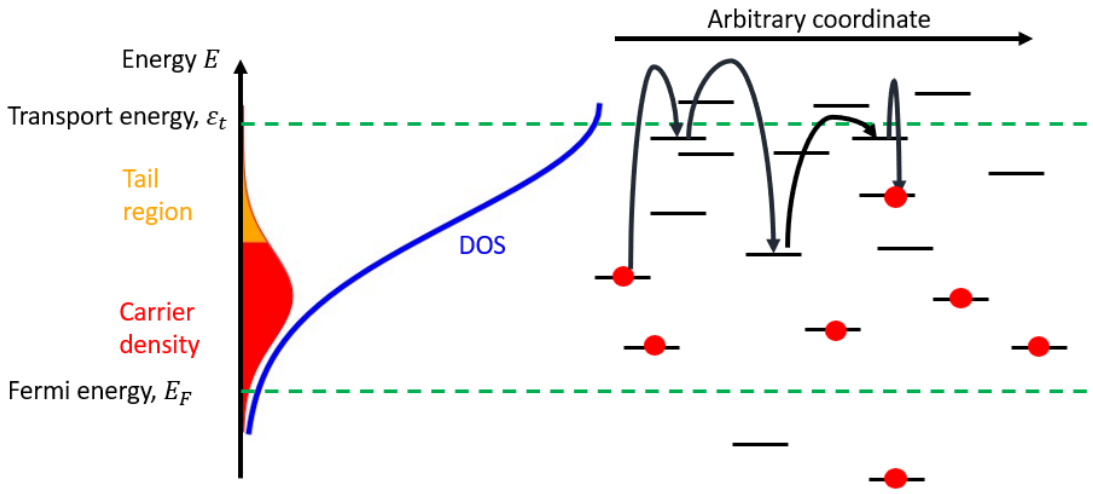

Figure 2.1: Illustration of the energy landscape of sites and density of charge carriers as described by a gaussian DOS (left), and hops (curved arrows) of charge carriers (red circles) across sites (right). Adapted from reference[90].

The tail state distribution in the DOS (those nearest to the transport energy, Figure 2.1) is significant as the width of the distribution indicates the conformational and electronic disorder in individual chains. For p-type semiconductors, the tail states at the valence band edge are highly localised in energy and have spacing much less than the thermal energy k_bT, making them thermally accessible to charge carriers.[92] The significance of the tail state distribution width has been confirmed by

multiple experimental studies, observed using absorption spectroscopy where the steepness of the absorption edge (Figure 2.2), measured by the Urbach energy, indicates the spread of the states.[20, 93, 94] A narrower width corresponds to a smaller spread of states near the tail and is associated with lower energetic disorder along the polymer backbone while spreading of the DOS tail is indicative of torsional disorder in the polymer chain, forming states that appear at the higher energy of the DOS tail and broadens the tail width (Figure 2.2).[95, 96] The possibility of characterising the electronic disorder of the bulk polymer arising from the conformational disorder in individual chains through the density of states thus presents a method of finding structure-property relationships in terms of chain features which affect the conformational and electronic disorder.

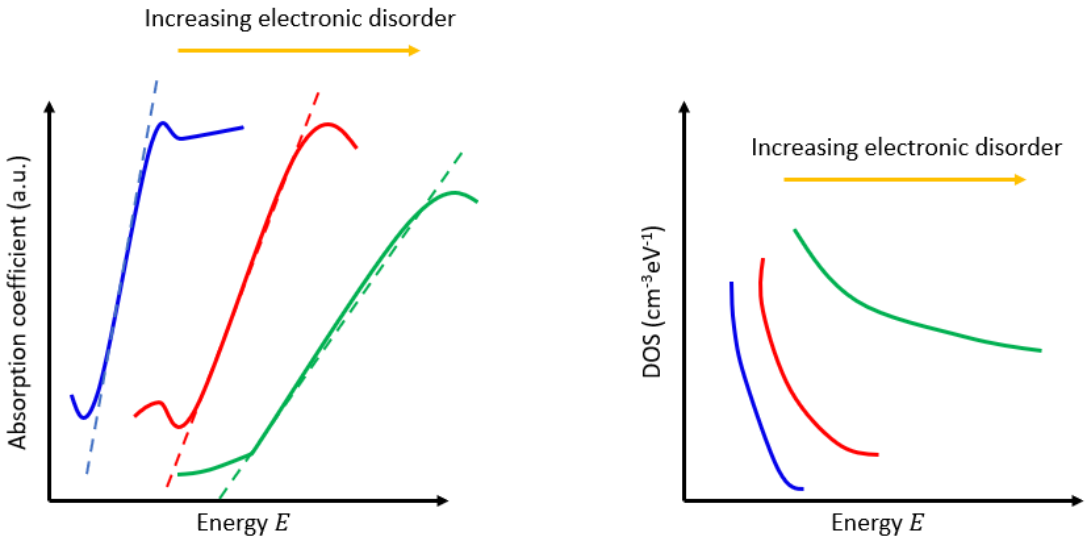

Figure 2.2: Representations of data from reference[93] illustrated to show essential features. LEFT: The absorption edge variation (blue, red and green curves) with increasing electronic disorder, dashed lines are exponential fits (absorption coefficient $\propto \exp(E)$) to extract the Urbach energy. RIGHT: The effect of increasing electronic disorder in the polymer on the tail state distribution width, indicated by the steepness of the curves (blue, red and green).

2.2 Modelling polymer materials with single chains

An important consideration when modelling the polymer material to obtain information about charge transport characteristics is how to simulate the bulk polymer which is required to calculate

the electronic structure. The electronic properties of the polymer can be characterised by the calculation of the density of states and in order to include the effects of structural disorder an atomistic model of the polymer material is required. A rapid method for calculating the electronic structure for a simulated bulk polymer material is to use an ensemble of single atomistic chains and neglect any interchain interactions, which is the approach used for calculations discussed in subsequent chapters. The justification is that the approach should still reproduce the essential electronic characteristics of the material, which is supported by some observations reported from other works. Qin and Troisi calculated the DOS for amorphous MEH-PPV, calculating the electronic structure with and without simulating the electrostatic environment for each polymer using point charges surrounding atoms on the chains, finding that the essential features of the DOS, such as the band gap and tail of the valence band, are still similar under both conditions and the weak extent of the electronic interaction between the chains was also cited as a factor.[97] This suggests that the DOS of amorphous polymers is largely determined by the electronic structure of the single chains constituting the polymer bulk material. Pearson et al. found that stretching of polymer chains of poly(3-octylthiophene) leads to increased conductivity (a measure of how easily charge carriers can move through the material), and that the same effect can be achieved by increasing the molecular weight of the chains.[98] This was rationalised by the increase in π-conjugation along individual chains and effective removal of conformational defects along chains on stretching the polymer, and suggests a stronger influence of the intrachain transport compared to interchain hopping on the conductivity, for which the individual chain properties are more important. Venkateshvaran et al. found that higher mobilities have been observed in amorphous polymers such as IDTBT displaying high disorder, lower density and non-interdigitated side chain morphologies where intrachain transport is expected to be the main contributor to carrier mobility, in contrast to semicrystalline PBTTT where there are significant interchain interactions such as π-stacks.[20] While these examples are of specific polymers, the works described provide a basis on using a single chain based approach when doing electronic structure calculations to obtain the DOS for similar amorphous polymers.

CHAPTER 3

Rapid Calculation of the Electronic Structure for Conjugated Polymers

The aim of the work presented in this chapter is to develop a rapid method for calculating the electronic structure of large quantities of polymer chains. First, the method for calculating the electronic structure using the localised molecular orbital method, key approximations, and implementation of the calculations are outlined. This is followed a discussion of the results for validating and improving the accuracy of the energies calculated using the method developed. Lastly, there will be results of calculations using the method for 5 unique polymers which are characterized by their orbital localisation and features of their density of states near the valence band tail, where the potential of the method is highlighted for use in screening applications to find high mobility polymers and understanding the structure property relation for mobility without explicit modelling of the polymer microstructure.

3.1 Localised molecular orbital method

The problem of computing the electronic structure for one-dimensional polymer chains is approached in this work by considering each chain as a linear oligomer being formed from discrete rigid conjugated monomer units. A monomer is defined as the chemically realistic rigid fragment possessing two carbon atoms that act as connection sites to which other monomers can bond in order to form an oligomer chain. The chain conformation arises from the relative orientation of the monomers in the chain, determined by the mutual geometry at each connection between adjacent

monomers. Enforcing rigid monomer units allows for the electronic structure of the chain to be calculated by considering the individual monomers and their mutual geometries in the chains only without further relaxation of the chain, an approximation shown to be reasonable for conjugated polymers.[99]

The electronic structure is calculated using the variational principle. For a trial wavefunction describing the system ψ, the variational principle obtains approximation to the true ground state energy of the system by minimising the expectation value E of the system Hamiltonian $\mathbf{H}$, given in equation 3.1.1.

$$E = \frac{\langle\psi|\mathbf{H}|\psi\rangle}{\langle\psi|\psi\rangle} \tag{3.1.1}$$

The wavefunctions ψ are the molecular orbitals (MO) for the system which is a polymer chain. The basis set for ψ is chosen from the available molecular orbitals on the monomers in the polymer. Using the Hartree-Fock method with the variation principle gives the Roothaan equations given in equation 3.1.2 used to calculate the energies $\mathbf{E}$ and MOs $\mathbf{c}$ of the polymer chain, which takes the Fock and overlap matrices ($\mathbf{F}$ and $\mathbf{S}$, respectively) of the chain as inputs.

$$\mathbf{Fc} = \mathbf{ESc} \tag{3.1.2}$$

$\mathbf{F}$ and $\mathbf{S}$ are obtained using the localised molecular orbital method (LMOM).[100] The method evaluates $\mathbf{F}$ and $\mathbf{S}$ by first partitioning polymer chains into smaller fragments derived from chemical intuition on the basis that the polymer chain orbitals can be described as a linear combination of the frontier orbitals of the fragments. In this work, these fragments are the rigid monomers and dimers formed by adjacent monomer pairs along the chain. The fragments obtained from partitioning are then capped by hydrogen atoms (terminal hydrogen atoms) at what would be connection sites to other monomers in the polymer chain. The process of this chain fragmentation is illustrated in Figure 3.1.

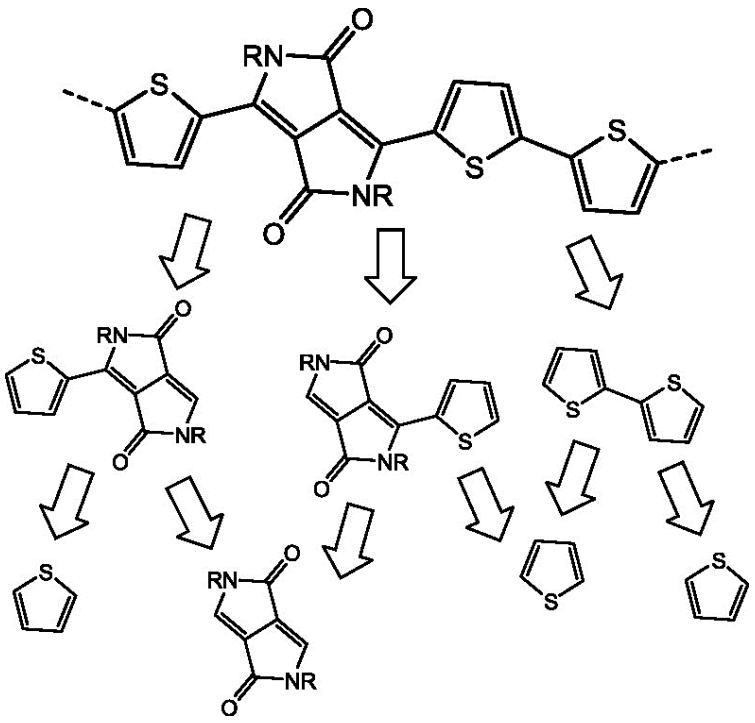

Figure 3.1: Partitioning an example polymer chain segment into smaller chemically realistic fragments.

Next, the MOs, Fock and overlap matrices for the rigid hydrogen capped fragments are obtained from a single point calculation. The MOs of the monomers thus obtained are extracted from the calculation output each as a vector of coefficients in the atomic basis. These monomer MO vectors are then expressed in the localised molecular orbital (LMO) basis by expanding them to the size of the fragment basis containing the monomers, with components of the MO not present in the fragment removed, and the monomer MO coefficients occupy positions in the basis of the fragment where the monomer would occur, illustrated in Figure 3.2. In dimers and larger fragments, the removed components of the monomer MOs arise from terminal hydrogen atoms lost from the monomer on forming the fragment and this is inconsequential as the chain MOs of interest, the frontier MOs, have contributions predominantly from the π-MOs on the fragments.

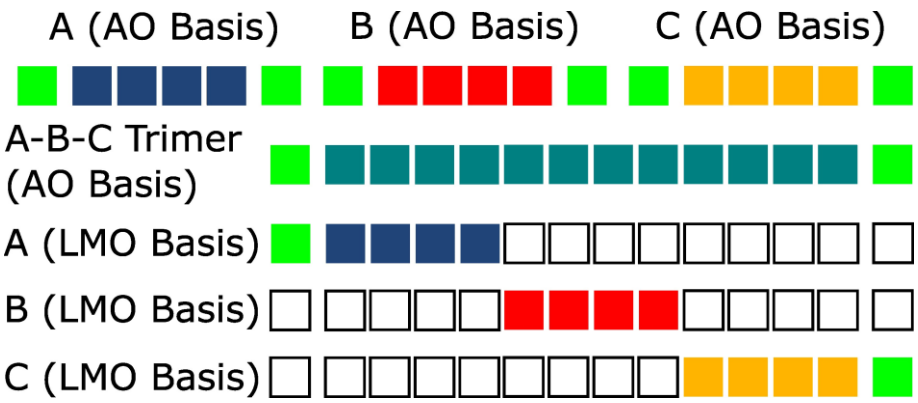

Figure 3.2: Illustration of how monomer MO coefficient vectors (monomers A, B and C, their basis elements as coloured squares) in the atomic orbital (AO) basis are expressed in the localised molecular orbital (LMO) basis. The hydrogen based basis components (green) lost from the monomer on forming the larger trimer fragment (A-B-C trimer, its basis elements as dark green) are removed to leave the other components remaining (blue, red and orange squares) and the basis is expanded to match the size of the trimer basis with zero elements (white squares).

Using the LMOs the fragment Fock and overlap matrices obtained from the single point energy calculations, denoted $\mathbf{F}^{\mathbf{A}}$ and $\mathbf{S}^{\mathbf{A}}$, are transformed from the atomic to the localised molecular orbital basis. The elements of the Fock and overlap matrix in the LMO basis F_{ij}^{LMO} and S_{ij}^{LMO} for the coupling and overlap between LMOs indexed i and j with coefficient vectors $\mathbf{C}_i$ and $\mathbf{C}_j$, respectively, are obtained from the atomic basis matrices $\mathbf{F}^{\mathbf{A}}$ and $\mathbf{S}^{\mathbf{A}}$ using the transformations given in (3.1.3) and (3.1.4). In the implementation of the transformations in this work, the LMO vectors occupy the columns of a single matrix $\mathbf{C}$, and a graphical representation of the transformations illustrating these is shown in Figure 3.3.

$$F_{ij}^{LMO} = \mathbf{C}_i^{\mathbf{T}} \mathbf{F}^{\mathbf{A}} \mathbf{C}_j \qquad (3.1.3)$$

$$S_{ij}^{LMO} = \mathbf{C}_i^{\mathbf{T}} \mathbf{S}^{\mathbf{A}} \mathbf{C}_j \qquad (3.1.4)$$

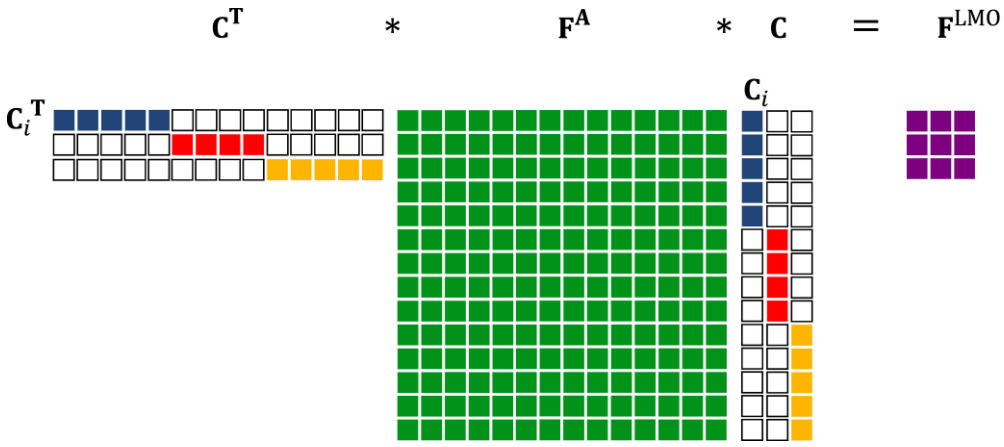

Figure 3.3: Illustration of the fragment Fock matrix $\mathbf{F}^{\mathbf{A}}$ (elements as green squares) being transformed ($\mathbf{C}^{\mathbf{T}}\mathbf{F}^{\mathbf{A}}\mathbf{C}$) from the atomic basis to the localised molecular orbital basis $\mathbf{F}^{\mathbf{LMO}}$ using LMO coefficient vectors $\mathbf{C}_i$ (non-zero elements as blue, red and orange squares, zero elements as white squares). The LMO coefficient vectors are the columns contained in a single matrix $\mathbf{C}$ ($\mathbf{C}^{\mathbf{T}}$ is its transpose). Each coefficient vector $\mathbf{C}_i$ in $\mathbf{C}$ represents 1 MO contributed from a monomer to the basis set of the LMOM calculation. An analogous transformation can be illustrated for $\mathbf{S}^{\mathbf{A}}$ replacing $\mathbf{F}^{\mathbf{A}}$.

These transformations can be done for any size fragment. For a monomer, the LMOs $\mathbf{C}_i$ are the same as those from the single point calculation output, while for dimers and larger fragments with multiple monomers, $\mathbf{C}_i$ is calculated using a monomer in the relative geometry they would occupy in the fragment and is expanded in size as described previously above. The number of LMOs from each fragment used for the transformations constitute the basis set and can be varied. For conjugated polymers the π-symmetry MOs on each monomer are chosen to form the basis set as these are the most relevant due to their contribution towards the frontier orbitals on the polymer chain.

For dimers and larger fragments, the p-orbital coefficients in $\mathbf{C}_i$ must be treated to ensure consistency between their signs and relative orientations of the monomers in the fragments before using them in 3.1.3 and 3.1.4. The phases of the p-orbitals in the π-MOs can be forced to align with a reference axis perpendicular to the planes of the monomers $\mathbf{d}_{\mathbf{h}}$, illustrated in Figure 3.4.

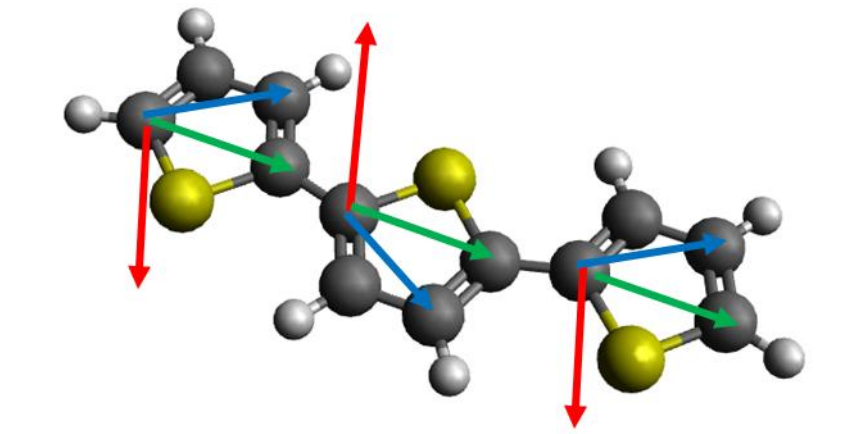

Figure 3.4: Illustration of vectors $\mathbf{d_1}$ (blue) and $\mathbf{d_2}$ (green) chosen on individual monomers in an example oligomer (pictured, and the vector $\mathbf{d_h}$ (red) obtained from the cross product of $\mathbf{d_1}$ and $\mathbf{d_2}$ on each monomer.

$\mathbf{d_h}$ is obtained for each monomer from the cross product, given in equation 3.1.5, of the distance vectors $\mathbf{d_1}$ and $\mathbf{d_2}$, defined by the position vectors $\mathbf{r_1}$, $\mathbf{r_2}$, and $\mathbf{r_3}$ corresponding to cartesian coordinates of three atoms selected involved in the π-conjugation on the monomer, labelled 1, 2 and 3 in Figure 3.4. On each monomer, atoms 2 and 3 are the ones connected to adjacent monomers, and atom 1 is any other carbon atom involved in the π-conjugation. The sign correction factor *g* by which all the LMO coefficients $\mathbf{C}_i$ are multiplied is obtained from the dot product given in equation 3.1.5 of vector $\mathbf{W}$, constructed with the values of the $2p_x$, $2p_y$ and $2p_z$ coefficients on the LMO $\mathbf{C}_i$ at atom 2 on the monomer as components, and $\mathbf{d_h}$. Only g=-1 changes the p-orbital phases on $\mathbf{C}_i$ thus equation 3.1.6 results in alignment of the p-orbital coefficients in the positive direction of $\mathbf{d_h}$ or leaves them unchanged when g=1.

$$\mathbf{d_h} = \mathbf{d_1} \times \mathbf{d_2} = (\mathbf{r_1} - \mathbf{r_2}) \times (\mathbf{r_3} - \mathbf{r_2}) \tag{3.1.5}$$

$$g = sgn(\mathbf{W} \cdot \mathbf{d_h}) = sgn\left(\left[2p_x\ 2p_y\ 2p_z\right] \cdot \mathbf{d_h}\right) \tag{3.1.6}$$

The phases of the p-orbitals in the MOs are fixed to the orientation of the monomer geometry thus the sign of the coupling between any two MOs on the monomers in an A-B dimer can change due to the symmetry of π-orbitals. In monomers where there are chemically identical connection sites, the

order of 2 adjacent monomers along the polymer chain (A-B or B-A order) can cause a difference in the sign of MO couplings between MOs localised on the monomers, illustrated in Figure 3.5.

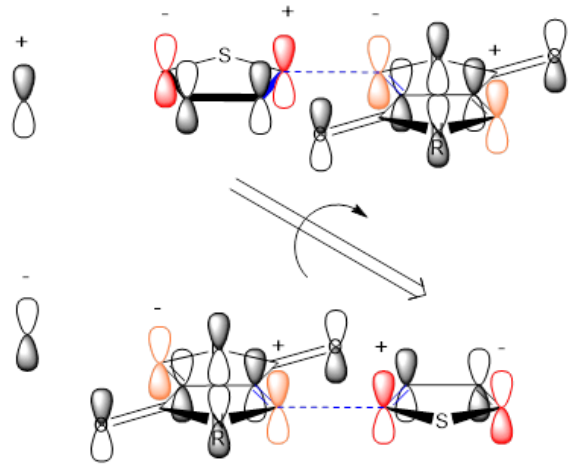

Figure 3.5: Illustration of the effect on the phase of the p-orbitals on each monomer, fixed relative to the monomer geometry, when the permutation of two different monomers in a pair changes from A-B to B-A along a polymer chain.

The sign of the coupling can be corrected to account for the difference due to the monomer order along the chain by considering the p-orbital lying perpendicular to the σ-bonds at the connection site atoms of the monomers, taken here as the $2p_y$ component. The sign of the $2p_y$ orbital on each connection site atom, assigned values -1 or +1, is determined by the phase pattern of the p-orbital lobes. As there are only linear polymer chains in the LMOM calculations, each monomer thus has only 2 possible connection sites, and these are either chemically identical or distinct. If at least one of the monomers A and B in the dimer A-B possesses chemically identical connection sites, the scheme outlined in Table 1 is used to determine the change in sign of the coupling calculated for any 2 LMOs for the pair A-B to obtain the coupling between those same LMOs in the dimer pair B-A.

Table 1 – MO coefficient sign modification table

Signs of $2p_y$ atomic orbital on connection site atoms in monomer A (right) to B (left)	Factor multiplied to sign of coupling element for 2 LMOs in the dimer pair A-B to obtain corresponding element for the same 2 LMOs in permutation B-A
+1, +1	None
-1, +1	Coupling element is multiplied by -1 for permutation B-A
-1, -1	None

Using the fragment matrices obtained with 3.1.3 and 3.1.4 the polymer chain Fock and overlap matrices $\mathbf{F}$ and $\mathbf{S}$ can be built in blocks of elements arising from LMOs interacting on the same monomer or LMOs on monomers adjacent on the polymer chain. To enable this, there are two assumptions used to simplify building the $\mathbf{F}$ and $\mathbf{S}$. First, it is assumed that the elements in the polymer chain matrix between LMOs on the same monomer or adjacent monomers can be calculated using MOs and matrices obtained with the fragments as described above using 3.1.3 and 3.1.4. Second, a tight binding approximation is invoked setting the matrix elements involving LMOs on nonadjacent monomers to zero. The overall building scheme for polymer chain matrix $\mathbf{F}$ (same scheme for overlap matrix $\mathbf{S}$) in terms of the blocks of fragment matrices is described by 3.1.7; for a monomer at a position along the polymer chain, indexed by *k*, the blocks of elements $\mathbf{F}_{k,k}$ are populated with elements involving LMOs on the same monomer and blocks $\mathbf{F}_{k,k+1}$ are populated with the elements from the matrix computed for a dimer fragment containing monomers at positions *k* and *k* + 1 on the polymer chain involving LMOs on different but adjacent monomers $\mathbf{F}^{\mathrm{LMO}}_{M(K),M(K+1)}$. These blocks of matrix elements are illustrated in Figure 3.6.

$$\mathbf{F} = \sum \mathbf{F}_{k,k} + \sum \mathbf{F}_{k,k+1}\,, \mathbf{F}_{k,k} = \mathbf{F}^{\mathrm{LMO}}_{M(K),M(K)}, \mathbf{F}_{k,k+1} = \mathbf{F}^{\mathrm{LMO}}_{M(K),M(K+1)} \tag{3.1.7}$$

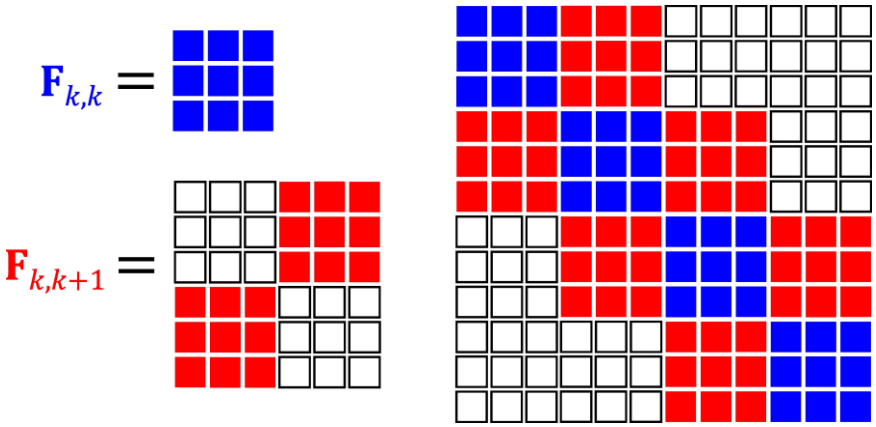

Figure 3.6: Illustration of the element blocks within the polymer chain LMO basis matrix corresponding to elements arising from LMOs interacting on the same monomer $\mathbf{F}_{k,k}$ ("monomer block" elements as blue squares) and LMOs on monomers adjacent on the polymer chain $\mathbf{F}_{k,k+1}$ ("dimer block" elements as red squares). Zero elements are white squares.

Figure 3.7 illustrates graphically the procedure of building **F** and **S** for an example oligomer using elements from its fragment matrices. The elements of **F** and **S** are in the LMO basis, thus the polymer chain MOs calculated using these matrices with the Roothaan equations in 3.1.2 are also expressed in the LMO basis. Overall, LMOM requires only that the polymer chain sequence is defined to calculate the electronic structure; from the chain sequence fragments can be partitioned and given that the LMO basis matrices for the fragments have been computed **F** and **S** can be built for the whole chain.

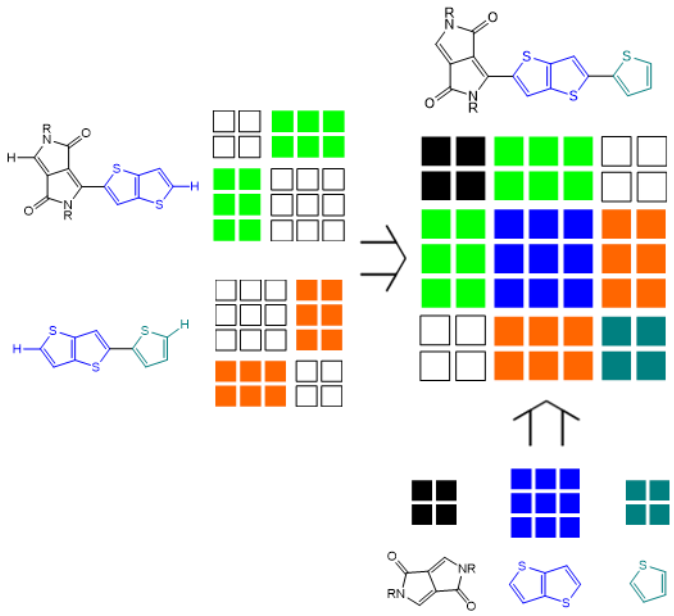

Figure 3.7: Illustration of scheme in 3.1.7 to build block matrices **F** and **S** for an oligomer containing DPP (black), BTT (blue), and thiophene (green) which contribute two, three, and two LMOs to the basis set, respectively. White square blocks represent matrix elements equal to 0, and the other coloured solid square blocks represent nonzero matrix elements. For dimers (orange and light green blocks), the monomer MO coupling elements are set to 0.

The effect of the assumptions invoked in LMOM (building the chain matrix from fragment matrices and tight-binding) were examined by a series of calculations with a planar 6 monomer polythiophene chain at B3LYP/3-21G*, where the atomic basis **F** and **S** matrices for the polythiophene are transformed to the complete MO basis using the same transformations given by 3.1.3 and 3.1.4, then elements were removed and/or replaced according to the approximations in

the assumptions and used as input for the Roothaan equations to calculate the MO energies. The matrix modifications are a) removal of elements not corresponding to adjacent monomer MO coupling (tight binding) b) replacement of exact elements arising from coupling between MOs on adjacent monomers with those computed for dimer fragments containing those monomers in the LMO basis, and c) using the modification in b) with the coupling elements involving MOs on the same monomer removed except along the diagonal. The energies from a full quantum mechanical calculation and calculations with the modified matrices both at B3LYP/3-21G* were compared by fitting them to a linear relationship, shown in Figure 3.8. The accuracy of the energies obtained from calculations with each matrix modification compared to the exact energies is assessed using the linear fitting parameters m and c, and root mean squared error (RMSE). The results show that the assumptions in LMOM still result in reasonable accuracy, where modification c) gives the worst match with the full calculation. Notably, using elements computed with dimer fragments to approximate the LMO coupling between adjacent monomer MOs (modification b)) only results in a ~3 fold increase in RMSE compared to the result obtained with only tight binding applied (modification a)), thus showing that approximating the polymer chain matrix with fragment matrices still maintains reasonable accuracy compared to an exact calculation.

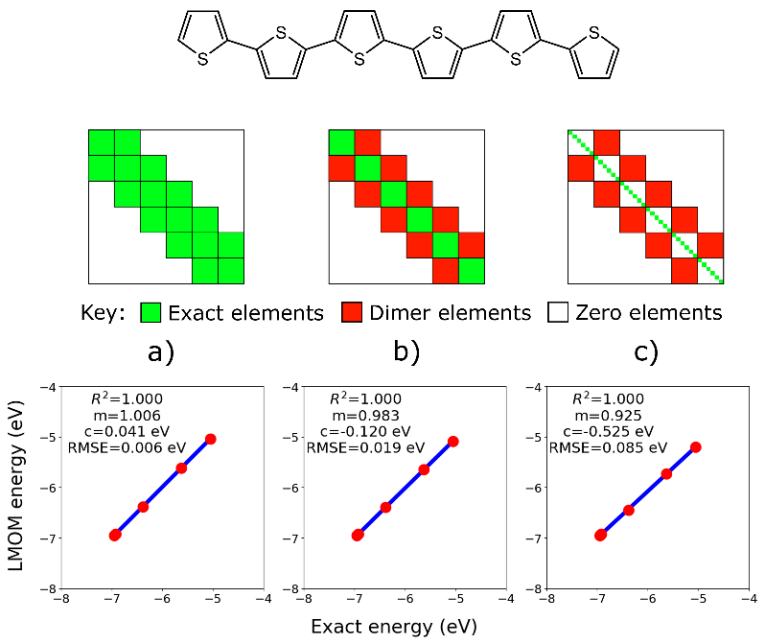

Figure 3.8: Plots (bottom) for the linear regression fit (blue line) of the energies for the top five levels in the valence band of a planar polythiophene chain (top) obtained from calculations with the approximations enforced in the LMO basis matrices $\mathbf{F}$ and $\mathbf{S}$ and exact calculation (B3LYP/3-21G*). The fit is measured by slope (m), intercept (c), correlation (R^2), and root mean square error (RMSE). Labels and approximations: (a) tight binding, (b) dimer fragment elements, (c) same monomer MO coupling to 0 and exact onsite energies on diagonal only, the manifestations of the approximations in $\mathbf{F}$ and $\mathbf{S}$ is illustrated above each plot (middle).

3.2 Polymer sample

To demonstrate the method outlined in section 3.1, 5 model polymers, IDTBT, DPPDTT, DPPBTz, polythiophene and PDPP2TT, were used for calculations where the structural repeat units (SRUs) are derived from those reported in the literature. The SRUs used for the calculations in this work, shown in Figure 3.9, have the side chain groups removed and replaced with hydrogen atoms to simplify the calculations. Table 2 gives abbreviated and chemical names of the polymers in the sample, and hole mobility data obtained from references quoted with their abbreviated names.

Table 2 – polymers and nomenclature

Abbreviated polymer name	IDTBT[18]	DPPBTz[101]	DPPDTT[102]	Polythiophene (P3HT)[12]	PDPP2TT[103]
Hole mobility ($cm^2V^{-1}s^{-1}$)	2.2 (± 0.2)	2.4	1.36 (± 0.26)	0.1	0.037 (± 0.015)
Chemical name	poly(indacenodithiophene-co-benzothiadiazole)	poly[[3,6-diketopyrrolo[3,4-c]pyrrole-1,4-diyl]- 2,1,3-benzotriazole]	poly[[3,6-dioxopyrrolo[3,4-c]pyrrole1,4-diyl]- alt −[[2,2’-bis-thieno[3,2-b]thiophen]-5,5’-diyl]]	-	poly[[3,6-dioxopyrrolo[3,4-c]pyrrole1,4-diyl]- alt −[[2,2’-bis-thieno[3,2-b]thiophen]-5,5’-diyl]]

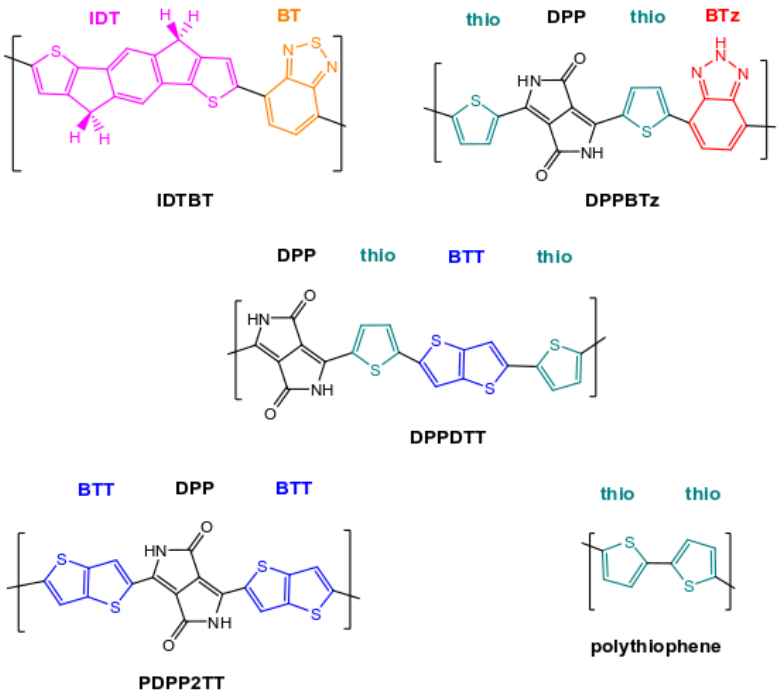

Figure 3.9: The simplified structural repeating units (SRU) of the polymers in the sample and monomers with abbreviated names.

Polythiophene is included as a homopolymer as the results for it can be compared to the other donor-acceptor copolymers. IDTBT, DPPDTT and DPPBTz are polymers reported in the literature for which experimental mobility data has been obtained in the same study that also reports tail widths from spectroscopically obtained DOSs, thus allowing for comparison with the results obtained in this work.[93] PDPP2TT is included in the sample as it is an example of a polymer where lower measured mobility is attributed to side chain effects which will allow a comparison between the observed mobility and the relative mobility inferred by the results of calculations using an idealized chain with removed side groups.[103]

3.3 Implementation of the localised molecular orbital method

The main parts for the implementation of the localised molecular orbital method developed in this work are the calculation of the fragment matrices, building of the polymer chain matrices from the fragment matrices and calculation of the polymer chain electronic structure. First, the basis set for calculating the fragment matrices must be chosen, which also determines the level of theory for the

polymer chain electronic structure calculations. Throughout the work in this thesis, the level of theory for calculating electronic structure and MO energies is B3LYP/3-21G*, which is low cost to use for LMOM calculations with large numbers of chains. There are two types of fragment matrices to compute; “monomer block” matrices with elements involving LMOs on the same monomer and “dimer block” matrices involving LMOs on different but adjacent monomers. The latter is computed using the structures of the dimers formed from adjacent monomer pairs that occur in the polymer chains being studied, thus calculations are done for all these pairs that are present in the chains. Once all the monomer pairs have been identified the structures of their dimers must be generated for calculations. The individual monomer structures are first optimized, which was done at B3LYP/3-21G* in this work. On each monomer there are defined 2 carbon atoms involved in the π-conjugation on the backbone which can bond to other monomers and about the bonds connecting two monomers, and there are 6 parameters determining their mutual geometry, illustrated in Figure 3.10. The intermonomer dihedral angle ϕ_3 defines the conformation of the dimer and is variable, whereas the other parameters that define the mutual orientation of monomer pairs along the chains, bond angles θ_1 and θ_2, and dihedral angles ϕ_1 and ϕ_2, depend on ϕ_3.

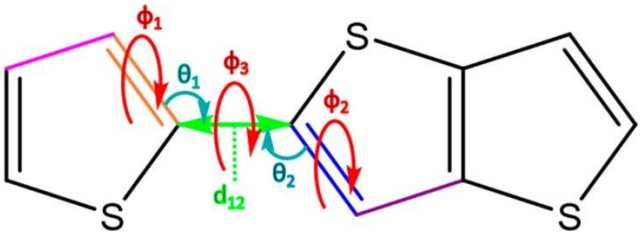

Figure 3.10: Illustration of dimer of thiophene-BTT on which the connection site is defined as the bond highlighted green and the atoms in this bond. Further highlighted are six parameters which defines the mutual orientation of the monomers in the dimer: bond length (light green) d_{12}, bond angles (cyan) θ_1 and θ_2, and dihedral angles (red) ϕ_1, ϕ_2, and ϕ_3.

The parameters d_{12}, θ_1, θ_2, ϕ_1 and ϕ_2, can be obtained using a relaxed torsional scan calculation. In this type of calculation the dihedral angle ϕ_3 is scanned through a specified range in fixed increments (0–180° in 10° degree increments) and the parameters d_{12}, θ_1, θ_2, ϕ_1 and ϕ_2 are allowed

to relax with the rest of the monomer structures in the dimer kept rigid. The values of d_{12}, θ_1, θ_2, ϕ_1 and ϕ_2 are then extracted for each point in the scan, corresponding to a value of ϕ_3. The torsional scan is done at a higher level of theory, B3LYP/6-311G+** in this work, which is justified for these calculations as the parameters extracted from them calculations can be reused for any identical monomer pair with the same connectivity. Once extracted from the torsional scan calculation output, the parameters calculated for each monomer pair and dihedral angle ϕ_3 are used to build the dimer fragments for the single point energy calculations to obtain the fragment matrices. The dimers for each monomer pair and dihedral angle ϕ_3 are built by connecting the two monomers at their connection sites setting the connectivity with the corresponding values of d_{12}, θ_1, θ_2, ϕ_1 and ϕ_2 and then single point calculations are done with each dimer structure. Using the single point calculation output, fragment matrices are calculated as described in section 3.1 of this chapter and a file is stored containing the Fock and overlap matrices for each dimer, identified by the monomer pair and dihedral angle. The fragment matrices can be retrieved from each file when building the polymer chain.

There are multiple ways to generate the monomer block matrices containing the elements arising from coupling involving LMOs on the same monomer and three different methods were tested, the results for which are outlined in Appendix S1. The best method for obtaining these matrix elements with respect to accuracy of the MO energies obtained from LMOM compared to an exact calculation for a planar six-monomer polythiophene chain was found to be using the full set of matrix elements calculated for a monomer fragment bonded at both of its connection sites to 2 other monomers. This method allows the perturbation of the monomer MO energies by other monomers along the polymer chain to be incorporated into the modelling. This “embedded” monomer method is illustrated in Figure 3.11; the single point calculation is done with the embedded monomer in a trimer fragment bonded to two other terminal monomers and the LMO basis trimer Fock and overlap matrices are obtained using 3.1.3 and 3.1.4., then the block of elements involving coupling

between LMOs on the embedded monomer are extracted to a file that is stored, uniquely identified by that monomer.

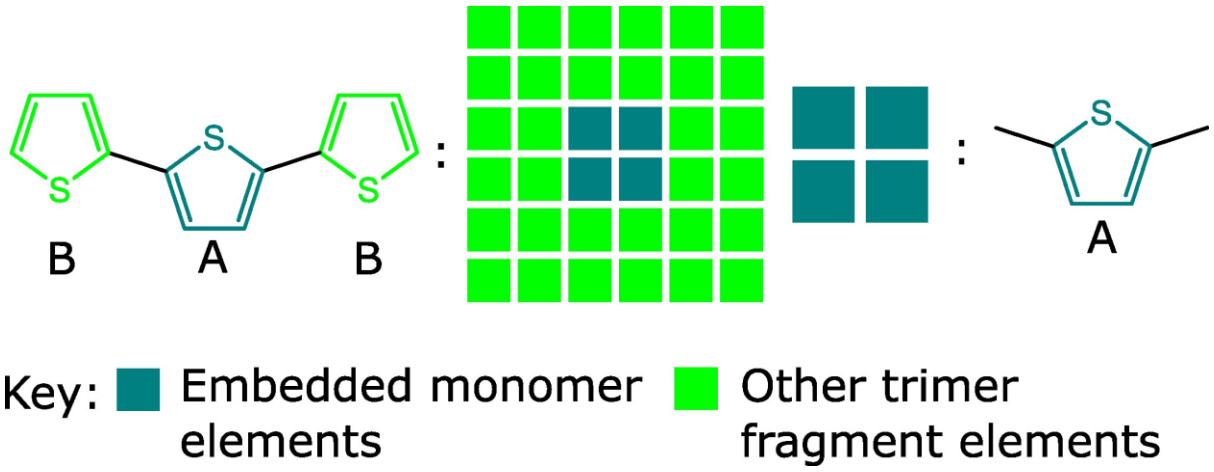

Figure 3.11: The method for obtaining monomer block matrix elements from a monomer A "embedded" (dark green) between two other monomers B (green) in a trimer fragment. The elements arising from coupling between LMOs on the embedded monomer A (dark green) are extracted from the rest of the trimer fragment matrix elements (green).

Figure 3.12 illustrates the overall implemented method for building the polymer chain matrix. The generated files containing the monomer and dimer block matrices can be stored in a database, reusable for calculations done with the same level of theory employed in the single point calculations done to obtain the matrices. For a single polymer chain, the method goes along its sequence, containing N monomers and N-1 adjacent monomer pairs with dihedral angles, and builds the polymer chain matrices by extracting them from the files and populating the elements corresponding to the positions the monomers and monomer pairs occur along the chain. The method was implemented in Python for this work, but any programming language with similar functionality for array-like data would also be suitable.

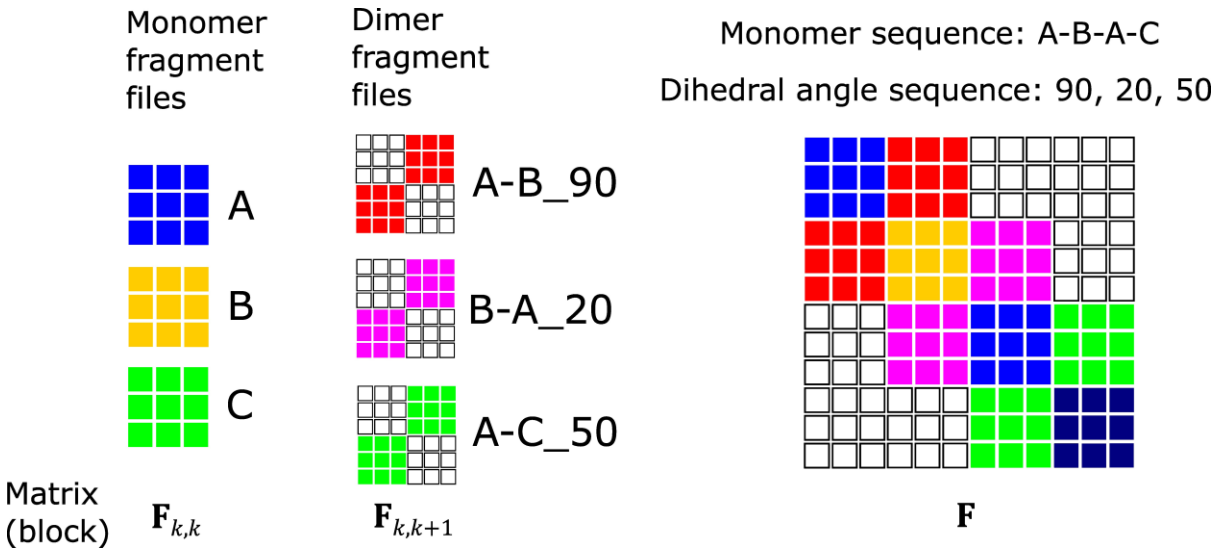

Figure 3.12: A graphical summary of the implemented scheme for building the polymer chain matrix $\mathbf{F}$ (same process for overlap matrix $\mathbf{S}$) for an example sequence with 4 monomers A-B-A-C and 3 dihedral angles (in degrees). The fragment matrices for matrix blocks $\mathbf{F}_{k,k}$ and $\mathbf{F}_{k,k+1}$ are fetched from stored files and the polymer chain matrix $\mathbf{F}$ is populated using the fragment matrix elements. Colored squares are non-zero elements, white squares are zero elements.

The next part of the LMOM implementation is the calculation of the polymer chain electronic structure, which involves obtaining the MOs and their energies for the polymer chains. The electronic structure is calculated using the Roothaan equations given in 3.1.2 and the polymer chain matrices obtained using LMOM; however, there will be some error in the energies obtained resulting from the approximations invoked in the calculation. Further improvements can be obtained post LMOM calculation by applying a calibration, with which the initial LMOM calculated MO energies are corrected to obtain energies closer to those from a full quantum mechanical calculation (full calculation). For 2 polymers from the sample in section 3.2, polythiophene and PDPP2TT, Figure 3.13 shows there is a possible linear and polynomial curve correlation between the full calculation and initial LMOM calculation energies. The region of most interest is the energies in the vicinity of the band edge which contribute to the band edge characteristics, highlighted with red points in Figure 3.13, thus the calibration can be applied selectively to these energies only.

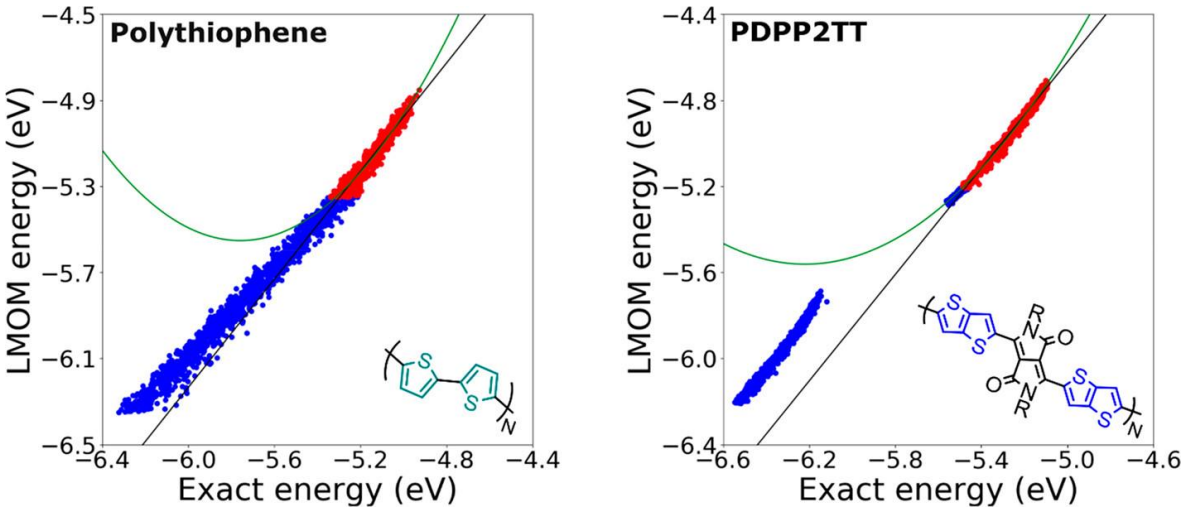

Figure 3.13: Plot of LMOM calculated energies vs exact calculation energies, shown as scatter points (red, blue), for 100-chain samples of 48-mer polythiophene (left) and PDPP2TT (right) chains. Fitting was done using energies within 1.5 eV of the valence band edge and points within 0.5 eV of the band edge are highlighted in red. The best-fit lines for the linear and curved fittings (black and green, respectively) are shown.

The linear and polynomial fitting equations are given in equations 3.3.1 and 3.3.2, where the pre-factors of the x terms m, a and b, and intercept constant c are the calibration parameters.

$$y = mx + c \tag{3.3.1}$$

$$y = ax^2 + bx + c \tag{3.3.2}$$

Typically, LMOM calculations involve around 100 chains, a high number needed for simulating the bulk polymer material. Fitting of the LMOM calculated energies to those from the full calculation and with the same number of full-length chains is the most optimal method; however, this is computationally expensive and slow, precluding a rapid method. Thus, a calibration fitting is done with shorter and fewer chains and the parameters obtained from this fitting are used to correct the energies from calculations with the full-size chains. The energies from the LMOM and full quantum mechanical calculations with shorter length chains and smaller chain numbers are fitted to the functions in 3.3.1 and 3.3.2. The chain lengths (in monomers) used for calculating the calibration parameters were chosen to be multiples of the SRU lengths of each polymer and number of chains

to be multiples of 5, with 100 chains being the full number of chains in the calculations used to obtain results in later sections. The calibrated energies E'_{LMOM} are obtained with the parameters obtained from the linear and polynomial fitting of the energies from the initial LMOM calculation E_{LMOM} and exact calculation E_{FC} using 3.3.3 and 3.3.4. The quality of fit is assessed by the root mean squared error $RMSE_{fit}$ between the energies E'_{LMOM} and E_{FC}, given in equation 3.3.5.

$$E'_{LMOM} = \frac{E_{LMOM} - c}{m} \tag{3.3.3}$$

$$E'_{LMOM} = aE_{LMOM}{}^2 + bE_{LMOM} + c \tag{3.3.4}$$

$$RMSE_{fit} = \sqrt{\frac{E'_{LMOM} - E_{FC}}{N}} \tag{3.3.5}$$

Tables S1 and S2 in Appendix S2 show the results from the fitting of the full calculation and calibrated LMOM calculation energies calculated using calibration parameters obtained with a range of chain lengths and different numbers of chains for two polymers, polythiophene and PDPP2TT from the sample in section 3.2. Based on the results in Appendix S2 the method implemented in this work for obtaining the calibration parameters is to use a linear fitting with the energies calculated for 5 chains each of chain length equivalent to 3 repeat units and applied only to the energies within 0.5 eV of the valence band edge. The effect of calibration on DOS(E), calculated using equation 2.1.11 from Chapter 2, is shown in Figure 3.14, comparing the DOS(E) calculated using LMOM energies before calibration and post-calibration, and energies from the exact calculation. Calibration has a visible effect in shifting the DOS(E) obtained from the initial LMOM calculation closer to the exact calculation result, and performs similarly for all the polymers.

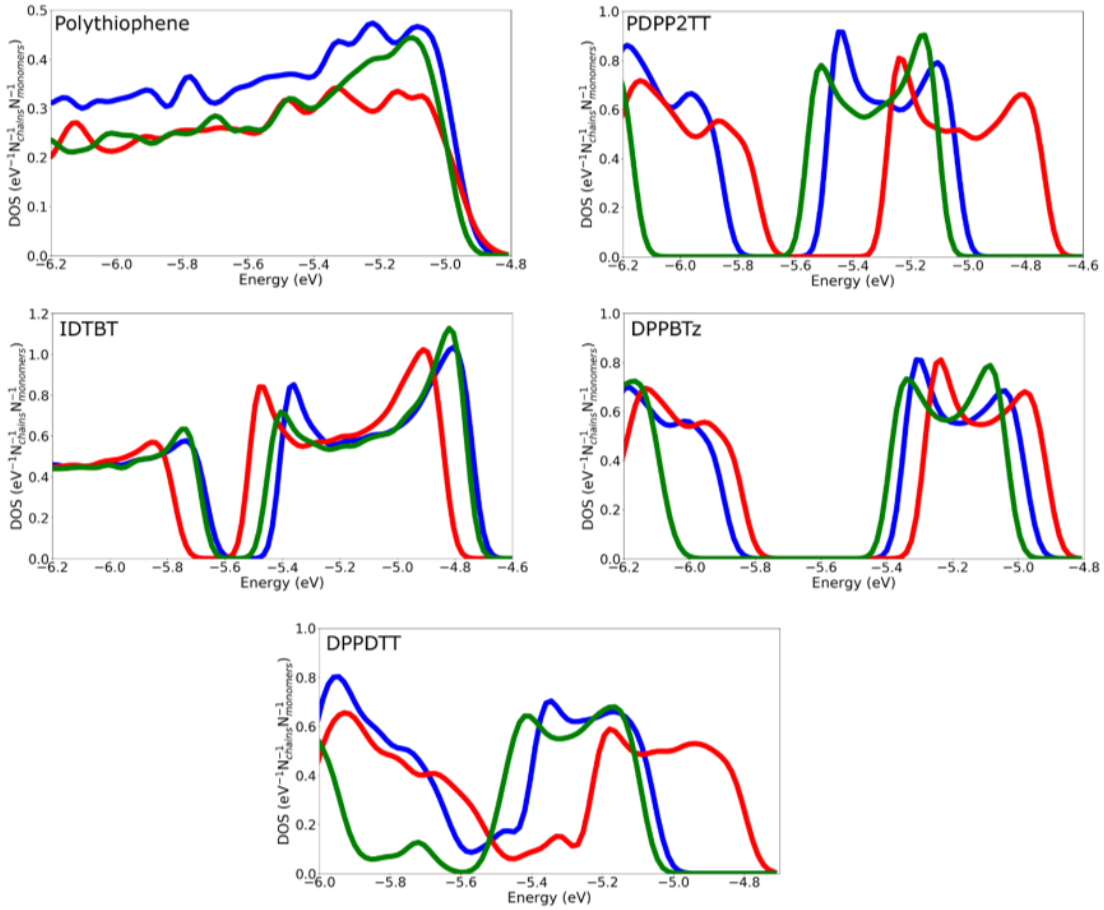

Figure 3.14: Comparison of the DOS(E) calculated using the LMOM energies before calibration (red), LMOM energies after calibration (blue) and exact energies (green) for polymers from the sample shown in section 4.2. The calibrated LMOM energies were obtained for each polymer with a sample containing 5 different chains each being 12-monomers long and the calibration applied to energies within 0.5 eV from the valence band edge.

3.4 Simulating the bulk polymer

The generation of realistic conformations for the polymer chains is required to simulate the bulk polymer, which is needed for calculations of the density of states and calibration parameters for correcting the LMOM calculated energies outlined in the previous section. The polymer conformation is defined as the sequence of N-1 dihedral angles ϕ_3 that determine the mutual geometry between the adjacent monomer pairs of the N monomers in the polymer chain. Values of ϕ_3 for each adjacent monomer pair were allowed to vary within the range of 0–180° inclusive in 10°

increments, giving N = 19 possible ϕ_3 values. Boltzmann statistics was used to select individual ϕ_3 values for each adjacent monomer pair along the chain. The probability p_s of selecting a certain value of ϕ_3, indexed by *s*, is calculated using 3.4.1.

$$p_s = \frac{e^{-\varepsilon_s/k_B T}}{\sum_{t=1}^{N} e^{-\varepsilon_t/k_B T}} \tag{3.4.1}$$

k_B is the Boltzmann constant and the system temperature T is set at 300 K. The torsional energy ε_s is obtained from a single point energy calculation at B3LYP/6-311G+** for the dimer of the adjacent monomer pair indexed by *s* oriented at dihedral angle ϕ_3. For each monomer pair, the values of ε_s calculated at each ϕ_3 are stored in its own file as a torsional potential (ε_s as a function of ϕ_3) along with the values of p_s to be used when selecting dihedral angles in generating the polymer chain configuration. The algorithm to generate the polymer chain conformation using the probabilities p_s is illustrated in Figure 3.15, which generates the chain conformation as a list of dihedral angles ϕ_3. The steps of the algorithm are as follows: 1) the list of adjacent monomer pairs is generated from the polymer sequence, 2) for the first adjacent monomer pair in the list the p_s values are read from file and cumulative probabilities $p_{cumul,s}$ are calculated using the p_s values for each dihedral angle ϕ_3, 3) a random number generator gives a number p_{rand} in the range [0,1], 4) the dihedral angle ϕ_3 is selected if $p_{cumul,s-1} < p_{rand} \leq p_{cumul,s}$ and added to a list that will contain all ϕ_3 selected, 5) steps 2-4 are repeated for the next adjacent monomer pair in the list from step 1 until no more pairs are left. The conformation is generated assuming that the geometry of each adjacent monomer pair is independent of the other monomers in the chain, and thus the resulting polymer chain geometry is not relaxed further.

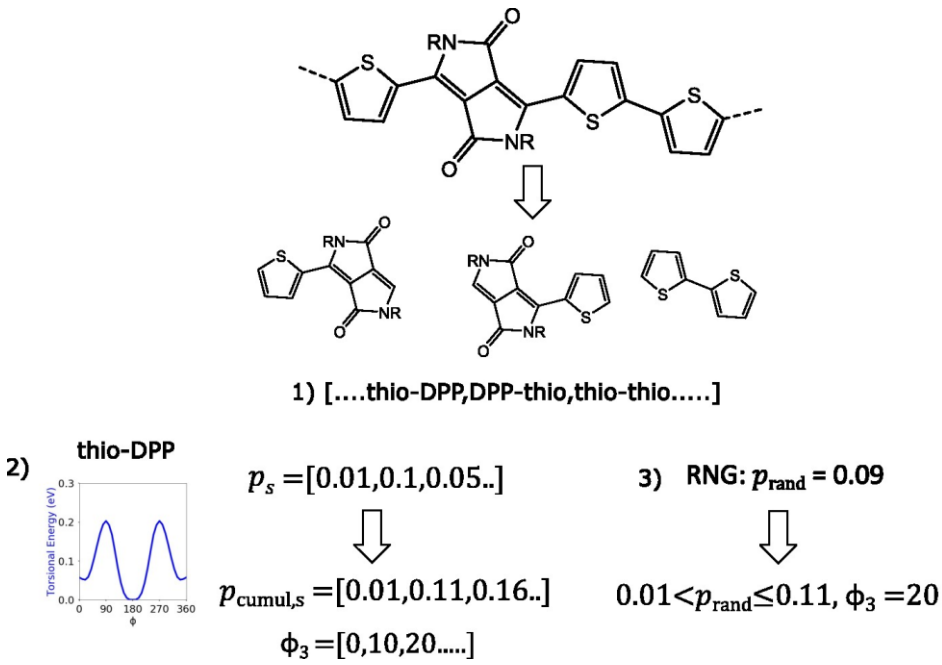

Figure 3.15: Algorithm to pick the dihedral angle for an adjacent monomer pair with example probabilities shown with illustrations of steps 1)-3) shown. Boundaries bounded by the example cumulative probabilities $p_{cumul,s}$ calculated from p_s values for each dihedral angle ϕ_3 of a monomer pair are shown as a list.

This method of conformation generation described has the feature of accounting for the difference between syn- and anti-conformers. Figure 3.16 shows the torsional potential energy and HOMO/HOMO-1 coupling dependence on the dihedral angle ϕ_3 for the monomer pairs that occur in the polymers described in section 3.2, which shows the main difference between syn- and anti-conformers is in the torsional potential energy, where ϕ_3 is close to 0 and 180°. The dependence of the coupling on ϕ_3 however is similar for both syn- and anti-conformers where only the sign is reversed going from one to the other. The size of barriers (peaks) in the torsional potential varies across the polymers, thus the fluctuation of ϕ_3 in the conformations generated differs for each polymer and results in different levels of disorder in the chains depending on the monomer pairs contained in the polymer repeat units.

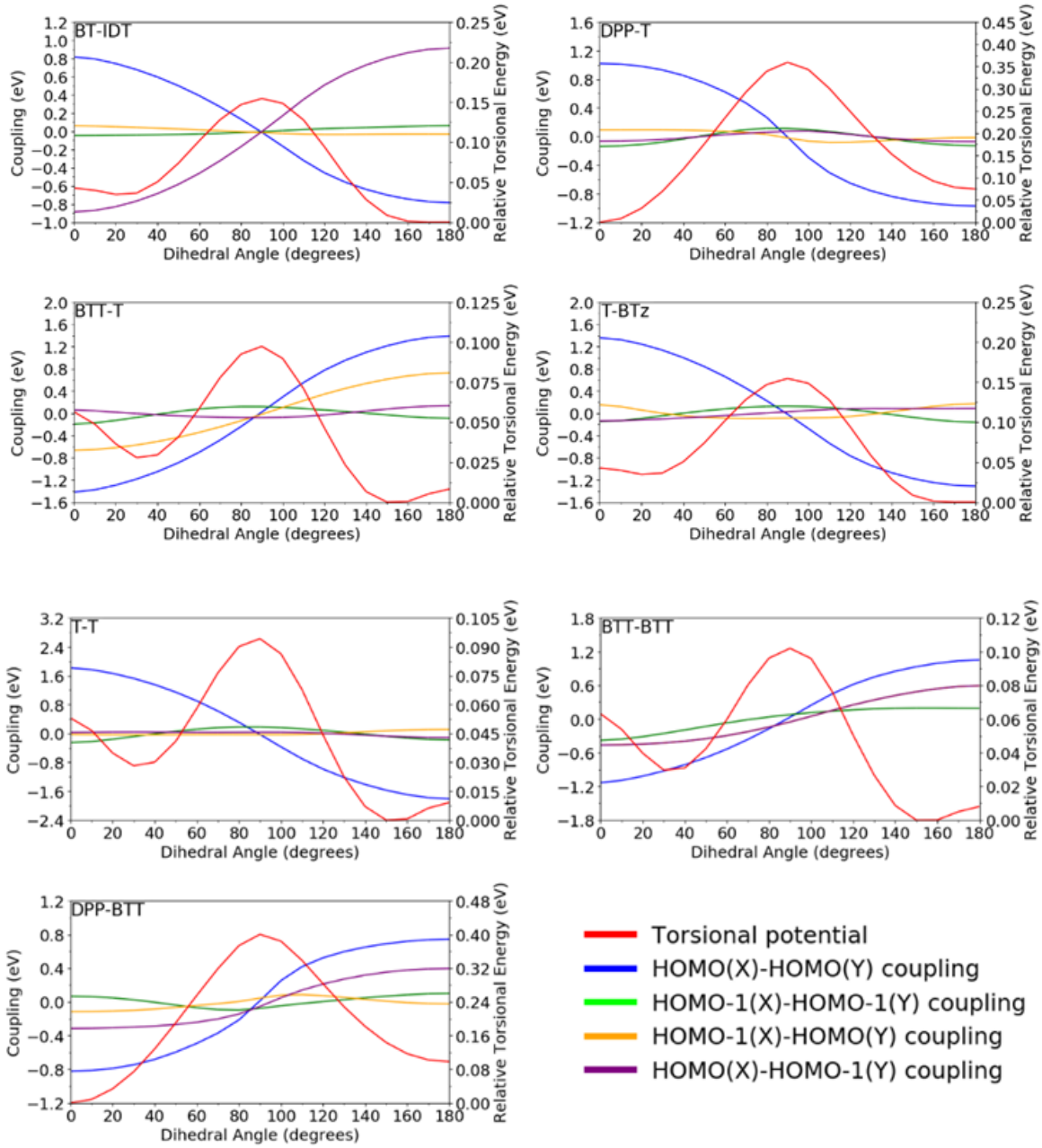

Figure 3.16: Dihedral angle (parameter ϕ_3 in Figure 3.10) vs scaled torsional energy of the dimers which are monomer pairs that occur in IDTBT, DPPBTz, DPPDTT, polythiophene and PDPP2TT. Also plotted are the HOMO to HOMO, HOMO-1 to HOMO-1, and permutations of HOMO to HOMO-1 couplings vs the dihedral angle, with coupling permutations distinguished by the variables X and Y, which are the abbreviated monomer names separated by a hyphen in the top left of each plot (for example, in BT-IDT X=BT and Y=IDT), in the parentheses.

3.5 Characterizing the electronic structure of bulk polymer materials

The electronic structure characteristics of polymers can be used to infer and compare them for mobility. Several measures can be employed based on the density of states calculated for the polymers, and the localisation of the orbitals along the chains. The features at the DOS band edge have been found in previous work to correlate with the hole mobility and suggests that the narrowness of the tail state distribution, the tail width, at DOS band edge is indicative of high mobility polymers.[20] The valence band edge E_{EDGE} is defined as the energy at which the inflection point on the DOS closest to the band gap occurs. The measure for the narrowness of the tail width in this work is the tail slope, defined as the gradient of the DOS(E) at E_{EDGE} and is -∞ (vertical edge) for a perfectly ordered 1D chain, thus indicating the electronic disorder in a material. The method for calculating the tail slope used in this work is outlined in Appendix S3. Figure 3.17 illustrates the definitions of E_{EDGE} and the tail slope on the DOS.

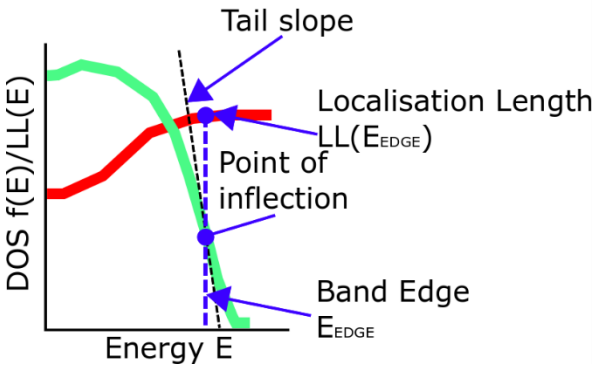

Figure 3.17: Illustration of the features at the valence band edge used to define measures for characterizing polymers. The band edge E_{EDGE} is denoted by the dotted blue line which crosses the point of inflection along the tail edge of DOS(E) that defines the tail slope.

The polymers are also characterized by a measure of the orbital localisation in chains. To define this measure, the contribution of monomer MOs to the chain MOs must first be calculated, given by the weight $P_k^{(m)}$ of MO m on a monomer with index k in the chain (eq. 3.5.1). $C_i^{(m)}$ are the coefficients of MO m where the index i runs along the basis of LMOs (the basis set constituting of the π-MOs from the monomers).

$$P_k^{(m)} = \sum_{\substack{i\ (on\ monomer\ k) \\ j\ (on\ monomer\ l)}} C_i^{(m)} S_{ij} C_j^{(m)} \quad (3.5.1)$$

Another localisation parameter also calculated is the centroid $R^{(m)}$ of chain MO *m* (eq. 3.5.2).

$$\mathbf{R^{(m)}} = \sum_k P_k^{(m)} \mathbf{r_k} \quad (3.5.2)$$

In $R^{(m)}$, $\mathbf{r_k}$ denotes the center of mass of monomer segment k in cartesian coordinates, calculated using $\mathbf{r_k} = \sum_{i=1}^{n} m_i \mathbf{r_i} / \sum_{i=1}^{n} m_i$ where i is an index running over all the n atoms in the monomer segment and $\mathbf{r_i}$ is the position of atom i in cartesian coordinates. Using 3.5.1 and 3.5.2 the measure of orbital localisation along a single chain, localisation length $LL^{(m)}$ of chain MO m, can be calculated and is given in eq. 3.5.3.

$$LL^{(m)} = 2\sqrt{\sum_k |\mathbf{r_k} - \mathbf{R^{(m)}}|^2 P_k^{(m)}} \quad (3.5.3)$$

To characterize the orbital localisation in the bulk polymer, the energy dependent localisation length $LL(E)^{(m)}$ (or LL(E)) in eq 3.5.4, which measures the averaged localisation of MOs in the region of energy E is calculated using $LL^{(m)}$.

$$LL(E)^{(m)} = \frac{\sum_m LL^{(m)} \delta(E - E_m)}{\sum_m \delta(E - E_m)} = \frac{\sum_m LL^{(m)} g(E - E_m)}{\sum_m g(E - E_m)} \quad (3.5.4)$$

As the polymer chains studied in this work have monomers of varying length, the spread of the MOs on each monomer will differ. Thus, the localisation length provides an ideal measure in terms of real molecular dimensions. Holes occupy states near the band edge, therefore the localisation length at the band edge $LL(E_{EDGE})$ is of most interest when comparing the polymers shown in Figure 3.9.

Lastly, the DOS(E) for each polymer will be characterized by the bandwidth of the valence band, approximately measured as the distance in energy between E_{EDGE} and the edge of the band where the density drops below ~10^{-3}.

3.6 Results

This section will discuss the results of the calculations done for polymers described in section 3.2, with comparisons of the polymers focusing on the DOS features, and how they correspond to the molecular and electronic features of the polymers. Figure 3.18 shows the DOS(E) and LL(E) calculated for the polymers using the methods outlined in sections 3.1-3.5 with energy level diagrams above for the structural repeating units with the HOMO energies calculated for the monomers in their isolated forms, and for each monomer pair in the SRUs is shown the mean average magnitude of the HOMO-HOMO coupling over all the chains and the fluctuation, which is a standard deviation, of this coupling in brackets. The DOS(E) was calculated as using the form of equation 2.2.1 in Chapter 2 with the spectra of energies for the polymers broadened using a Gaussian function g with σ=0.008 eV for all polymers described in section 3.2 except polythiophene with a DOS(E) broadened using σ=0.012 eV. Table 2 also shows several key figures of merit for each polymer; the experimental hole mobility, valence band edge E_{EDGE}, tail slope at the band edge, valence bandwidth, and localisation length at the band edge $LL(E_{EDGE})$.

Table 2 – copolymers and key figures of merit for comparison

Polymer	IDTBT[18]	DPPBTz[18]	DPPDTT[102]	Polythiophene (P3HT)[12]	PDPP2TT[103]
Hole mobility ($cm^2V^{-1}s^{-1}$)	2.2 (± 0.2)	2.4	1.36 (± 0.26)	0.1	0.037 (± 0.015)
Tail width (eV)	0.13	0.12	0.16	0.17	0.11
Band width (eV)	0.775	0.486	0.443	>1	0.549
LL(E) (Å)/E (eV)	44.47/-4.70	39.21/-4.95	33.28/-5.02	21.01/-4.89	56.52/-5.02
LL (Å)/E (eV)	41.67/-4.70	41.12/-4.95	30.12/-5.02	20.09/-4.89	55.77/-5.02

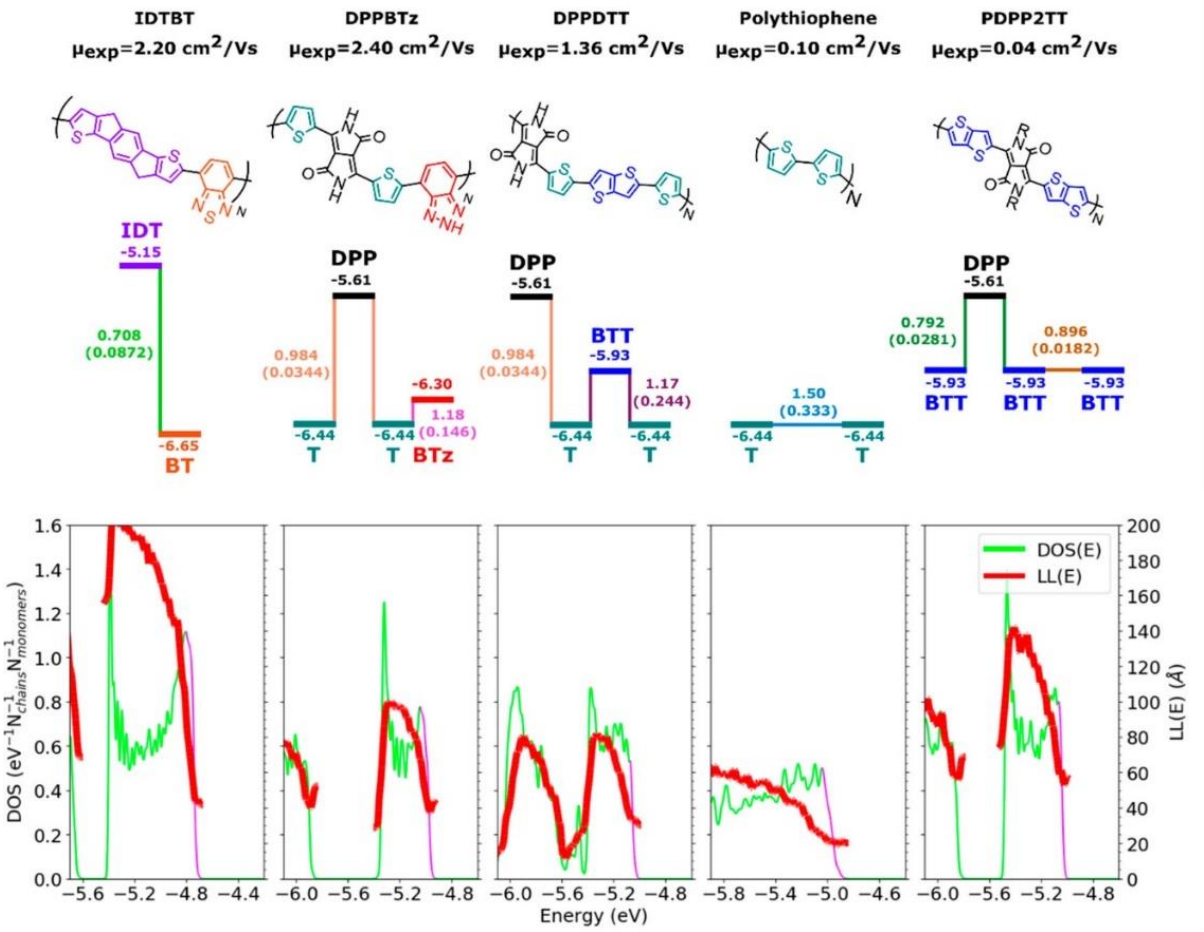

Figure 3.18: (top) Abbreviated names, experimental mobility, and structural repeating units for each polymer sample. (middle) HOMO energies (eV) of each monomer, mean HOMO−HOMO coupling magnitudes between adjacent monomer pairs (eV), and their corresponding standard deviation in parentheses. Height of horizontal-coloured segments indicates their relative position in energy. (bottom) Normalized DOS(E) and energy-dependent localisation lengths LL(E) for the corresponding polymer. The purple segments at the band edge of each DOS(E) is the edge along which the tail slopes are calculated.

To justify the focus on the monomer HOMO energies as shown in Figure 3.18, a series of LMOM calculations using a basis set that includes only the HOMO orbitals on each monomer were done to calculate the DOS(E) and LL(E) for each polymer in a similar fashion as that done with the full basis set, the results of which are shown in Figure 3.19. Using the HOMO only basis set, almost all the key electronic characteristics are quantitatively reproduced, thus allowing the interpretation of the results in terms of the relative energy of the HOMO localised on separate monomer fragments, their

coupling, and the fluctuation in this coupling arising from the conformational disorder in the polymer.

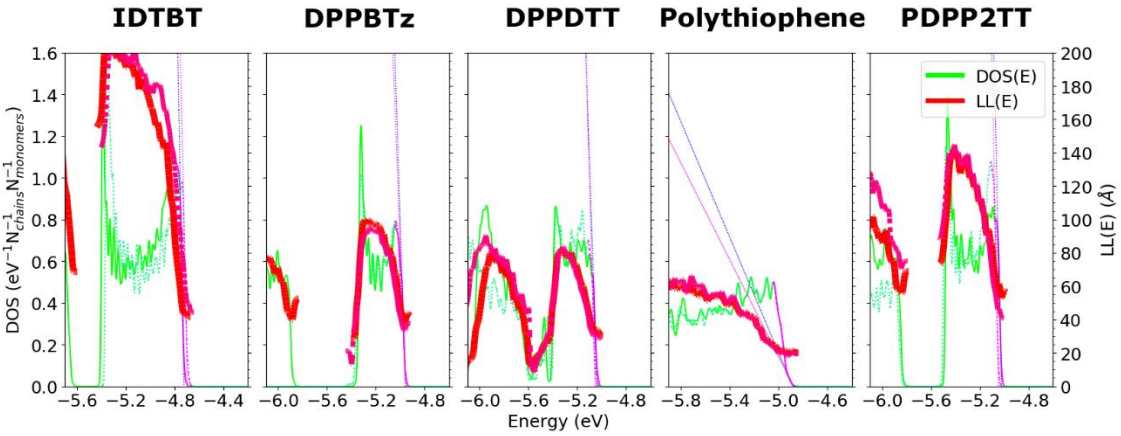

Figure 3.19: DOS(E) and LL(E) calculated with energies from full π-MO basis set (red and green plots) and HOMO only basis set (dashed blue-colour shifted red and green plots) LMOM calculations for IDTBT, DPPBTz, DPPDTT, polythiophene and PDPP2TT. DOS(E) tail slopes are represented as dotted lines (blue for full π-MO basis set calculations and purple for HOMO only basis set calculations). The purple segments at the band edge of each DOS(E) is the edge along which the tail slopes are calculated.

An important feature of the results in Figure 3.19 is that each calculated DOS show the expected band splitting of varying widths with two distinct bands each for the donor-acceptor copolymers (IDT-BT, DPP-BTT, DPP-2TT and PDPP-2TT) and a single band for the homopolymer polythiophene shows no band splitting, as predicted elsewhere.[79] The energy splitting between the bands of the DA copolymers is correlated with the energy difference between the HOMO levels of the monomers. The bandwidth of the valence band depends on the effective coupling due to the superexchange interaction between the (nonadjacent) monomers with highest HOMO energies.[104] IDTBT shows the largest band splitting, having the shortest separation between the high-HOMO energy monomers and thus the largest bandwidth, and the smaller splitting is seen for DPP-DTT and PDPP2TT, which can be conversely attributed to the weaker superexchange interaction through three nondegenerate monomers between the DPP units.[104]

There is an apparent trend across the tail width and the localisation of the MOs near the band edge, as measured by the tail slope and $LL(E_{EDGE})$, across the polymers studied. The tail slope decreases steepness in the order IDTBT > PDPP2TT > DPPBTz > DPPDTT > polythiophene, while the localisation length at the band edge $LL(E_{EDGE})$ decreases in the order of PDPP2TT > IDTBT > DPPBTz > DPPDTT > polythiophene. Figure 3.20 shows the plot of $LL(E)$ and DOS(E) for each polymer in the region of the valence band tail, with the tail slope illustrated at E_{EDGE}.

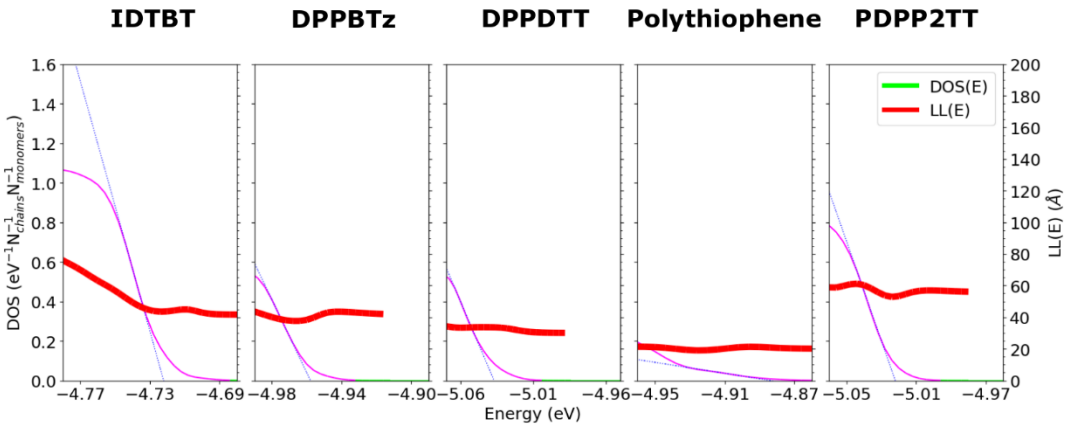

Figure 3.20: Comparison of the tail slope (shown as dotted blue lines) at the band edge of the DOS(E) for the 5 polymers IDTBT, DPPBTz, DPPDTT, polythiophene and PDPP2TT.

Both trends can be attributed to the different degrees of electronic disorder present within the polymers. Disorder manifests in the HOMO−HOMO coupling fluctuation due to different torsional potential between monomers, which causes broadening in the distribution of MO energies and results in more localised states along the chains. The steepest tail slopes and highest $LL(E_{EDGE})$ are seen for IDTBT and PDPP2TT, which have the lowest HOMO−HOMO coupling fluctuation throughout their chains and their monomer pairs all exhibiting fluctuations below 0.1 eV, whereas fluctuations above 0.1 eV are seen in the monomer pairs within the other polymers. The difference in $LL(E_{EDGE})$ between PDPP2TT and IDTBT can be attributed to the rigidness of the monomer pair units, measured by the spread of the dihedral angle with torsional energy ≤ k_BT resulting from the conformation generation method in section 4.4, shown for all monomer pairs in Table 3.

Table 3 – Monomer pairs and their most probable dihedral angles

Monomer pair	Dihedral angle at (interpolated) global torsional energy minimum (degrees)	Spread of dihedral angles with torsional energy ≤ k_BT (T=298.15 K) (degrees)
T-T	154	52
BTT-BTT	155	50
DPP-BTT	0	18
BT-IDT	169	39
DPP-T	0	19
BTT-T	154	52
T-BTz	169	39

The DPP-BTT unit in PDPP2TT is more rigid compared to the BT-IDT unit in IDTBT, and is twice as frequent in PDPP2TT chains than the more flexible BTT-BTT unit, thus overall PDPP2TT chains should be less disordered than IDTBT chains. DPPBTz has the TBTz pair which has a HOMO−HOMO coupling fluctuation of 0.146 eV, greater than 0.1 eV, showing a lower $LL(E_{EDGE})$ and much less steep tail slope than IDTBT. The lowest $LL(E_{EDGE})$ values and least steep tail slopes are seen for DPPDTT and polythiophene. The T-BTT pair of DPPDTT shows a HOMO−HOMO coupling fluctuation of 0.244 eV which is double that of the T-BTz pair in DPPBTz, and the T-T pair in polythiophene shows a coupling fluctuation much higher at 0.333 eV. The variation in the torsional potential minima depth for the different monomer pairs affects the fluctuation in the HOMO−HOMO coupling, where in the monomer pairs contained in the polymer sample studied (Figure 3.19) torsional potentials between monomer pairs that display a double minimum near planarity (BTT-T and T-T) or an extremely flat minimum in the planar configuration (T-BTz) are associated with the largest coupling fluctuations seen.

The trend in $LL(E_{EDGE})$ and tail width for PDPP2TT, IDTBT, DPPBTz, and DPPDTT show some correspondence with experimentally measured mobility values quoted in Figure 3.19. It has been previously suggested that a narrow distribution of tail states at the DOS band edge is a characteristic of high mobility polymers.[20, 93] Thus, the observed tail widths, as measured by the tail slope, from the calculations in this work can be compared to experimental mobility data. A comparison with experiment tail widths is available for IDTBT, DPPBTz and DPPDTT obtained from the

spectroscopically obtained DOS by Nikolka et al., where the method in this work correctly reproduces the order of tail width reported from experiment, which is narrowest for IDTBT, then DPPBTz, with DPPDTT showing the widest tail state distribution.[93] The break in the trend with respect to $LL(E_{EDGE})$, DOS tail width, and experimental mobility occurs for PDPP2TT, which is attributed to the use of idealized chains in the method for this work. It was proposed previously by Bronstein et al. that side-chain effects in real PDPP2TT leads to the lower than expected experimentally measured mobility.[103] The use of idealised chains for the calculations in this work assumes a model based solely on the monomer sequence, and will fail to include the supramolecular effects that contribute to chain conformations.[105-107]

4.7 Conclusion

In the work outlined in this chapter, a method for rapidly computing the electronic structure for large samples of polymer chains in different conformations was demonstrated. Using a tight binding method and additional calibration steps to improve the energies reasonably accurate results were obtained at minimal cost compared to a full quantum calculation. The implementation of the method involves generating fragment matrices which can be used to build the input matrices of full polymer chains in a modular fashion, allowing storage of these fragment matrices in a reusable database, thus making it ideal for screening a large number of polymers while including the fundamental role of structural disorder in their electronic structure.

To illustrate the potential of the methodology for materials design a set of 5 polymers used as p-type semiconductors were considered, containing a diverse range of motifs spanning DA copolymers, homopolymers, small fused and large fused ring monomers. A range of characteristics relevant for charge transport were identified and the relation between the polymer structure and such characteristics were established. An important finding is that all the key parameters related to the density of states and orbital localisation could be deduced by a limited number of polymer

parameters, namely the energy level of the HOMO localised on each monomer and the fluctuation of the coupling between HOMOs localised on adjacent fragment due to the conformational flexibility. Thanks to this analysis the computed properties can be understood in terms of properties of the individual monomers and the interaction with their neighbours making the interpretation of the results straightforward and, more importantly, allowing the exploration of novel chemical designs.

The orbital localisation characteristics and the band tail correlate rather well with the measured mobility, with greater mobility measured for polymers with larger computed localisation length and narrower band tail. One major exception to this trend was noted and it can be attributed to the intrinsic limitation of the method which ignores the additional structural disorder (or order) imposed by the interaction between different chains. Thus, a future investigation could be done to determine the extent to which the observations for the systems of isolated polymers studied in this chapter apply to the bulk phase. Such work could be done using molecular dynamics (MD) plus quantum mechanical (QM) calculations, where the method developed in the work of this chapter would be used to do the QM calculations on polymer chain ensembles generated via MD simulation, with the chain geometries thus obtained modified by replacing monomer units with rigid fragment monomers. It is important to note, however, that while the method accelerates the QM part of the aforementioned calculations this is less impactful to the overall speed of the calculation because the slowest step comes from the MD procedure for generating the chain geometries, as polymers are very slow to equilibrate. An independent source of validation for the method is the agreement in the relative width of the valence band edge tail available for three of the considered polymers.

In summary, this work illustrates how to extract the maximum amount of computationally relevant information for a polymer to be used as a semiconductor without explicitly modelling its microstructure in bulk.[52, 108] The bulk microstructure remains very relevant but explicitly modelling this hinders the possibility of high throughput screening or molecular design and it is therefore

expected that the design will be likely limited to the range of local properties considered in this work. Future applications of this method will explore a wider range of polymers.

Chapter 4

Polymer Screening Using the Localised Molecular Orbital Method

In this chapter, the methodology presented previously in Chapter 3 is demonstrated in a screening type study using a sample of 36 polymers. The work discussed in Chapter 4 has been previously published in reference[109]. Firstly, the screening method is outlined, which is based on correlations between the localisation length and measures defined by structural and electronic features of the polymers studied. The correlations plotted are then rationalised by examining the coupling, torsional and structural features of the polymers. Statistically significant correlations are thus identified and the structure property relations inferred are proposed as design principles. The design principles derived from analysis of the correlations are further examined at the end using a model Hamiltonian.

4.1 Polymer sample for screening

The polymer sample for the screening is derived from structures of polymers reported in reference[8] and contain the addition of novel structural repeating units (SRUs) suggested from collaborators derived from a reported non-fullerene acceptor in reference[110]. From reference[8], polymer backbones from only p-type and ambipolar type polymers were selected for the sample, and idealised SRUs, shown in Figure 4.1, were derived from these by removing or replacing the larger side chains (2+ carbon atoms) with a methyl group (when connected to spiro-carbon atoms) or hydrogen atoms (in all other cases).

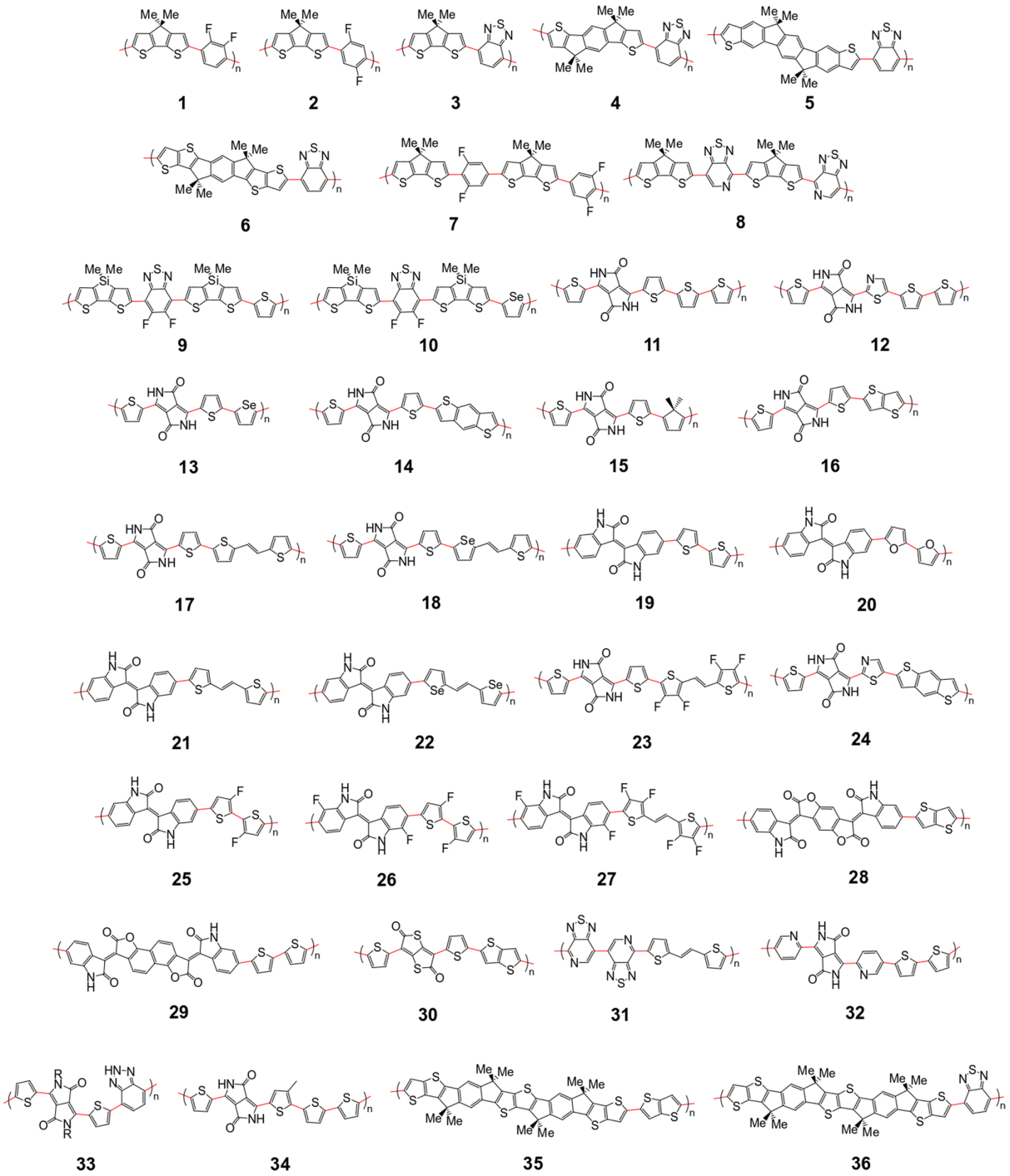

Figure 4.1: Structural repeating units (SRUs) based on polymers selected from reference 8 and from collaborators in the work of this chapter. The red bonds denote connections between individual monomers in the polymer chain.

The monomers used to build the SRUs in Figure 4.1 are shown in Figure 4.2. Each monomer has 2 connection site atoms which other monomers can bond to, which are highlighted with a black circle if they are in a chemically identical environment, while red or blue circles denote connection sites in

chemically inequivalent environments. Each monomer with non-identical connection sites is assigned a label in the SRU sequence to its name indicating how the connection sites are bonded; [A] if the blue connection site atom is bonded to the monomer to its left in the polymer chain sequence and [B] if it is the red connection site atom. Monomers at the start or end of the sequence are labelled with [A] or [B] according to which of its connection sites is bonded to the second or second to last monomer in the chain sequence, respectively.

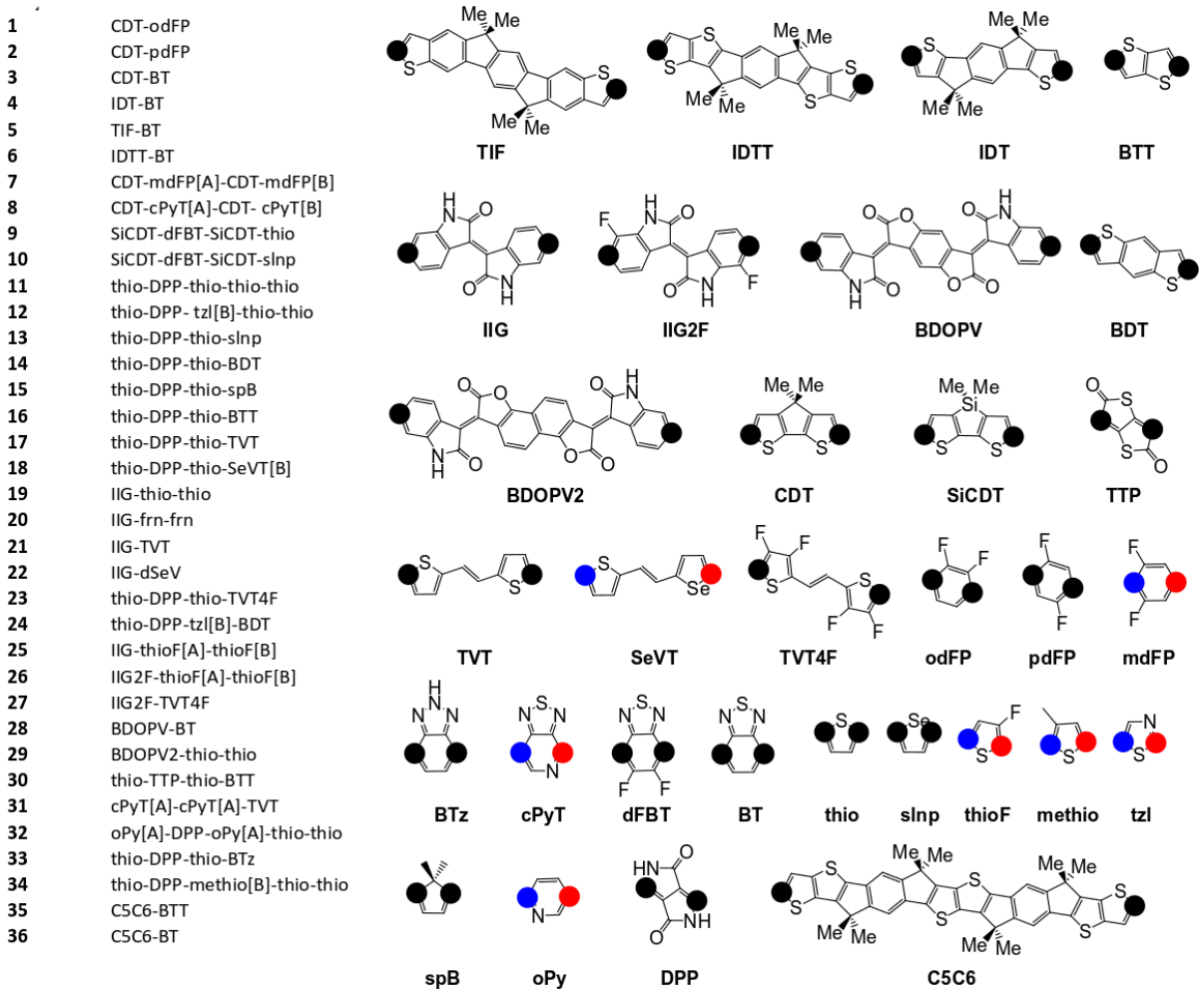

Figure 4.2: Monomers and list of monomer sequences for the polymer SRUs in Figure 5.1. The black circles on each monomer denote the connection sites, while the blue and red coloured circles denote non-equivalent connection sites.

4.2 Methods for electronic structure calculation and characterisation

For each unique polymer in Figure 4.1, the averaged electronic structure is calculated in two independent steps; first, several polymer chain conformations are generated using Boltzmann statistics as outlined in section 3.4 of Chapter 3 and the electronic structure is calculated for each polymer chain using the localised molecular orbital method (LMOM) following the method in section 3.1 and implementation detailed in section 3.3 of Chapter 3.

A polymer chain conformation, given a sequence of rigid monomers, is defined by the sequence of dihedral angles ϕ between the pairs of adjacent monomers in the chain. The latter is generated by selecting the dihedral angles ϕ in the chain with Boltzmann sampling using the torsional potential energies where the absolute system temperature T is set at 300 K. The torsional potentials of each adjacent monomer pair are considered independent of each other and calculated for dimers of each adjacent monomer pair that appear in the polymers, shown in Figure 4.2, at the B3LYP/6-311G+** level. This method for obtaining the coupling explicitly for each ϕ is necessary as there are several orbital couplings which contribute to the overall electronic structure, where the coupling between different MOs is correlated and thus cannot be considered independent for each MO pair. For the polymer chain conformations, 100 conformations of polymer chains containing 48 monomers (or 50 if the repeating units had 5 monomers) are generated, and there is no further relaxation of the conformations once generated. The explicit polymer conformations are required for calculating the localisation length, calculated using the equations and method described in section 3.5 of Chapter 3, which requires the atomic coordinates of the polymer chains to be expressed in realistic molecular scale dimensions and calibration calculations for the LMOM procedure described in section 3.1 and 3.3 of Chapter 3. The LMOM calculations done to obtain the electronic structure of the polymer chains require the onsite energies of the monomer MOs included in the basis set and transfer integral (coupling) matrices for the dimers of adjacent monomer pairs contained in the polymers, shown in Figure 4.2. The basis set for the LMOM calculations is the full set of π-MOs from each

monomer, with the exception of the oPy monomer which has a σ-symmetry HOMO also included and this anomaly is discussed in Figure S5.6 of Appendix S5.

The density of states (DOS) $f(E)$ is computed as $f(E) = \sum_m g(E - E_m)$ where $g(E - E_m)$ is the normalised Gaussian function centred at energy E (data are reported with broadening width 0.016 eV) and E_m is the energy of the molecular orbital (MOs) on the polymer chains from the bulk sample.

4.3 Method for polymer screening

The approach followed for the work in this chapter can be divided into 4 main parts, shown in Figure 4.3. First, a list of polymers reported in literature is compiled which represents a good sample of the current chemical state-of-the-art for p-type semiconducting conjugated polymers. For these polymers, the adjacent monomer pairs from their structural repeating units (SRUs) are identified and the relevant electronic coupling and torsional potentials for the dimers of these monomer pairs are computed as a function of the intermonomer dihedral angle φ. These data are then used to generate polymer chain conformations for calculating the average electronic structure, used to obtain the density of states (DOS) and localisation length. As the last two properties are related to the charge carrier mobility is possible to deduce the features of monomer sequences that promote larger mobility.

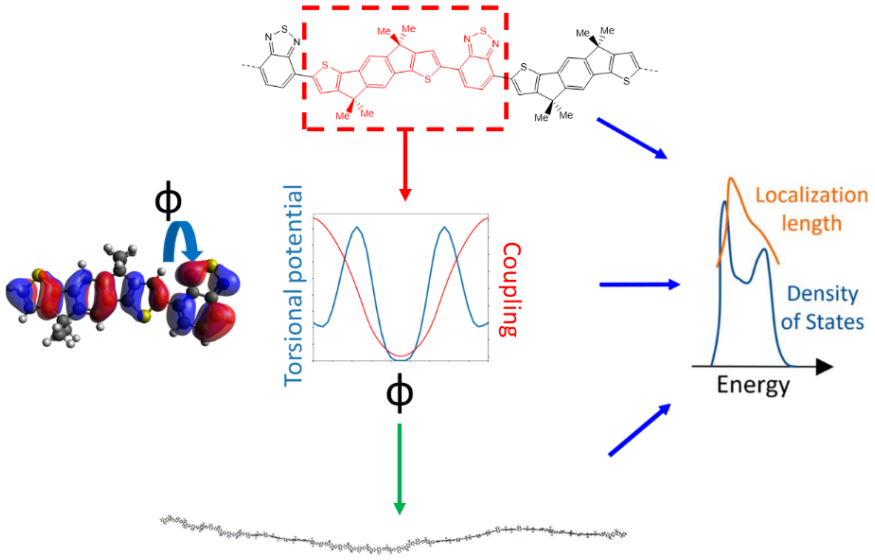

Figure 4.3: Illustrated summary of the methodology for screening a sample of polymers. The adjacent monomer pairs are identified then their torsional potentials and MO coupling are obtained from torsional scans and single point energy calculations using the methodology outlined in Chapter 3. All of these contribute to generating the realistic polymer chain conformations to calculate the density of states and localisation length.

To infer charge transport properties from parameters corresponding to molecular features and thus establish structure property relationships, measures based on these features must be defined in order to characterize the polymers. Such features include MO coupling and torsional potentials, and molecular structure features involving the sequence and size of the monomers and their repeating units in the chains. As previously described in Chapters 2 and 3, the charge carrier mobility has been found experimentally and shown theoretically to be closely correlated with the localisation length and tail state distribution width, the latter measured by the tail slope at the DOS band edge. Thus, localisation length and tail slope at the DOS band edge can be used as proxy properties for charge carrier mobility, and the correlation of any polymers properties with these proxy properties can infer mobility. The strength of the correlation between any two properties is measured using the Spearman rank order correlation coefficient $\rho_{R(X),R(Y)}$, given in equation 4.3.1 for variables *x* and *y* belonging to sets *X* and *Y*.

$$\rho_{R(X),R(Y)} = \frac{n\sum_{x_r\in X_r, y_r\in Y_r} x_r y_r - \sum_{x_r\in X_r} x_r \sum_{y_r\in Y_r} y_r}{\sqrt{n\sum_{x_r\in X_r} {x_r}^2 - (\sum_{x_r\in X_r} x_r)^2}\sqrt{n\sum_{y_r\in Y_r} {y_r}^2 - (\sum_{y_r\in Y_r} y_r)^2}} \quad (4.3.1)$$

Each element *x* and *y* in the datasets for the variables is associated with ranks x_r and y_r from the set of ranks X_r and Y_r, where x_r is the rank order of variable *x* in the set *X* and y_r is the rank order of variable *y* in the set *Y*. $\rho_{R(X),R(Y)} \in [-1,1]$, where negative and positive values indicate monotonically decreasing and increasing relationships between variables x and y, respectively, and the closeness of $|\rho_{R(X),R(Y)}|$ to 1 indicates how strong the relationships between the variables is. The first correlation to be presented here is between the localisation length and the magnitude of the tail slope $|df(E = E_{EDGE})/dE|$, shown in Figure 4.4. While both measures are justifiable choices to use as the proxy property for mobility, with both being linked to transport models[84] and experimental measurement[97], the strong positive correlation between the measures means only one is necessary. Thus, the localisation length at the band edge is chosen as the sole proxy property for mobility.

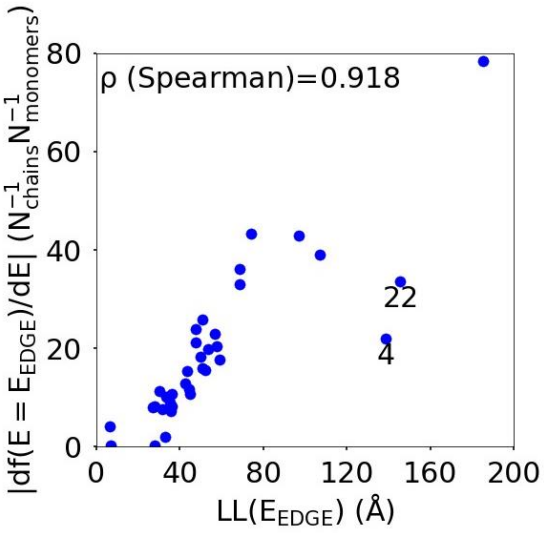

Figure 4.4: Correlation between the localisation length $LL(E_{EDGE})$ and magnitude of tail slope (= $|df(E = E_{EDGE})/dE|$) at the band edge. Outlier points for polymers 4 and 22 are noted on the plot.

The screening method will be based on correlations between the localisation length at the band edge and polymer characteristics defined by the structural, coupling and electronic features shown by the polymers, which are defined in the next section of this chapter. The strength of the correlation coefficient $\rho_{R(X),R(Y)}$ defined in equation 4.3.1 will be used to infer the structure property relation for the polymer properties related to the measure being compared against the localisation length at the band edge.

As will be discussed in subsequent sections of this chapter, there are two descriptors of the coupling between consecutive monomers that are particularly important; the *mean average coupling magnitude* $\langle|J_{i,i+1}|\rangle$ between HOMO orbitals localised on consecutive monomer *i* and *i+1* and the standard deviation of such matrix elements $\sigma_{i,i+1}$ due to the conformations explored by the chains which will be referred to as the *fluctuation* of the (HOMO-HOMO) coupling. Concomitantly, *relative coupling fluctuation* $\sigma_{i,i+1}^{\mathrm{rel}}$ will also be calculated, where $\sigma_{i,i+1}^{\mathrm{rel}} = \sigma_{i,i+1}/\langle|J_{il}|\rangle$.

4.4 Main trends

It was previously shown in Chapter 3 that for 5 model polymers the DOS and localisation length at the band edge were predominantly influenced by the relative position of the HOMO energy levels of the monomers and fluctuations in the coupling between the HOMOs on adjacent monomers along the polymer SRU.[111] The localisation length at the band edge is likely determined by the sequence of on-site energies, the strength of the HOMO-HOMO coupling and the fluctuation of this coupling. To visualize all these features in a single diagram and guide the analysis, for each polymer an energy level diagram of the HOMO orbitals on each monomer of the sequence is shown, contained in Figure 4.5, and the polymers are ordered from the lowest (polymer 18) to highest $LL(E_{EDGE})$ (polymer 36). On the energy level diagrams, larger vertical separation between the HOMO levels corresponds to larger energy separation. The lines connecting the orbital levels indicate the strength of the coupling

(thicker lines have larger average coupling $\langle|J_{i,i+1}|\rangle$) and the relative fluctuation of such coupling $\sigma_{i,i+1}^{\mathrm{rel}}$ (using the colour code given in Figure 4.5).

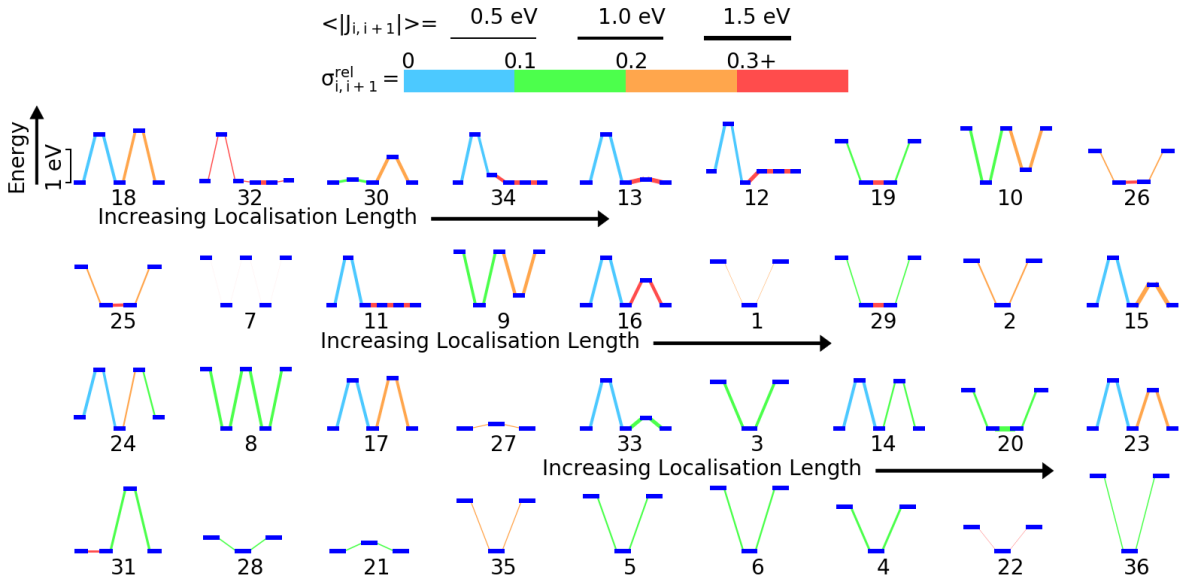

Figure 4.5: Orbital energy level diagrams for each polymer ordered left to right and top to bottom from lowest (for polymer 18) to highest (for polymer 36) localisation length. The same energy scale, shown on the top left, is used for all diagrams. In each orbital energy level diagram, the horizontal blue lines represent the HOMO energy levels localised on each monomer (the energy difference are in scale across the diagram). The line connecting the HOMO levels encodes the strength of the average coupling (thicker lines correspond to stronger coupling $\langle|J_{i,i+1}|\rangle$ as shown in the top part of the figure) and the fluctuation of the coupling $\sigma_{rel}(|J_{il}|)$ (using the colour code given in the top part of the figure).

There are three key trends apparent from Figure 4.5. The first is that A-B type polymers (2 monomers only in the structural repeating unit) appear to have higher localisation length than non A-B type polymers (the 8 polymers with highest localisation length contains 2 monomers in the structural repeating unit). Second, the localisation length appears to be affected by the size of the difference in HOMO energies on adjacent monomers along the polymer SRU; in A-B type polymers, a higher difference in HOMO energy appears to give higher localisation length. Lastly, there appears to be a tendency to have lower fluctuation in the coupling for individual monomer pairs in the polymers on the higher end of localisation length and strong coupling fluctuation between at least

one pair of consecutive monomers for low localisation length polymers. The correlations between localisation length and properties of the polymers will be examined in the subsequent sections.

To rationalize the results is it useful to consider a limited number of parameters of the model. In particular, it is very convenient to consider the energy and coupling fluctuation of only the localised HOMO on each fragment, an approach that appears to be generally well-justified. In Figure 4.6 the $LL(E_{EDGE})$ computed with the complete starting basis set is compared with those computed for models which only include the HOMO localised on each monomer. The two results are well correlated, and, in the majority of cases, one can attribute the difference in localisation length only to features of the HOMO orbitals. The few exceptions, discussed in Appendix S5 are easy to explain and can be anticipated from the shape of the HOMO containing very diffuse orbitals (for Se containing monomers in polymers 18 and 22) or negligible coupling between neighbouring HOMO orbitals due to the presence of nodal planes (polymer 7). Also noted in Figure 4.6 is the point for polymer 32, where the apparent low deviation between the results obtained using the complete and HOMO only basis set result from sigma-symmetry in the oPy HOMO, outlined in Appendix S5, which results in low $LL(E_{EDGE})$ regardless of the basis set. Finally, the two data points where $LL(E_{EDGE})$ increases the most with including all orbitals (polymers 4 and 22) are also the two outliers in Figure 4.4; that is, multi-orbital effects explain the lack of perfect correlation between and DOS tail.

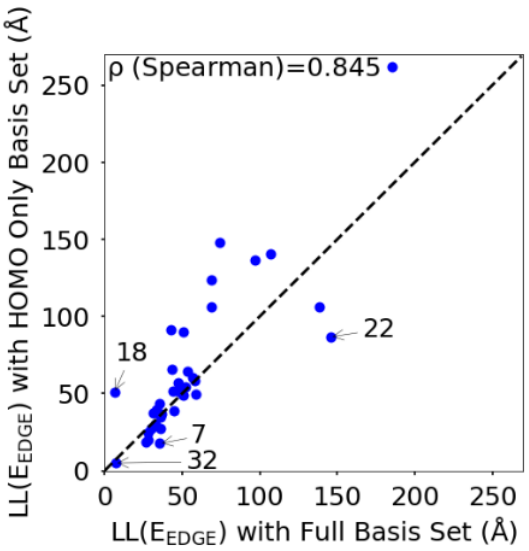

Figure 4.6: Correlation between localisation length obtained with complete starting basis set and reduced HOMO only basis set.

4.5 Polymer structural features and localisation length

The first polymer structural feature discussed is the number of chemically unique monomers in the polymer structural repeating unit. While these are not included in the polymer sample in Figure 4.1 to begin with, polymers with only one monomer in the structural repeating unit (homopolymers), such as polythiophene, were already found in previous work described in Chapter 3[111] to show worse DOS and localisation features than donor-acceptor copolymers which have 2 or more different monomers. The correlation in Figure 4.7 clearly shows that having only 2 unique monomers in the structural repeating unit is optimal, as it increases the likelihood of large localisation length, although the range of localisation lengths seen in polymers with 2 repeating units is very large. In the subsequent section 4.6 it is shown that the geometric average of all coupling fluctuations between all adjacent monomers correlates negatively with the decrease of the localisation length. Polymers containing only 2 monomers in the repeating unit are expected to display the largest distribution of localisation lengths (because there is only one element in the average) and, consequently, the maximum likelihood of particularly large localisation length.

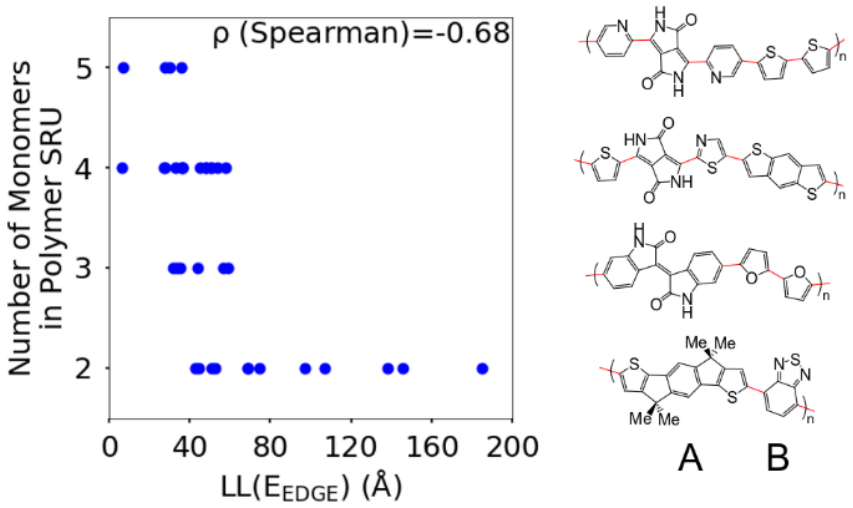

Figure 4.7: Correlation between the localisation length at band edge and number of monomers in polymer structural repeating unit. The right panel shows an example of SRUs with to 2, 3, 4, and 5 monomers, where distinct monomers are separated by red bonds in the drawn structures. The polymers with 2 monomers in the SRU are referred to as A-B polymers.

Another feature which is noticeably varied amongst reported polymers taken for the sample studied in Figure 4.1 is the size of the monomers in the polymer chain. The combined size of the monomers for each polymer SRU is measured with the polymer SRU length, shown in Figure 4.8, which is defined as the sum of distances between the connection sites on each monomer and bonds between the sites connecting each monomer in the structural repeating unit. Overall, there is no clear correlation between the polymer structural repeating unit length and the localisation length shown in Figure 4.8.

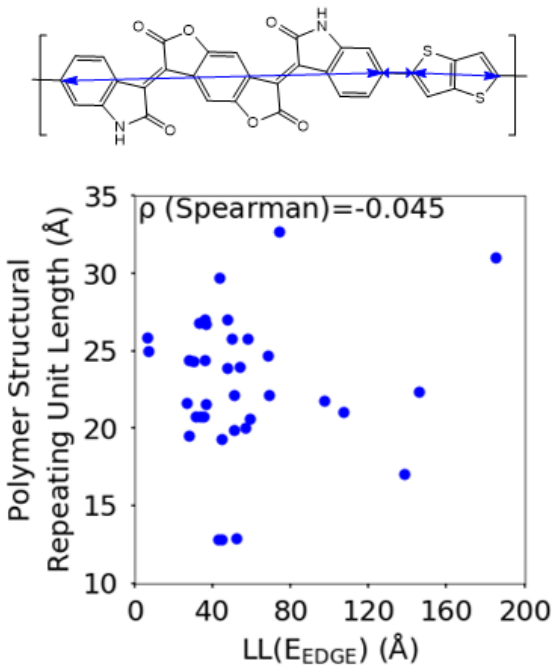

Figure 4.8: Correlation between the localisation length at band edge and polymer structural repeating unit length (bottom) defined as the sum of the length of each monomer.

The difference between the HOMO energy levels of adjacent monomers in the polymer chain, noted in section 4.4, appears to be another feature influencing the localisation length. To accommodate analysis of both A-B and non A-B type polymers, the correlation is computed for the localisation length with the average tunnelling barrier for the hole, defined as the difference between the highest energy HOMO along the polymer SRU and the mean average of all the other HOMO energies on the monomers in the SRU, shown in Figure 4.9. The Spearman ρ correlation for the average tunnelling barrier and localisation length was computed to be between -0.099 and 0.836 at the 95% confidence level. The negative lower limit suggests only a moderate correlation, although the observation made in reference[83] where an increase of the orbital gap between A-B polymers is shown to increase the localisation length supports the correlation of the latter with the average tunnelling barrier.[79] There is no statistically significant correlation between localisation length and tunnelling barrier when there are more than 2 monomers in the SRU, likely because of the many additional parameters that influence this case.

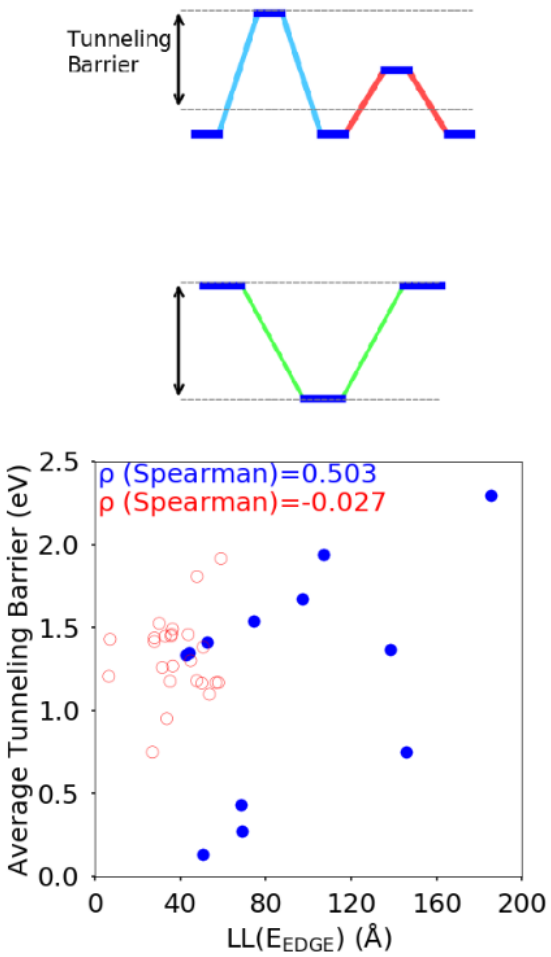

Figure 4.9: TOP: Definition of (average) hole tunnelling barrier. BOTTOM: Correlation of the localisation length with the average tunnelling barrier, which corresponds to the average energy needed for a hole charge carrier to hop between HOMOs on adjacent monomers in the polymer. The red points are non A-B polymers and the blue points are A-B polymers.

4.6 Coupling features and localisation length

In this section, the relation between the strength and fluctuation of the electronic coupling between monomers and the localisation length is explored. In all polymers containing a monomer with higher energy HOMO the highest energy orbitals tend to be linear combination of HOMOs localised on such monomers.[79] The polymer orbitals deriving from monomers with the highest energy HOMOs form a band with bandwidth which becomes larger if the effective coupling between high energy HOMO is larger. The energy difference between the polymer highest occupied band edge E_{EDGE} and the

energy of the highest onsite energy HOMO of a monomer, max(E(HOMO)) (Figure 4.10, top) is a global measure of the electronic coupling between highest energy HOMOs or the bandwidth for hole transport. In the bottom of Figure 4.10 it is shown that $|E_{EDGE}$-max(E(HOMO))| is negatively correlated with the localisation length (ρ in the range between -0.704 and -0.191 with 95% confidence level); that is, larger bandwidths or stronger couplings are detrimental for transport. This is in line with the expectations outlined in reference[85] where narrow bands are shown to facilitate transport and is fully in line with the evolution of the research field from the widest band of MEH-PPV[112] in the early days of organic electronics to the narrowest band of highest mobility polymers such as those containing the DPP monomer.[113]

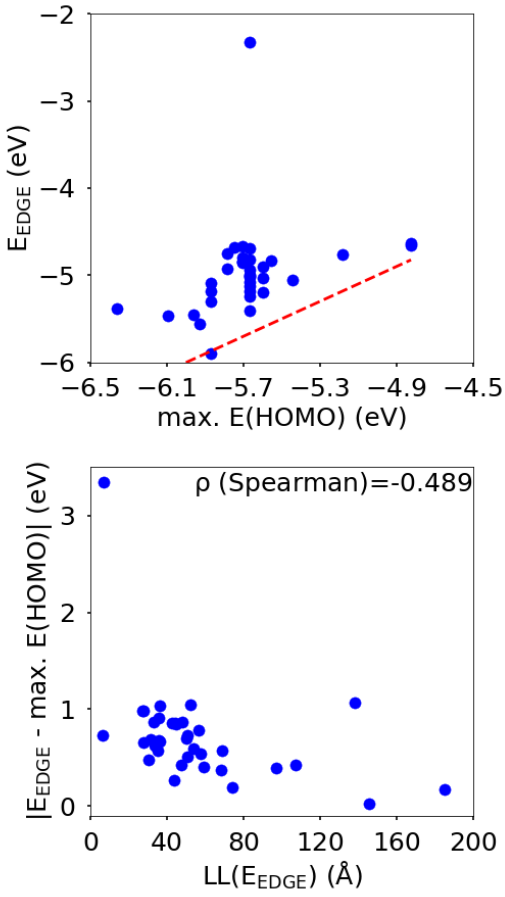

Figure 4.10: TOP: Plot of band edge energy E_{EDGE} vs the highest HOMO onsite energy in the structural repeating unit max(E(HOMO) of the polymers in the sample shown in Figure 4.1, where the red hashed line is for the case of no coupling between monomer MOs in the polymer chains. BOTTOM: Correlation between the localisation length at band edge and $|E_{EDGE}$-max(E(HOMO))|.

The other aspect of coupling to be examined is the fluctuation in coupling magnitude, which describes the extent of electronic disorder in the polymer chains. The effective coupling between two localised orbitals coupled through a one-dimensional chain of localised orbitals has been studied extensively in the context of electron transfer theory[114] and single molecule electronics.[115] According to perturbative theories[116] and more advanced techniques[117] the effective coupling is proportional to the product of the coupling along the chain $J_{i,i+1}$. For small normal fluctuations, the relative fluctuation of the overall coupling is given by $\left[\sum\left(\sigma_{i,i+1}^{rel}\right)^2\right]^{0.5}$ (as encountered in standard error propagation analysis), with the summation extending to all adjacent pairs in the SRU, and this simplified and intuitive measure is used here to rationalize the results. Figure 4.11 shows that lower combined coupling fluctuation $\left[\sum\left(\sigma_{i,i+1}^{rel}\right)^2\right]^{0.5}$ is correlated with higher localisation length thus it is observed that lower electronic disorder along polymer chains is preferred. Such a correlation (ρ in the range -0.807 and -0.411 with 95% confidence level) also explains a key feature of Figure 4.9, where the localisation length is more narrowly distributed for polymers with more monomers in the SRU because more terms are involved in the summation.

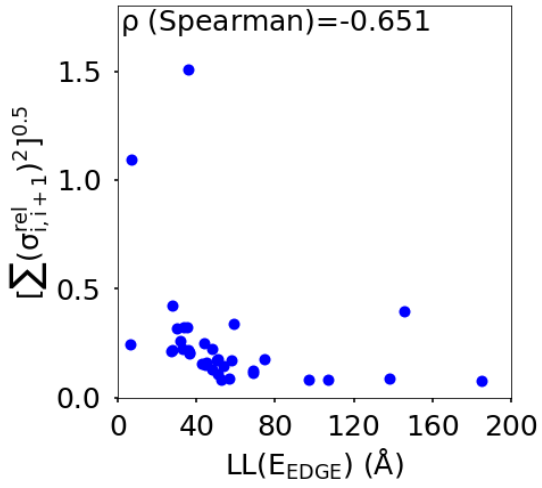

Figure 4.11: Correlation between the localisation length at band edge and combined coupling fluctuation $\left[\sum\left(\sigma_{i,i+1}^{rel}\right)^2\right]^{0.5}$.

From the correlations in Figure 4.10 and Figure 4.11 it is apparent that low coupling fluctuation and magnitude are desirable for higher localisation length, which is in line with previously reported examples of work suggesting the importance of minimising electronic disorder to achieve higher charge carrier mobility.[20, 93] The results, however, provide more than just broad agreement with certain phenomenological models because the data can be used to establish the degree of confidence in following certain design rules such as focusing on 2 monomers per SRU and maximizing the gap between HOMO orbitals in different monomers. However, no explicitly ranking for the importance of each design rule is given here as this is not just dependent on the robustness of the correlation shown with $LL(E_{EDGE})$ but also related to the facility of implementation in designing new polymers. For example, the design rule of A-B polymer sequences is easily implemented and many of the approximations of the model used in the work here will not affect this conclusion, whereas reducing coupling fluctuation requires calculation and its impact is modulated by possible effects of intermolecular interactions.

4.7 Torsional potential features and electronic disorder

While the number of monomers and the energy mismatch between their HOMO levels can be easily engineered it is not clear from the data presented so far how one can decrease the coupling fluctuation. Two ideas have been put forward in the literature. The first one is that the coupling fluctuation is reduced if the torsional potential favours a mutual geometry of the monomers in which they lie in the same plane as rigidly as possible.[65] In agreement with this view, a strong correlation is observed, shown in the top of Figure 4.12, between $LL(E_{EDGE})$ and the torsional entropy $S_\phi = -R\sum_i p_i ln(p_i)$, which measures the dihedral angles accessible at a given temperature and is related to the Boltzmann probability p_i of occupying a certain dihedral angle, at 298.15 K.[118] There is one noticeable outlier point in the plot of S_ϕ and $\sigma_{i,i+1}^{rel}$ caused by the dimer DPP-oPy[A]

which is discussed in Appendix S6. In general, S_ϕ is minimal in the presence of a deep potential energy well in the torsional potential.

A distinct proposal for reducing the coupling fluctuation is to consider monomer pairs for which the HOMO-HOMO coupling is less sensitive to the dihedral angle. It was indeed noticed that in some instances the relative coupling profile $J_{i,i+1}^{rel}(\phi) = J_{i,i+1}(\phi)/J_{i,i+1}(\phi = 180^0)$ is flatter around ϕ=0 or 180°, where the first derivative is null by symmetry.[74] Thus, $J_{i,i+1}^{rel}(\phi)$ is characterized with the curvature, defined as the second derivative $d^2J_{i,i+1}^{rel}(\phi)/d\phi^2$ calculated at the global minimum in the torsional potential of the dimers. While there are some examples of dimers showing varying curvature in $J_{i,i+1}^{rel}(\phi)$, shown in the bottom of Figure 4.12, overall there is not a strong correlation between $d^2J_{i,i+1}^{rel}(\phi)/d\phi^2$ and $\sigma_{i,i+1}^{\mathrm{rel}}$ indicating that optimising the curvature is not a viable approach considering the pool of monomer pairs in the dataset.

Lastly, the molecular structures of select low and high $\sigma_{i,i+1}^{\mathrm{rel}}$ dimers were briefly examined, where the structures of the dimers with the 10 lowest and highest $\sigma_{i,i+1}^{\mathrm{rel}}$, respectively, excluding dimers containing the monomer oPy, are shown in Figures S7.1 and S7.2 in Appendix S7. There are some common features amongst those lower $\sigma_{i,i+1}^{\mathrm{rel}}$ dimers; contiguous fused ring motifs, heteroatoms which can form non-covalent interactions, and monomer dipoles. Of these features, only the presence of contiguous fused ring motifs is mostly absent amongst the higher $\sigma_{i,i+1}^{\mathrm{rel}}$ dimers, with several dimers having only small thiophene sized monomers. However, these features observed are not conclusive, and this is left to future work beyond the scope of this chapter.

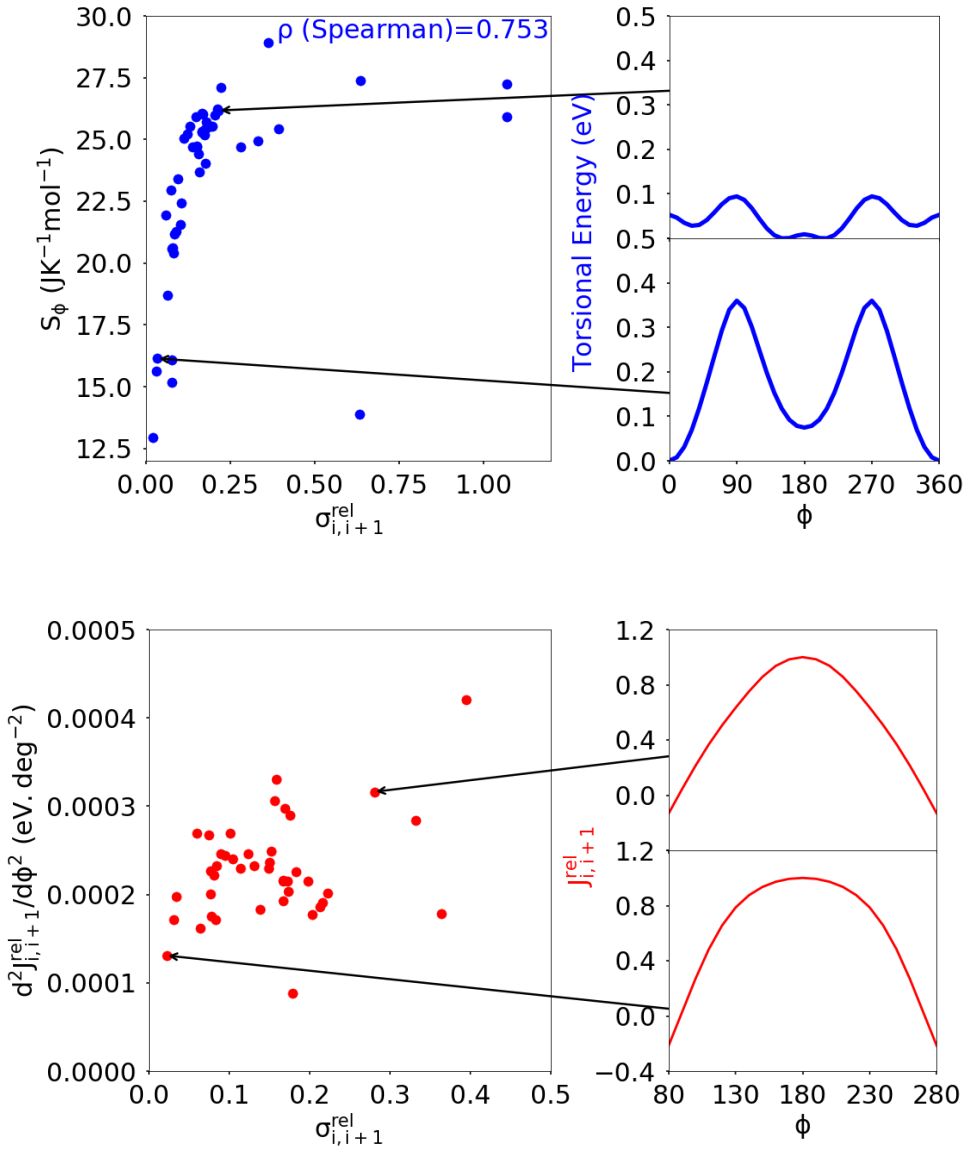

Figure 4.12: Correlation of the relative coupling fluctuation $\sigma^{\mathrm{rel}}_{i,i+1}$, the main measure for electronic disorder, with each the torsional entropy of the dimers (blue) and curvature in the relative coupling profile $d^2J^{rel}_{i,i+1}(\phi)/d\phi^2$ measured at the global minima in the torsional potential for each dimer (red). In the S_ϕ vs $\sigma^{\mathrm{rel}}_{i,i+1}$ plot, the point for polymer 32 is not shown as it lies significantly above the range covered by points from the other polymers of the polymer sample studied. The plot for $d^2J^{rel}_{i,i+1}(\phi)/d\phi^2$ vs $\sigma^{\mathrm{rel}}_{i,i+1}$ excludes points which deviate significantly from the cluster of points shown, the full plot is included in Appendix S6.

4.8 Further rationalization of results through a simplified model Hamiltonian

To further verify the explanation of the design rules discussed so far, calculations were done using a model Hamiltonian to explore more systematically the effect of the different parameters. The model includes only one orbital per site, and 2, 3, or 4 repeating units. The overlap matrix is assumed to be the identity matrix. The continuous parameters of the model are set as follows:

- The energy of the orbital in the first repeating unit is set to parameter ΔE controlling the relative orbital energies, while the other repeating units have orbital energy set to zero. ΔE is sampled between 0.1 and 2.3 eV, corresponding to the range of the average tunnelling barrier observed for the polymers studied here, and set to the median of the range ΔE=1.2 eV when the other parameters are changed.

- The coupling characteristics are controlled by parameter J_0 which determines the amplitude of the cosine defining the dependence of the coupling J between adjacent monomers on the relative dihedral angle ϕ where J=0.5 J_0 cos(ϕ). J_0 is sampled in the range between 0.05 and 3.55 eV, corresponding to the range of amplitudes typically observed in the coupling profiles of the dimers, and is set to the median of the range J_0=1.8 eV when the other parameters are changed.

- The torsional potential is controlled by parameter V_0 determining the depth of the minima and assumed to be of the form $V=V_0 \sin^2(\phi)$. V_0 is sampled in the range between 0.05 and 0.36 eV, corresponding to the range of minima depths observed in the torsional potentials of the dimers, and is set to the median of the range V_0=0.20 eV when the other parameters are changed.

The temperature is fixed at 298.15 K. The relative coupling fluctuation $\sigma_{i,i+1}^{rel}$ is controlled by the parameter V_0; as shown in panel a) of Figure 4.13. To compute the localisation length $LL(E_{EDGE})$, the polymer chain is considered as being a rigid rod with the distance between adjacent monomers

being the unit length. The results in panels b)-d) of Figure 4.13 are averages over 100 chains of 1200 monomer-long chains.

The main observations of the first part of the manuscript are reproduced by the results shown in panel b) of Figure 4.13. The localisation length increases by increasing the rigidity of the chain (i.e. larger V_0 and therefore smaller $\sigma_{i,i+1}^{rel}$) and the increase in the number of monomers in structural repeating unit causes a decrease in localisation length. The increase of the orbital gap ΔE shown in panel c) of Figure 4.13 (in effect analogous to the *decrease* of the coupling J_0 shown in panel d) of Figure 4.13) cause a moderate increase of localisation length for polymers with 2 repeat units and a decrease of localisation length with polymers with more than 2 monomers in the structural repeat unit. The effect seen for polymers with 2 monomers in the repeat unit was observed with a more realistic Hamiltonian in Figure 4.9, while no correlation was observed for larger numbers of monomers in the repeat units probably because of the much greater number of parameters affecting the results of realistic systems in comparison with the idealised model. It is worth noticing in passing, that over the past 40 years the top performing polymers of each decade (PPV, P3HT, PBTTT, DPP-based)[119] display a decreasing bandwidth; that is, as a long as the transport remains delocalised, electronic coupling along the chain seems not to be the primary factor determining the charge mobility.

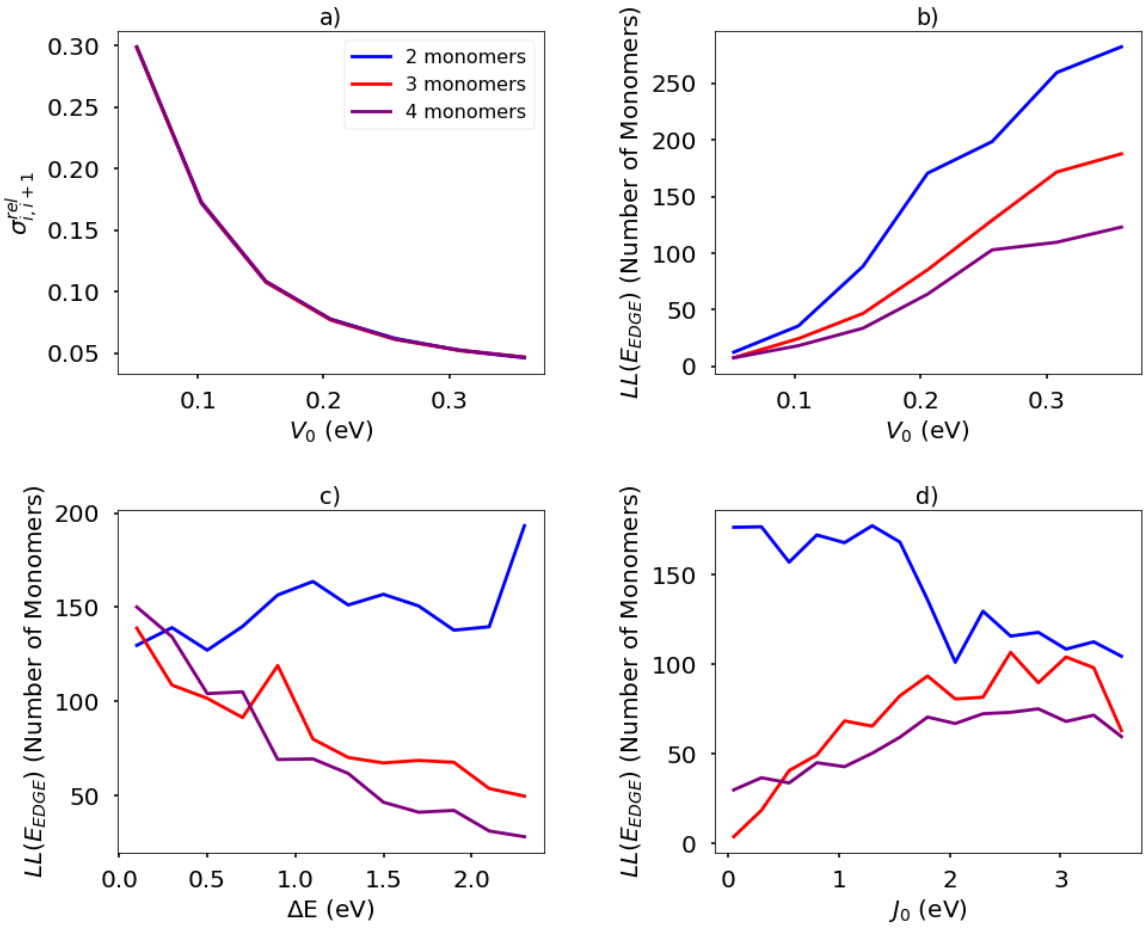

Figure 4.13: (a) Relation between relative fluctuation of the coupling and rigidity of the torsional potential in a simplified model Hamiltonian. For the same model, average localisation length at the band edge for different number of monomers in the structural repeat unit as a function of (b) torsional barrier V_0 (c) orbital energy gap ΔE (c) inter-monomer coupling J_0.

4.9 Conclusion

In the screening study described in this chapter, the electronic structure and charge delocalisation characteristics of a large number of polymer models were analysed and the features that most effectively produce greater charge delocalisation and reduced electronic disorder were identified. Given the sample of polymers considered, structure-property relations were observed that can be trusted with an associated degree of statistical significance. Two features are jointly the most important in determining greater localisation length: (i) a reduced relative fluctuation of the coupling between localised HOMO orbitals on adjacent monomers $\sigma^{\mathrm{rel}}_{i,i+1}$ and (ii) the presence of only two

monomers in the SRU, i.e. a preference for AB type polymer sequences. Less important but also contributing to greater localisation length are (iii) a greater difference in the energy of the HOMO orbitals for polymers with SRUs containing only two monomers (AB type polymers) and (iv) an overall smaller coupling between HOMO orbitals localised on adjacent monomers.

The results of the work in this chapter are in line with previous works in that they considers the electronic disorder as the most significant factor; this appears to be the aim of strategies employed by others such as incorporating more planarized and fused ring monomers,[7, 120, 121] and engineering non-covalent locks in chains to planarize polymer chain backbones and thus minimise backbone torsional disorder.[121] However, several polymers reported have a significant number with non AB type sequences, thus the results which suggest a preference for AB type polymer sequence, is not only supported previous theoretical work but observes this preference over a large sample of polymers thus providing an important contribution in verifying the potential of an AB type only approach to sequence design.[77] Additionally, the finding that the disorder in the coupling is more significant than its magnitude is contrary to other views on this matter.[122] Finally, the opportunity provided by increasing the energy mismatch between the HOMO orbitals in AB type polymers was never directly exploited in materials design.

Most of the derived structure-property relations can be immediately used for the development of new polymers as they concern the monomer sequence (part of synthetic design) and the energy levels of the monomer MOs (normally known). Identifying monomer pairs with reduced fluctuation of the electronic coupling still defies simple intuitive rules but the relevant electronic structure calculations are straightforward and can be employed to explore new chemistries at marginal costs.

Chapter 5
Conclusion and Outlook

5.1 Conclusion

The work in this thesis overall presents a convenient approach to discovering structure property relationships for charge carrier mobility in semiconducting conjugated polymers relevant in flexible electronics applications, which are typically disordered materials. In Chapters 1-2, the existing models used to conceptualise charge carrier transport in disordered polymer materials were discussed, and current understanding of how the disordered morphology affects the features of charge carrier transport in conjugated polymers was outlined. An important concept highlighted in Chapter 2 was the density of states, which could be used to characterise the electronic structure and thus infer charge transport characteristics of a polymer. Chapter 1 further elaborates on the strategies that have been employed in other work to improve charge carrier mobilities in conjugated polymer materials, outlining the prevailing views on the structure property relation for mobility in these disordered polymers. This survey of understanding in the structure property relation for mobility shows that a general consensus on clear definite principles for designing high mobility polymers is lacking, with proposed principles coming from work done with specific polymer examples, thus motivating the work in this thesis to develop general structure-property relations for semiconducting polymers.

The first problem to solve in exploring large numbers of polymer structures is the electronic structure calculations, for which a rapid method of calculating the electronic structure of polymer chains was developed in the work described in Chapter 3. Rapid calculation is achieved by using the localised molecular orbital method to generate the matrix inputs, employing a tight binding approximation to simplify the generation of the polymer chain Hamiltonian matrix. The elements obtained from matrices calculated for fragments of the polymer chain are used to populate the

Hamiltonian for the whole chain in a modular fashion, with inclusion of only the π-MOs on the monomers in the basis set. The fragment matrices used for populating the off-diagonal elements of the polymer chain Hamiltonian are generated with sampling of the torsional potential range for the dimers that occur in the chain, thus preserving atomistic detail. An additional calibration procedure introduced post initial calculation was demonstrated to improve the energies thus obtained and the accuracy of results at minimal cost compared to a full quantum calculation. The results obtained from the rapid calculation method were validated against those from full quantum calculations showing that essential features of the density of states and orbital localisation characteristics expected in those calculated with energies from a full calculation are reproduced with the approximated method. The implementation of the method allows for reuse of the input fragment matrices in calculations done at the same level of theory and for chains containing the same fragments, thus being very ideal for screening applications.

The methodology developed in Chapter 3 was demonstrated for a sample of 5 p-type polymers encompassing both DA copolymers and homopolymers. The bulk polymer material was simulated in a rapid fashion by using large ensembles of single polymer chains, an approach justified in Chapter 2, and sampling the chain conformations using Boltzmann statistics. The density of states and orbital localisation were calculated to characterise the electronic structure of the polymers sampled, and the key features of these could be rationalized by examining the relative energy levels of the HOMOs localised on each monomer in the polymer repeat unit and the fluctuation in the coupling of HOMOs localised on adjacent monomers. Most importantly, it was found that greater mobility was correlated with localisation length and tail slope at the DOS band edge, and a correspondence in the order of localisation length computed using the rapid calculation method with the reported experimental mobilities for 3 of the 5 polymers was observed. These results demonstrated the potential of the methodology to be used for screening large samples of polymer structures using the localisation length and tail slope at the DOS band edge as proxy figures of merit for mobility which are comparable across all polymers.

Using the methodology developed in Chapter 3 a screening study encompassing a large sample of 36 polymers was described in Chapter 4. The screening demonstrates the ability of the rapid calculation method developed to be applied for studying large numbers of polymers. With regards to the screening methodology, the localisation length and tail slope at the band edge of the DOS, previously identified as suitable proxy properties for the charge carrier mobility, were observed to be largely interchangeable, and the former measure was used to identify structure property relations for mobility by examining the correlation with measures derived from electronic and structural properties of the polymers studied. The most important factor identified in obtaining a higher localisation length was the electronic disorder exhibited by the polymer; specifically, a reduction in the fluctuation of the coupling between HOMO orbitals localised on adjacent monomers along the chain correlates with higher localisation length. This is better achieved with polymers containing only 2 distinct monomers in their SRU, so called AB type polymers. Other features of the polymers identified to be relevant for achieving higher localisation length were the difference in HOMO orbital energies localised on adjacent monomers for AB type polymers and smaller magnitude coupling between the HOMO orbitals. The results present a set of design principles which map a figure of merit, the localisation length, to tuneable features of the polymer that correspond to parameters in the molecular structure, such as the polymer sequence and HOMO orbital energies. The validity and applicability of these principles can be further investigated in future work.

5.2 Outlook

The findings presented in Chapters 3 and 4 provide several bases for future work. The methodology for rapid electronic structure calculation in Chapter 3 is largely self-contained as it provides a scheme for generating realistic chain conformations and can be used to explore further screening of hypothetical conjugated polymer repeat units under the assumption that interchain interactions in

the bulk material are less significant than intrachain transport, which allows the electronic structure of the simulated bulk material to be calculated using those of the constituent single polymer chains. Alternatively, the electronic calculation method can be used with chain conformations generated with interchain effects accounted for, such as those from molecular dynamics simulations and the effects of ignoring such interactions can be examined for already known polymers, testing the validity of the single chain-based approach to simulating the bulk polymer material used in Chapter 3. A notable finding from Chapter 4 to explore further is that the electronic coupling along the chain appears to have a weak effect on the localisation length and a preference for smaller coupling between HOMO orbitals on adjacent monomers is observed. Sequences could be explored containing monomers with weaker HOMO coupling, or even connectivity between monomers that diminishes coupling between HOMO orbitals significantly, such as disrupting conjugation with alkyl group spacers.[123] The screening in Chapter 4 shows that structure property relationships for the amorphous polymers studied can be deduced from analysis of only essential chain features, such as HOMO energy levels and torsional potential of adjacent monomer pairs, thus polymers with novel sequences could be explored similarly using models of their chains reduced to such features. The reduced model chain can include only the HOMOs on each monomer along the chains, and the inter-monomer torsional potentials to determine the chain conformations and HOMO-HOMO coupling, providing a set of features which can be described with a functional dependence on the intermonomer dihedral angles containing a defined set of parameters that can be varied individually. Such a reduced model can be used to screen polymers by varying the parameters affecting the torsional potential and computing the mobility using a model Hamiltonian, where the coupling obtained from the functional dependence can be used as inputs for the latter.

References

1. Y. Lu, J.-Y. Wang and J. Pei, *Chem. Mater.*, 2019, **31**, 6412-6423.
2. N. Banerji, S. Cowan, E. Vauthey and A. J. Heeger, *The Journal of Physical Chemistry C*, 2011, **115**, 9726-9739.
3. D. M. de Leeuw, M. M. J. Simenon, A. R. Brown and R. E. F. Einerhand, *Synth. Met.*, 1997, **87**, 53-59.
4. M. Wang, P. Baek, A. Akbarinejad, D. Barker and J. Travas-Sejdic, *Journal of Materials Chemistry C*, 2019, **7**, 5534-5552.
5. D. Wu, M. Kaplan, H. W. Ro, S. Engmann, D. A. Fischer, D. M. DeLongchamp, L. J. Richter, E. Gann, L. Thomsen, C. R. McNeill and X. Zhang, *Chem. Mater.*, 2018, **30**, 1924-1936.
6. G. W. Kim, E. H. Kwon, M. Kim and Y. D. Park, *The Journal of Physical Chemistry C*, 2019, **123**, 23255-23263.
7. A. F. Paterson, S. Singh, K. J. Fallon, T. Hodsden, Y. Han, B. C. Schroeder, H. Bronstein, M. Heeney, I. McCulloch and T. D. Anthopoulos, *Adv. Mater.*, 2018, **30**, 1801079.
8. M. Kim, S. U. Ryu, S. A. Park, K. Choi, T. Kim, D. Chung and T. Park, *Adv. Funct. Mater.*, 2020, **30**, 1904545.
9. A. R. Moore, *Appl. Phys. Lett.*, 1977, **31**, 762-764.
10. M. I. Nathan, W. P. Dumke, K. Wrenner, S. Tiwari, S. L. Wright and K. A. Jenkins, *Appl. Phys. Lett.*, 1988, **52**, 654-656.
11. K. Kang, S. Xie, L. Huang, Y. Han, P. Y. Huang, K. F. Mak, C.-J. Kim, D. Muller and J. Park, *Nature*, 2015, **520**, 656-660.
12. L. Janasz, D. Chlebosz, M. Gradzka, W. Zajaczkowski, T. Marszalek, K. Müllen, J. Ulanski, A. Kiersnowski and W. Pisula, *Journal of Materials Chemistry C*, 2016, **4**, 11488-11498.
13. I. McCulloch, M. Heeney, C. Bailey, K. Genevicius, I. MacDonald, M. Shkunov, D. Sparrowe, S. Tierney, R. Wagner, W. Zhang, M. L. Chabinyc, R. J. Kline, M. D. McGehee and M. F. Toney, *Nat. Mater.*, 2006, **5**, 328-333.
14. B. H. Hamadani, D. J. Gundlach, I. McCulloch and M. Heeney, *Appl. Phys. Lett.*, 2007, **91**, 243512.
15. E. Cho, C. Risko, D. Kim, R. Gysel, N. Cates, D. W. Breiby, M. D. McGehee, M. F. Toney, R. J. Kline and J.-L. Bredas, *Journal of the American Chemical Society*, 2012, **134**, 6177-6190.
16. Z. Wu, A. Petzold, T. Henze, T. Thurn-Albrecht, R. H. Lohwasser, M. Sommer and M. Thelakkat, *Macromolecules*, 2010, **43**, 4646-4653.
17. Y. Ie, K. Morikawa, W. Zajaczkowski, W. Pisula, N. B. Kotadiya, G.-J. A. H. Wetzelaer, P. W. M. Blom and Y. Aso, *Advanced Energy Materials*, 2018, **8**, 1702506.
18. X. Zhang, H. Bronstein, A. J. Kronemeijer, J. Smith, Y. Kim, R. J. Kline, L. J. Richter, T. D. Anthopoulos, H. Sirringhaus, K. Song, M. Heeney, W. Zhang, I. McCulloch and D. M. DeLongchamp, *Nature Communications*, 2013, **4**, 2238.
19. P.-T. Wu, F. S. Kim and S. A. Jenekhe, *Chem. Mater.*, 2011, **23**, 4618-4624.
20. D. Venkateshvaran, M. Nikolka, A. Sadhanala, V. Lemaur, M. Zelazny, M. Kepa, M. Hurhangee, A. J. Kronemeijer, V. Pecunia, I. Nasrallah, I. Romanov, K. Broch, I. McCulloch, D. Emin, Y. Olivier, J. Cornil, D. Beljonne and H. Sirringhaus, *Nature*, 2014, **515**, 384-388.
21. I. Kang, H.-J. Yun, D. S. Chung, S.-K. Kwon and Y.-H. Kim, *Journal of the American Chemical Society*, 2013, **135**, 14896-14899.
22. S. Y. Son, Y. Kim, J. Lee, G.-Y. Lee, W.-T. Park, Y.-Y. Noh, C. E. Park and T. Park, *Journal of the American Chemical Society*, 2016, **138**, 8096-8103.
23. J. Li, Y. Zhao, H. S. Tan, Y. Guo, C.-A. Di, G. Yu, Y. Liu, M. Lin, S. H. Lim, Y. Zhou, H. Su and B. S. Ong, *Scientific Reports*, 2012, **2**, 754.
24. G. J. Hedley, A. Ruseckas and I. D. W. Samuel, *Chem. Rev.*, 2017, **117**, 796-837.

25. P. K. Bhatnagar, in *Nanomaterials and Their Applications*, ed. Z. H. Khan, Springer Singapore, Singapore, 2018, DOI: 10.1007/978-981-10-6214-8_10, pp. 261-287.
26. R. Kubota, Y. Sasaki, T. Minamiki and T. Minami, *ACS Sensors*, 2019, **4**, 2571-2587.
27. H.-W. Chen, J.-H. Lee, B.-Y. Lin, S. Chen and S.-T. Wu, *Light: Science &Amp; Applications*, 2018, **7**, 17168.
28. C.-a. Di, G. Yu, Y. Liu and D. Zhu, *The Journal of Physical Chemistry B*, 2007, **111**, 14083-14096.
29. M. Pandey, N. Kumari, S. Nagamatsu and S. S. Pandey, *Journal of Materials Chemistry C*, 2019, **7**, 13323-13351.
30. A. R. Murphy and J. M. J. Fréchet, *Chem. Rev.*, 2007, **107**, 1066-1096.
31. J. T. E. Quinn, J. Zhu, X. Li, J. Wang and Y. Li, *Journal of Materials Chemistry C*, 2017, **5**, 8654-8681.
32. R. Ganesamoorthy, G. Sathiyan and P. Sakthivel, *Solar Energy Materials and Solar Cells*, 2017, **161**, 102-148.
33. S. Li, L. Ye, W. Zhao, S. Zhang, S. Mukherjee, H. Ade and J. Hou, *Adv. Mater.*, 2016, **28**, 9423-9429.
34. C. W. Schlenker, V. S. Barlier, S. W. Chin, M. T. Whited, R. E. McAnally, S. R. Forrest and M. E. Thompson, *Chem. Mater.*, 2011, **23**, 4132-4140.
35. L. Lu, T. Zheng, Q. Wu, A. M. Schneider, D. Zhao and L. Yu, *Chem. Rev.*, 2015, **115**, 12666-12731.
36. X. Kang, D. Zhou, Q. Wang, D. Zhu, X. Bao, X. Yuan, F. Liu, Y. Li, S. Qiao and R. Yang, *ACS Appl. Mater. Interfaces*, 2019, **11**, 48155-48161.
37. S. P. Singh, C. H. P. Kumar, P. Nagarjuna, G. D. Sharma, S. Biswas and J. A. Mikroyannidis, *The Journal of Physical Chemistry C*, 2013, **117**, 13350-13356.
38. B. Qi and J. Wang, *J. Mater. Chem.*, 2012, **22**, 24315-24325.
39. G. Dennler, M. C. Scharber and C. J. Brabec, *Adv. Mater.*, 2009, **21**, 1323-1338.
40. C. J. Brabec, S. E. Shaheen, C. Winder, N. S. Sariciftci and P. Denk, *Appl. Phys. Lett.*, 2002, **80**, 1288-1290.
41. Z. G. Zhang and J. Wang, *J. Mater. Chem.*, 2012, **22**, 4178-4187.
42. Z. Xiao, T. Duan, H. Chen, K. Sun and S. Lu, *Solar Energy Materials and Solar Cells*, 2018, **182**, 1-13.
43. E. Lanzarini, M. R. Antognazza, M. Biso, A. Ansaldo, L. Laudato, P. Bruno, P. Metrangolo, G. Resnati, D. Ricci and G. Lanzani, *The Journal of Physical Chemistry C*, 2012, **116**, 10944-10949.
44. D. J. Woods, R. S. Sprick, C. L. Smith, A. J. Cowan and A. I. Cooper, *Advanced Energy Materials*, 2017, **7**, 1700479.
45. R. S. Sprick, J.-X. Jiang, B. Bonillo, S. Ren, T. Ratvijitvech, P. Guiglion, M. A. Zwijnenburg, D. J. Adams and A. I. Cooper, *Journal of the American Chemical Society*, 2015, **137**, 3265-3270.
46. M. Kuik, G.-J. A. H. Wetzelaer, H. T. Nicolai, N. I. Craciun, D. M. De Leeuw and P. W. M. Blom, *Adv. Mater.*, 2014, **26**, 512-531.
47. D. Fazzi and M. Caironi, *Physical Chemistry Chemical Physics*, 2015, **17**, 8573-8590.
48. M. Mladenović and N. Vukmirović, *The Journal of Physical Chemistry C*, 2015, **119**, 23329-23333.
49. X. Shi, V. Nádaždy, A. Perevedentsev, J. M. Frost, X. Wang, E. von Hauff, R. C. I. MacKenzie and J. Nelson, *Physical Review X*, 2019, **9**, 021038.
50. S. A. Mollinger, B. A. Krajina, R. Noriega, A. Salleo and A. J. Spakowitz, *ACS Macro Letters*, 2015, **4**, 708-712.
51. E. D. Miller, M. L. Jones and E. Jankowski, *Journal*, 2018, **10**.
52. N. E. Jackson, K. L. Kohlstedt, B. M. Savoie, M. Olvera de la Cruz, G. C. Schatz, L. X. Chen and M. A. Ratner, *Journal of the American Chemical Society*, 2015, **137**, 6254-6262.

53. L. Berencei, A. Grout-Smith, J. E. Poole and W. Barford, *The Journal of Chemical Physics*, 2019, **151**, 064120.
54. C. Poelking, E. Cho, A. Malafeev, V. Ivanov, K. Kremer, C. Risko, J.-L. Brédas and D. Andrienko, *The Journal of Physical Chemistry C*, 2013, **117**, 1633-1640.
55. P. Gemünden, C. Poelking, K. Kremer, K. Daoulas and D. Andrienko, *Macromol. Rapid Commun.*, 2015, **36**, 1047-1053.
56. R. Noriega, J. Rivnay, K. Vandewal, F. P. V. Koch, N. Stingelin, P. Smith, M. F. Toney and A. Salleo, *Nat. Mater.*, 2013, **12**, 1038.
57. Y. Imamura, M. Tashiro, M. Katouda and M. Hada, *The Journal of Physical Chemistry C*, 2017, **121**, 28275-28286.
58. I. Y. Kanal, S. G. Owens, J. S. Bechtel and G. R. Hutchison, *The Journal of Physical Chemistry Letters*, 2013, **4**, 1613-1623.
59. L. Wilbraham, E. Berardo, L. Turcani, K. E. Jelfs and M. A. Zwijnenburg, *J. Chem. Inf. Model.*, 2018, **58**, 2450-2459.
60. H. T. Turan, O. Kucur, B. Kahraman, S. Salman and V. Aviyente, *Physical Chemistry Chemical Physics*, 2018, **20**, 3581-3591.
61. P. B. Jørgensen, M. Mesta, S. Shil, J. M. García Lastra, K. W. Jacobsen, K. S. Thygesen and M. N. Schmidt, *The Journal of Chemical Physics*, 2018, **148**, 241735.
62. S. Nagasawa, E. Al-Naamani and A. Saeki, *The Journal of Physical Chemistry Letters*, 2018, **9**, 2639-2646.
63. Q. Yuan, A. Santana-Bonilla, M. A. Zwijnenburg and K. E. Jelfs, *Nanoscale*, 2020, **12**, 6744-6758.
64. J. Huang, Z. Mao, Z. Chen, D. Gao, C. Wei, W. Zhang and G. Yu, *Chem. Mater.*, 2016, **28**, 2209-2218.
65. Z.-D. Yu, Y. Lu, J.-Y. Wang and J. Pei, *Chemistry – A European Journal*, 2020, **26**, 16194-16205.
66. N. E. Jackson, B. M. Savoie, K. L. Kohlstedt, M. Olvera de la Cruz, G. C. Schatz, L. X. Chen and M. A. Ratner, *Journal of the American Chemical Society*, 2013, **135**, 10475-10483.
67. C. Zhu and L. Fang, *Macromol. Rapid Commun.*, 2018, **39**, 1700241.
68. G. P. Kini, Y. W. Han, S. J. Jeon, Y. J. Lee and D. K. Moon, *Materials Chemistry Frontiers*, 2022, **6**, 1759-1769.
69. Q. Wang, S. Böckmann, F. Günther, M. Streiter, M. Zerson, A. D. Scaccabarozzi, W. L. Tan, H. Komber, C. Deibel, R. Magerle, S. Gemming, C. R. McNeill, M. Caironi, M. R. Hansen and M. Sommer, *Chem. Mater.*, 2021, **33**, 2635-2645.
70. B. Liu, D. Rocca, H. Yan and D. Pan, *JACS Au*, 2021, **1**, 2182-2187.
71. R. Dilmurat, V. Lemaur, Y. Olivier, S. M. Gali and D. Beljonne, *The Journal of Physical Chemistry C*, 2022, **126**, 3118-3126.
72. H. Chen, A. Wadsworth, C. Ma, A. Nanni, W. Zhang, M. Nikolka, A. M. T. Luci, L. M. A. Perdigão, K. J. Thorley, C. Cendra, B. Larson, G. Rumbles, T. D. Anthopoulos, A. Salleo, G. Costantini, H. Sirringhaus and I. McCulloch, *Journal of the American Chemical Society*, 2019, **141**, 18806-18813.
73. A. Troisi and A. Shaw, *The Journal of Physical Chemistry Letters*, 2016, **7**, 4689-4694.
74. R. P. Fornari and P. de Silva, *Chemistry – A European Journal*, 2019, **25**, 14651-14658.
75. M. Caironi, M. Bird, D. Fazzi, Z. Chen, R. Di Pietro, C. Newman, A. Facchetti and H. Sirringhaus, *Adv. Funct. Mater.*, 2011, **21**, 3371-3381.
76. D. Fazzi and F. Negri, *Advanced Electronic Materials*, 2021, **7**, 2000786.
77. J. C. Maier and N. E. Jackson, *Macromolecules*, 2021, **54**, 7060-7069.
78. R. Dilmurat, S. Prodhan, L. Wang and D. Beljonne, *The Journal of Chemical Physics*, 2022, **156**, 084115.
79. R. P. Fornari and A. Troisi, *Adv. Mater.*, 2014, **26**, 7627-7631.

80. H. Bässler and A. Köhler, in *Unimolecular and Supramolecular Electronics I: Chemistry and Physics Meet at Metal-Molecule Interfaces*, ed. R. M. Metzger, Springer Berlin Heidelberg, Berlin, Heidelberg, 2012, DOI: 10.1007/128_2011_218, pp. 1-65.
81. R. Di Pietro, I. Nasrallah, J. Carpenter, E. Gann, L. S. Kölln, L. Thomsen, D. Venkateshvaran, K. O'Hara, A. Sadhanala, M. Chabinyc, C. R. McNeill, A. Facchetti, H. Ade, H. Sirringhaus and D. Neher, *Adv. Funct. Mater.*, 2016, **26**, 8011-8022.
82. K. S. Radke, F. Ortmann and G. Cuniberti, in *Supramolecular Materials for Opto-Electronics*, ed. N. Koch, The Royal Society of Chemistry, 2014, DOI: 10.1039/9781782626947-00273, p. 0.
83. W. Barford, M. Marcus and O. R. Tozer, *The Journal of Physical Chemistry A*, 2016, **120**, 615-620.
84. P. W. Anderson, *Phys. Rev.*, 1958, **109**, 1492-1505.
85. B. Movaghar, L. O. Jones, M. A. Ratner, G. C. Schatz and K. L. Kohlstedt, *The Journal of Physical Chemistry C*, 2019, **123**, 29499-29512.
86. L. Berencei, W. Barford and S. R. Clark, *Phys. Rev. B*, 2022, **105**, 014303.
87. K. Asadi, A. J. Kronemeijer, T. Cramer, L. Jan Anton Koster, P. W. M. Blom and D. M. de Leeuw, *Nature Communications*, 2013, **4**, 1710.
88. N. Tessler, Y. Preezant, N. Rappaport and Y. Roichman, *Adv. Mater.*, 2009, **21**, 2741-2761.
89. A. Miller and E. Abrahams, *Phys. Rev.*, 1960, **120**, 745-755.
90. S. D. Baranovskii, *physica status solidi (b)*, 2014, **251**, 487-525.
91. S. D. Baranovskii, T. Faber, F. Hensel and P. Thomas, *J. Phys.: Condens. Matter*, 1997, **9**, 2699.
92. R. P. Fornari, P. W. M. Blom and A. Troisi, *Phys. Rev. Lett.*, 2017, **118**, 086601.
93. M. Nikolka, K. Broch, J. Armitage, D. Hanifi, P. J. Nowack, D. Venkateshvaran, A. Sadhanala, J. Saska, M. Mascal, S.-H. Jung, J. K. Lee, I. McCulloch, A. Salleo and H. Sirringhaus, *Nature Communications*, 2019, **10**, 2122.
94. X. Yan, M. Xiong, X.-Y. Deng, K.-K. Liu, J.-T. Li, X.-Q. Wang, S. Zhang, N. Prine, Z. Zhang, W. Huang, Y. Wang, J.-Y. Wang, X. Gu, S. K. So, J. Zhu and T. Lei, *Nature Communications*, 2021, **12**, 5723.
95. V. Lemaur, J. Cornil, R. Lazzaroni, H. Sirringhaus, D. Beljonne and Y. Olivier, *Chem. Mater.*, 2019, **31**, 6889-6899.
96. N. Vukmirović, *Physical Chemistry Chemical Physics*, 2013, **15**, 3543-3551.
97. T. Qin and A. Troisi, *Journal of the American Chemical Society*, 2013, **135**, 11247-11256.
98. D. S. Pearson, P. A. Pincus, G. W. Heffner and S. J. Dahman, *Macromolecules*, 1993, **26**, 1570-1575.
99. M. M. Henry, M. L. Jones, S. D. Oosterhout, W. A. Braunecker, T. W. Kemper, R. E. Larsen, N. Kopidakis, M. F. Toney, D. C. Olson and E. Jankowski, *The Journal of Physical Chemistry C*, 2017, **121**, 26528-26538.
100. D. P. McMahon and A. Troisi, *Chem. Phys. Lett.*, 2009, **480**, 210-214.
101. M. Gruber, S.-H. Jung, S. Schott, D. Venkateshvaran, A. J. Kronemeijer, J. W. Andreasen, C. R. McNeill, W. W. H. Wong, M. Shahid, M. Heeney, J.-K. Lee and H. Sirringhaus, *Chem. Sci.*, 2015, **6**, 6949-6960.
102. Z. Chen, M. J. Lee, R. Shahid Ashraf, Y. Gu, S. Albert-Seifried, M. Meedom Nielsen, B. Schroeder, T. D. Anthopoulos, M. Heeney, I. McCulloch and H. Sirringhaus, *Adv. Mater.*, 2012, **24**, 647-652.
103. H. Bronstein, Z. Chen, R. S. Ashraf, W. Zhang, J. Du, J. R. Durrant, P. Shakya Tuladhar, K. Song, S. E. Watkins, Y. Geerts, M. M. Wienk, R. A. J. Janssen, T. Anthopoulos, H. Sirringhaus, M. Heeney and I. McCulloch, *Journal of the American Chemical Society*, 2011, **133**, 3272-3275.
104. H. Geng, L. Zhu, Y. Yi, D. Zhu and Z. Shuai, *Chem. Mater.*, 2019, **31**, 6424-6434.
105. M. Xiao, A. Sadhanala, M. Abdi-Jalebi, T. H. Thomas, X. Ren, T. Zhang, H. Chen, R. L. Carey, Q. Wang, S. P. Senanayak, C. Jellett, A. Onwubiko, M. Moser, H. Liao, W. Yue, I. McCulloch, M. Nikolka and H. Sirringhaus, *Adv. Funct. Mater.*, 2021, **31**, 2007359.

106. S. Himmelberger, D. T. Duong, J. E. Northrup, J. Rivnay, F. P. V. Koch, B. S. Beckingham, N. Stingelin, R. A. Segalman, S. C. B. Mannsfeld and A. Salleo, *Adv. Funct. Mater.*, 2015, **25**, 2616-2624.
107. A. T. Hidayat, H. Benten, N. Ohta, Y. Na, A. Muraoka, H. Kojima, M.-C. Jung and M. Nakamura, *Macromolecules*, 2020, **53**, 6630-6639.
108. S. M. Ryno and C. Risko, *Physical Chemistry Chemical Physics*, 2019, **21**, 7802-7813.
109. R. Manurung and A. Troisi, *Journal of Materials Chemistry C*, 2022, **10**, 14319-14333.
110. J. Qu, Q. Zhao, J. Zhou, H. Lai, T. Liu, D. Li, W. Chen, Z. Xie and F. He, *Chem. Mater.*, 2019, **31**, 1664-1671.
111. R. Manurung, P. Li and A. Troisi, *The Journal of Physical Chemistry B*, 2021, **125**, 6338-6348.
112. T. W. Hagler, K. Pakbaz, K. F. Voss and A. J. Heeger, *Phys. Rev. B*, 1991, **44**, 8652-8666.
113. C. B. Nielsen, M. Turbiez and I. McCulloch, *Adv. Mater.*, 2013, **25**, 1859-1880.
114. M. D. Newton, *Chemical Reviews*, 1991, **91**, 767-792.
115. A. Nitzan, *Annual Review of Physical Chemistry*, 2001, **52**, 681-750.
116. H. M. McConnell, *The Journal of Chemical Physics*, 1961, **35**, 508-515.
117. S. Priyadarshy, S. S. Skourtis, S. M. Risser and D. N. Beratan, *The Journal of Chemical Physics*, 1996, **104**, 9473-9481.
118. A. J. Doig and M. J. E. Sternberg, *Protein Sci.*, 1995, **4**, 2247-2251.
119. O. Ostroverkhova, *Chem. Rev.*, 2016, **116**, 13279-13412.
120. W. Zhang, Y. Han, X. Zhu, Z. Fei, Y. Feng, N. D. Treat, H. Faber, N. Stingelin, I. McCulloch, T. D. Anthopoulos and M. Heeney, *Adv. Mater.*, 2016, **28**, 3922-3927.
121. H. Chen, M. Hurhangee, M. Nikolka, W. Zhang, M. Kirkus, M. Neophytou, S. J. Cryer, D. Harkin, P. Hayoz, M. Abdi-Jalebi, C. R. McNeill, H. Sirringhaus and I. McCulloch, *Advanced Materials*, 2017, **29**, 1702523.
122. S. Prodhan, J. Qiu, M. Ricci, O. M. Roscioni, L. Wang and D. Beljonne, *The Journal of Physical Chemistry Letters*, 2020, **11**, 6519-6525.
123. Q. Chen, Y. H. Han, L. R. Franco, C. F. N. Marchiori, Z. Genene, C. M. Araujo, J.-W. Lee, T. N.-L. Phan, J. Wu, D. Yu, D. J. Kim, T.-S. Kim, L. Hou, B. J. Kim and E. Wang, *Nano-Micro Letters*, 2022, **14**, 164.

Appendix

S1. Methods for obtaining the monomer block matrix

The methods devised and tested for obtaining the matrix elements for the coupling between LMOs on the same monomer, the "monomer block" matrix elements, and the results from their testing are outlined in Figure S1.1. The first method (a) in Figure S1.1 is to use a diagonal Fock matrix containing only the onsite energies of the MOs on the monomer included in the basis set and an identity matrix as the overlap matrix, both of which are obtained by transforming the atomic orbital basis matrix calculated for the isolated monomer into the MO basis using the transformations 3.1.3 and 3.1.4 in Chapter 3. This generates the least accurate results as the monomer is not isolated in the chain and the onsite energies would be perturbed by some amount by other surrounding bonded monomer units. The next two methods tried are with the matrix elements calculated for the monomer bonded at both of its connection sites to 2 other monomers in a trimer and the elements arising from MOs of the middle "embedded" monomer are the ones extracted; one method extracts the monomer block Fock and overlap matrix with only the on-diagonal elements (b) in Figure S1.1 and the other method extracts all the matrix elements involving LMOs on the middle embedded monomer (c) in Figure S1.1). Each method described was tested by calculating MO energies using LMOM which were compared to an exact calculation for a planar six-monomer polythiophene chain at B3LYP/3-21G* level of theory and plotting the LMOM and exact energies as shown in Figure S1.1, with a linear regression fitting and root mean square error (RMSE) calculated for each plot. The best result, as measured by the RMSE, is obtained using method c) using all the matrix elements involving LMOs on the middle embedded monomer and thus this method was used to obtain the monomer block matrix elements in the final implementation of LMOM outlined in Chapter 3 of the thesis.

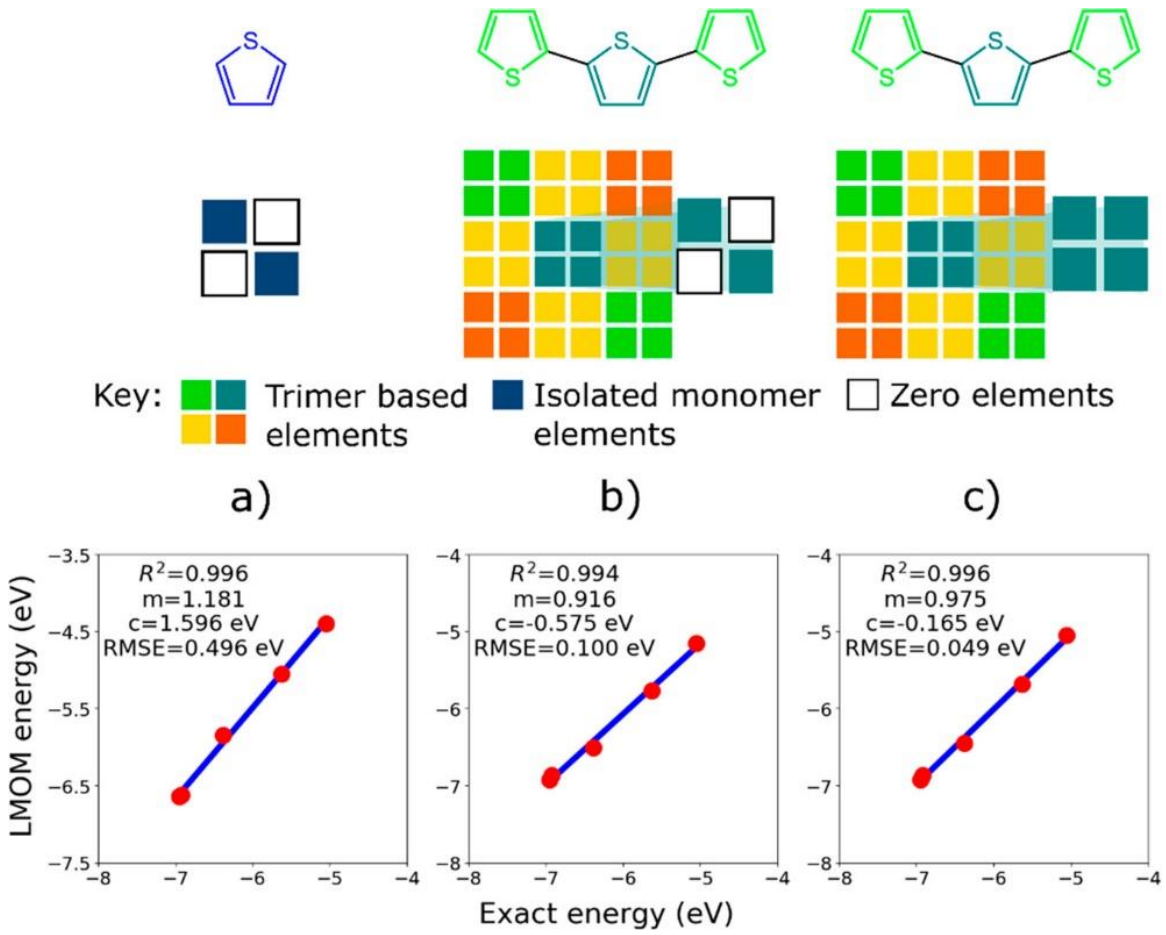

Figure S1.1: (top) Illustrations for the different methods of obtaining the monomer block matrix elements, with the following labels describing the source of the matrix elements: (a) isolated monomer, (b) only the on-diagonal elements involving LMOs on the (middle) embedded monomer, (c) all elements from the (middle) embedded monomer matrix segment. Individual monomers are distinguished by different colours (green, blue and cyan), and their matrix elements are illustrated as squares, with elements sharing a colour belonging to the same corresponding monomer. (bottom) Below the illustrations are plots with linear regression fitting for the top five valence band orbital energies of planar six-monomer polythiophene chain from the methods illustrated in a), b) and c), and the exact calculation.

S2. Results for testing linear and polynomial curve based calibration of LMOM calculated energies

Tables S1 and S2 show the results from the fitting of the exact calculation and calibrated LMOM calculation energies calculated using calibration parameters obtained with a range of calibration chain lengths and calibration sample sizes for two polymers, polythiophene and PDPP2TT, using the linear fitting (equations 3.3.1 and 3.3.3 in Chapter 4) and polynomial curve (equations 3.3.2. and 3.3.4 in Chapter 3) based methods described Chapter 3 of the thesis. The LMOM and exact calculation energies are obtained using B3LYP/3-21G* level of theory. The RMSE (equation 3.3.5. in Chapter 3) between the calibrated LMOM and exact energies was calculated for each calibration chain length and sample size tested, and the job CPU time in minutes calculated as the total sum job CPU time taken by the LMOM and exact calculation per chain is quoted.

There is very minor difference between the result obtained from using a linear and polynomial curve fitting across the two polymers, differing by around 10^{-3} eV across the RMSEs calculated, thus a linear fitting is preferred due to simpler implementation and calculation of the calibrated energies and thus the chosen method for the final implementation of LMOM described in Chapter 3 of the thesis. The computational time savings from altering the calibration sample size is only significant when going down to 5 chains, and for the chain length 3 repeat units (12-15 monomers) is the best compromise between accuracy and computational time. Thus, the preferred method for obtaining calibration parameters for each polymer is using a calibration sample size of 5 chains each with length equivalent to 3 repeat units.

Table S1: RMSE values with polynomial and line regression fits for polythiophene against time cost of generating the calibration sample (chain length=calibration chain length, number of chains=calibration sample size)

Chain length	6				12				24			
Number of chains	5	25	50	100	5	25	50	100	5	25	50	100
Job CPU time (minutes)	14.95	74.75	149.5	299.0	39.8	199.0	398.0	796.0	86.35	431.75	863.5	1727.0
RMSE polynomial (eV)	0.154	0.061	0.059	0.061	0.046	0.041	0.039	0.039	0.028	0.025	0.026	0.025
RMSE linear (eV)	0.065	0.070	0.065	0.068	0.044	0.042	0.039	0.041	0.027	0.027	0.029	0.027

Table S2: RMSE values with polynomial and line regression fits for PDPP2TT against time cost of generating the calibration sample (chain length=calibration chain length, number of chains=calibration sample size)

Chain length	6				12				24			
Number of chains	5	25	50	100	5	25	50	100	5	25	50	100
Job CPU time (minutes)	31.3	156.3	312.6	625.2	73.7	368.4	736.8	1473.5	239.2	1195.8	2391.5	4783.0
RMSE polynomial (eV)	0.108	0.110	0.110	0.111	0.055	0.058	0.057	0.057	0.020	0.023	0.025	0.024
RMSE linear (eV)	0.111	0.115	0.117	0.116	0.051	0.056	0.054	0.056	0.020	0.024	0.025	0.024

S3. Tail slope calculation

The tail slope in the density of states (DOS) is calculated using the method of finite differences for first derivatives and is defined as the inflection point on the DOS closest to the band gap. The inflection point is estimated as the energy at which the finite differences slope changes sign. The finite differences derivative for the DOS point $f(E_n)$ at the nth energy E_n in the sampled energy range is calculated as a forward difference, given in SE3.1.1.

$$\frac{df(E_n)}{dE} \approx \frac{f(E_n)-f(E_{n-1})}{E_n-E_{n-1}} \quad \text{(SE3.1.1)}$$

The energy at which this inflection point occurs is defined as the band edge energy $E_n = E_{EDGE}$.

S4. Comparison of polymer chain contour length and localisation length for examining finite size effects

In consideration of finite size effects associated with the use of defined chain lengths in the calculations of Chapter 4, the relative sizes of the contour length for the polymer chains and the localisation length at the band edge were examined. A structural repeating unit (SRU) length is defined in Figure 4.8 of Chapter 4 which can be used to estimate the contour length of the polymer chains, defined here as the SRU length multiplied by the total number of monomers divided by the number of monomers in the SRU. The result of the comparison is shown in Figure S4.1, where the contour length is usually at least 4 times the localisation length for each polymer.

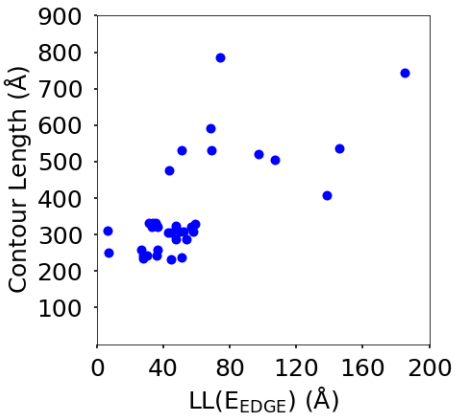

Figure S4.1: Plot comparing the contour length of the polymer chains and their localisation length at the band edge.

S5. Outlier polymers

This section of the Appendix will discuss the outliers and anomalies seen in the correlation plots of Chapter 4.

Section 4.4, Figure 5.6

The DOSs calculated for both polymers 4 (IDT-BT) and 22 (IIG-dSeV) are shown in Figure S5.1, which show outlier points in Figure 4.6, and that of polymer 36 (C5C6-BT) which is the "best" polymer for comparison. Both polymers 4 and 22 show a slightly broader tail in the DOS than the comparison example of polymer 36. Thus, the calculation of the tail slope, which is a finite differences first derivative, will be affected significantly by slight changes in the tail, even if the overall broadness is similar across the DOSs of the polymers that show higher localisation length.

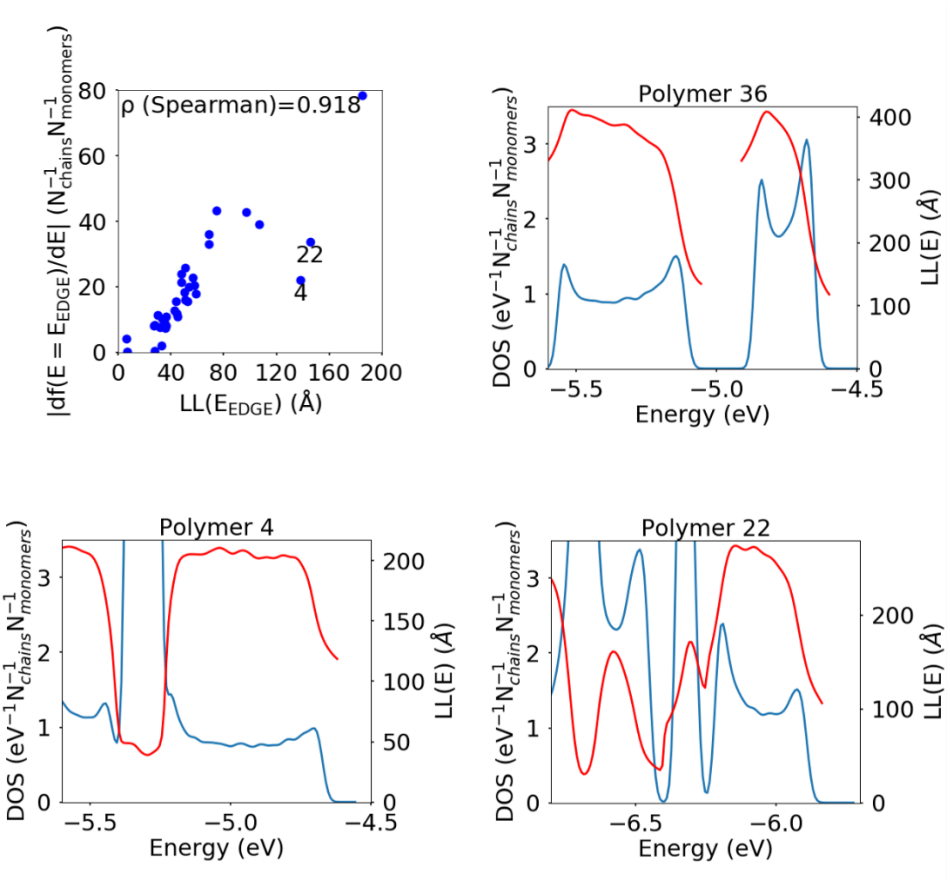

Figure S5.1: Comparison of DOSs for anomalous points polymers 4 and 22 (bottom) in Figure 4 (top left, polymers 4 and 22 highlighted) from Chapter 4 Figure 4.6 with that of polymer 36 (top right).

The density of states (DOS) and localisation length (LL(E)) plots below are those obtained for the polymers discussed in section 4.4 of Chapter 4 in the thesis which show notable shifts in the localisation length on reducing the basis set of the LMOM calculation. Each DOS is calculated with broadening σ=0.016 eV. For polymer 22 (DOS in Figure S5.3) in particular, the larger shift in its localisation length is attributed to having a higher density of Selenium compared to other polymers, with 2 Selenium atoms per SRU, thus making any basis set reductions have a bigger effect on the localisation length. The slightly smaller but significant shift in localisation length on reducing the basis set for polymer 18 (DOS in Figure S5.2) is attributed to the high lying states beyond 5 eV in the DOS that results from having the SeVT monomer which disappear when the basis set is reduced.

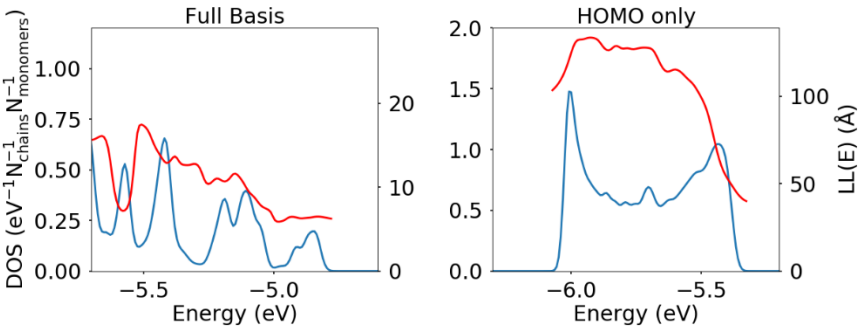

Figure S5.2: DOS and LL(E) plots for polymer 18 calculated using the full and reduced basis sets.

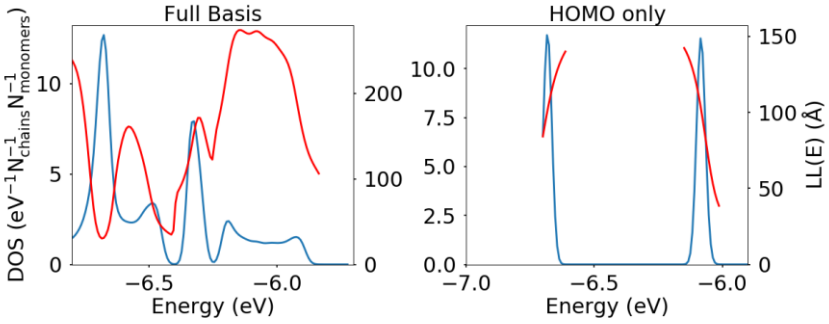

Figure S5.3: DOS and LL(E) plots for polymer 22 calculated using the full and reduced basis sets.

Using the HOMO per monomer only basis set is especially detrimental for polymer 7 (DOS in Figure 5.4) due to the mismatch between the HOMO energies and symmetry of the CDT and mdFP

monomers, shown in Figure S5.5, which results in weak coupling between these two MOs. The existence of the topmost band in the DOS thus depends on the coupling between the HOMO on CDT and HOMO-1 on mdFP, which ceases when the HOMO-1 per monomer is removed from the basis set.

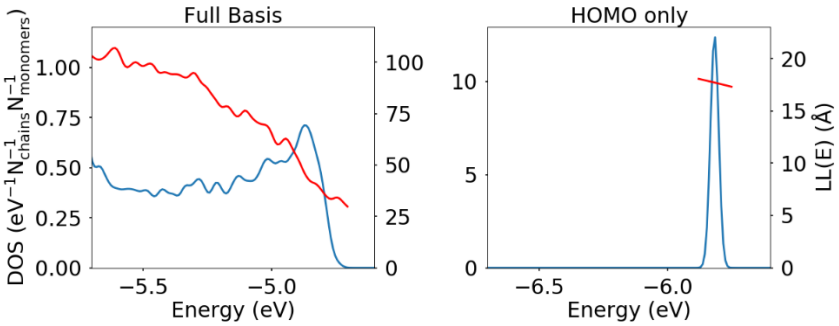

Figure S5.4: DOS and LL(E) plots for polymer 7 calculated using the full and reduced basis sets.

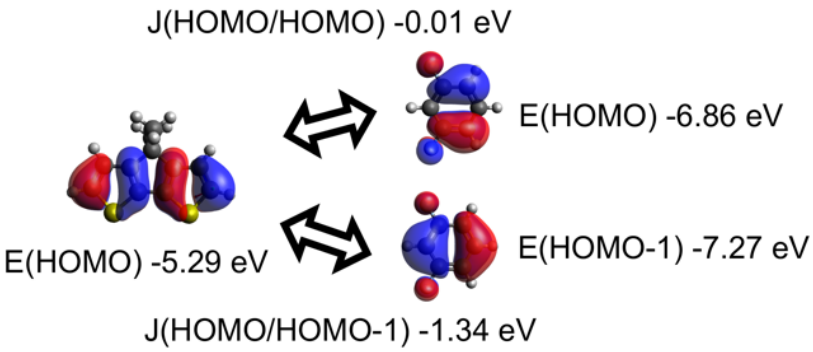

Figure S5.5: The CDT HOMO (left), mdFP HOMO (top right) and mdFP HOMO-1 (bottom right) juxtaposed, with isolated monomer HOMO energies and raw coupling values for each possible coupling pair with the shown MOs.

Polymer 32 (DOS in Figure S5.6) exhibits a unique shift in localisation length which increases when the basis set is HOMO and HOMO-1 per monomer but decreases further back reducing the basis set to HOMO only per monomer. The main cause of these shifts in localisation length is the HOMO of the oPy monomer, which has been calculated by DFT as a σ-symmetry MO, shown in Figure S5.6, whereas all other MOs included in the full basis set for this monomer are π-symmetry. This problem

is unique to polymer 32 and thus does not affect the interpretation of the results for the other polymers.

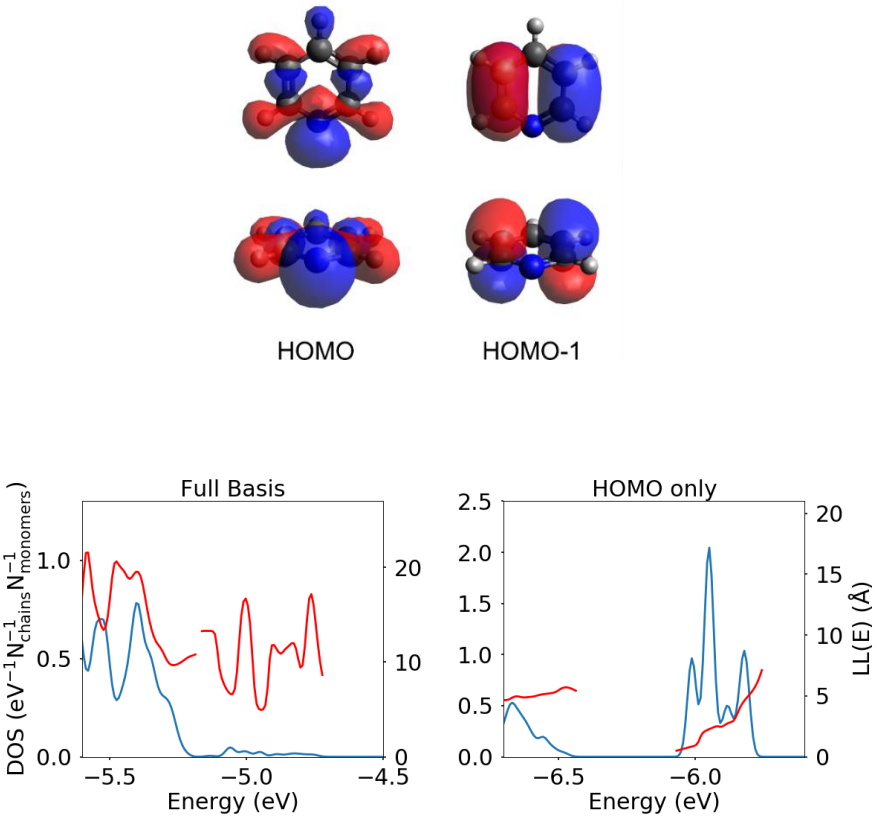

Figure S5.6: TOP: The HOMO and HOMO-1 of the oPy monomer. The HOMO is σ-symmetry as there is density along the plane of the monomer (bottom left), whereas the HOMO-1 is π-symmetry as there is no density along the plane of the monomer (bottom right). BOTTOM: DOS and LL(E) plots for polymer 32 calculated using the full and reduced basis sets.

Section 4.7, Figure 4.12

In Figure 4.12 of Chapter 4 section 4.7 in the thesis there is a single notable outlier point for the torsional entropy S_ϕ and relative coupling fluctuation $\sigma^{\mathrm{rel}}_{i,i+1}$ correlation plot corresponding to the DPP-oPy[A] dimer, highlighted in Figure S5.7. Figure S5.6 shows the oPy monomer has a sigma symmetry HOMO orbital calculated at B3LYP/3-21G* level of theory, which causes dimers with this monomer to display a non-cosine (sine-like) dependence of the HOMO-HOMO coupling on the dihedral angle, shown in Figure S5.7 for the DPP-oPy[A] dimer. While the torsional potential of the

DPP-oPy[A] dimer has deep minima around ϕ=0^{o}, the coupling profile in this region of the torsional potential has a varied slope leading to very high coupling fluctuation. Thus, the combination of features in the torsional potential and coupling profile results in a very strong outlier point.

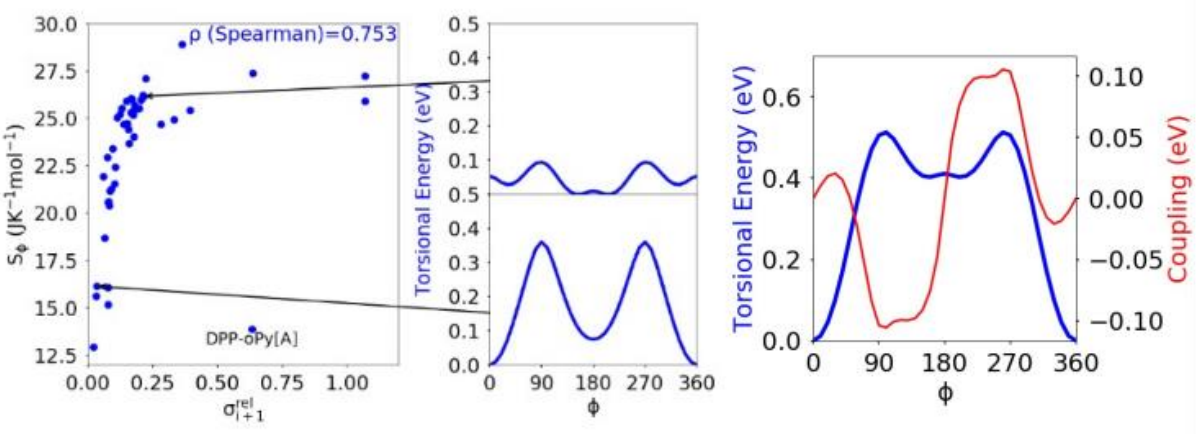

Figure S5.7: Highlight of outlier point in Figure 4.12 of Chapter 4 section 4.7 in the thesis (left), and the torsional potential and coupling profile for the DPP-oPy[A] dimer (right).

S6. Full plot for curvature vs relative coupling fluctuation

The full plot for relative coupling fluctuation $\sigma_{i,i+1}^{\mathrm{rel}}$ with each the curvature in the relative coupling profile measured at the global minima $d^2J_{i,i+1}^{rel}(\phi)/d\phi^2$ in the torsional potential for each dimer is shown in Figure S6.1. The points which deviate significantly from the cluster below $\sigma_{i,i+1}^{\mathrm{rel}}$<0.5 can be attributed to a non-cosine dependence of the coupling on the dihedral angle. The most significant deviations are from dimers with the oPy monomer, described previously in Appendix section S5 and Figure S5.7. Another example for one of these dimers, CDT-mdFP[A], is shown in Figure S6.2.

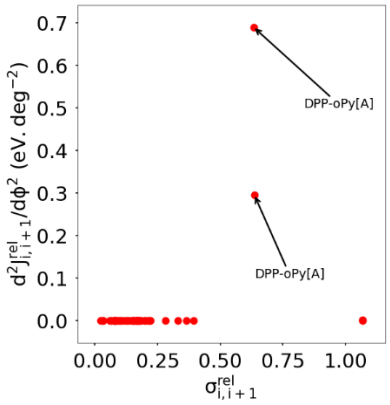

Figure S6.1: Full plot for $d^2J_{i,i+1}^{rel}(\phi)/d\phi^2$ vs $\sigma_{i,i+1}^{\mathrm{rel}}$ including all dimers.

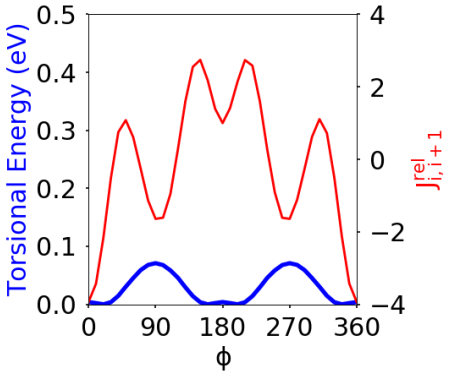

Figure S6.2: The relative torsion energy and relative coupling $J_{i,i+1}^{rel}$ plot for a dimer, CDT-mdFP[A] which displays non-cosine dependence of the coupling on the dihedral angle ϕ.

S7. Lowest and highest relative coupling dimers

In Figures S7.1 and S7.2 are shown the 10 lowest and highest relative coupling fluctuation dimers from those in the polymer sample shown in Figure 4.1 of Chapter 4 in the thesis. Dimers involving the oPy monomer, which is only relevant for polymer 2, were excluded from the sample when determining the 10 lowest and highest relative coupling fluctuation dimers due to the issue with oPy having a σ-symmetry HOMO, as described in section S5 Figure S5.6 of this Appendix.

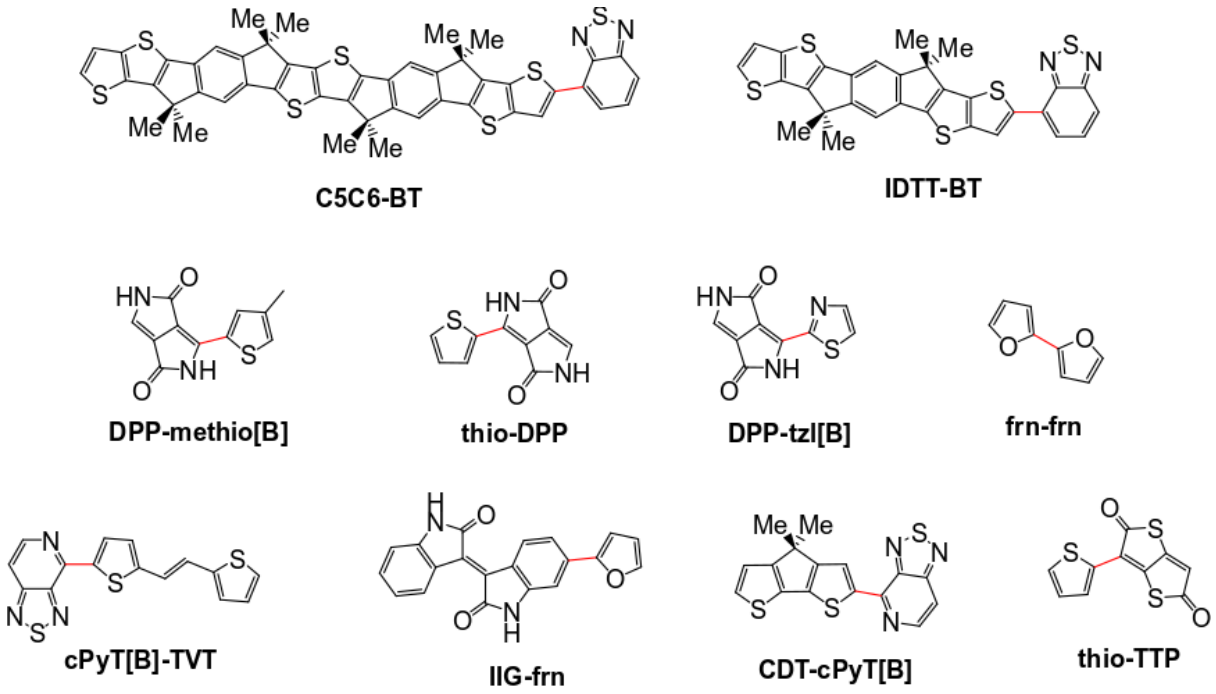

Figure S7.1: Dimers with lowest 10 relative coupling fluctuation

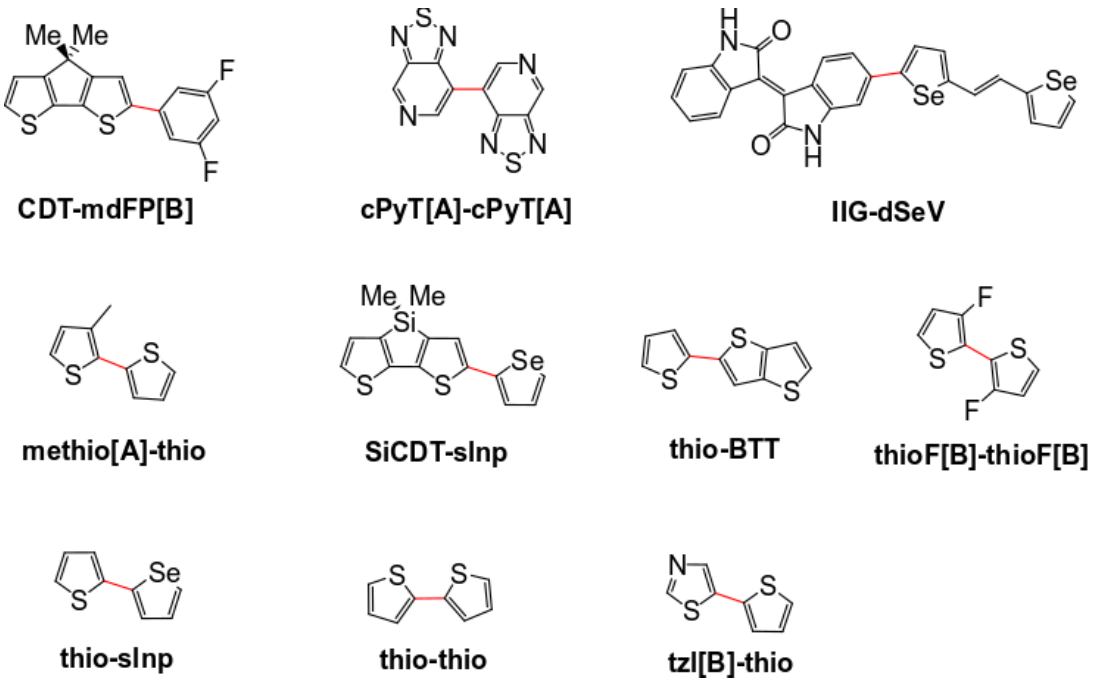

Figure S7.2: Dimers with highest 10 relative coupling fluctuation